Computation and Measurement of Force and Tissue Damage for the Grasper-tissue Interface in Robot-assisted Minimal Invasive Surgery

Lei Cheng

A dissertation submitted in partial fulfillment of the requirements for the degree of

Doctor of Philosophy

University of Washington

2015

Reading Committee:

Blake Hannaford, Chair

Eric Seibel

Martin Berg

Joshua Smith

Program Authorized to Offer Degree:

Mechanical Engineering

University of Washington

Abstract

Computation and Measurement of Force and Tissue Damage for the Grasper-tissue Interface in Robot-assisted Minimal Invasive Surgery

Lei Cheng

Chair of the Supervisory Committee:

Professor Blake Hannaford

Electrical Engineering

Robot-assisted minimally invasive surgery (RMIS) has many benefits for patients. However, loss of haptic feedback in the technique is a major limitation to surgeons since extensive applied force due to the lack of haptic feedback may cause unrecognized tissue damage. Also a surgical simulator without touch sensation is less adequate to train medical students to handle tissue safely. Various previous studies have reported the quantified tissue damage resulting from mechanical compression such as due to a surgical instrument grasping tissue; however, most of them require in-vitro bench work analysis, which limits their application in clinical conditions. This work provides a nonlinear finite element (FE) analysis of the grasper-tissue interaction to predict the reaction force on grasper jaws and degree of damage inside tissue. It also investigates the effects of the boundary conditions and material properties of the FE model on the simulated von Mises stress value and tissue damage. Four FE models were analyzed: two-dimensional (2D) plane strain model, 2D plane stress model, full three-dimensional (3D) model, and 3D thin membrane model. Our study shows that for integrated von Mises stress and tissue damage computations, the 3D thin membrane model yielded results closest to the full 3D analysis and

required only 0.2% of the compute time. Then the 3D thin membrane model was used further to extract the three descriptors (length, width and depth) of tissue deformation. Correlations between applied force from in vitro experiments and tissue models validate the ability to predict force from deformation. Finally, a wide range of grasper-tissue interfaces were evaluated regarding tissue damage magnitude and grasp quality. By comparing the results with previously published studies, we confirmed that the computational methodology is useful for researchers to develop and test various designs of graspers, reducing the need for time-consuming and expensive in vivo experiments. The results presented in this study can guide engineers to design surgical instruments to improve patient safety. Additionally it is useful for improving the surgical simulator performance by reflecting more realistic tissue material property and displaying tissue damage severity.

TABLE OF CONTENTS

LIST OF FIGURES

LIST OF TABLES

ACKNOWLEDGEMENTS

From the moment when I decided to follow the pioneers in robotics research, it was time to meet the participants with different backgrounds, who have helped me to accomplish my dissertation. Without their support and assistance, I may not make it. I would like to especially express the appreciation and acknowledgement to my advisor Prof. Blake Hannaford. You are such a great tutor that you never stop helping me in research, encouraging me and pointing out how I can improve my papers. Many thanks for your enthusiastic supervision, advice and support.

I also gratefully thank my doctorate committee members. Dr. Eric Seibel, thank you for your intensively reading and valuable comments on each paper I submitted. I really appreciate it. Dr. Martin Berg, thanks for your advices on how to clearly express the thesis' ideas. Dr. Joshua Smith, thank you for your encouragement and help since four years ago. Dr. Miqin Zhang, thanks for taking the time to help me complete my dissertation.

I am also greatly indebted to Dr. Smita De, for her guidance and support on the finite element model and Dr. Thomas Lendvay, for providing the opportunities to observe the laparoscopic ureteral reimplant surgery.

The members of the Bio-robotics lab made it a great and enjoyable place to work. Thank you all for helping me cheer ups. In particular, I would like thank Dr. Diana Friedman and Dr. Hawkeye King, for your guidance and support in building, testing and debugging the Raven Robots.

Finally, I would like to thank my friends for their help and encouragement. I would especially like to thank Irma Suntay and Lio Suntay for hosting me in their lovely home for three years.

The acknowledgement section goes here. The acknowledge section does not go into the table of contents.

DEDICATION

To my wife, Zhe.

For your unwavering love and support.

Chapter 1. Introduction

The population in the United States undergoing minimally invasive surgery (MIS), also known as laparoscopic surgery, has grown steadily since the late 1980s. In the United States, each year more than 2 million patients undergo MIS [1]. The advantages of these surgeries over open surgery have been highlighted by a large series of reports, including reduced recovery time, shorter hospital stays and less pain for patients [2]. There are two widely used MIS techniques: manual MIS (MMIS) and robotic-assisted MIS (RMIS). Due to the robotic use, RMIS can allow remote or even unmanned surgery as well as providing more precision and less trauma to patients. There is strong interest in the medical community moving towards RMIS. It is reported that over 2,500 surgery robots have been installed in hospitals all over the world, while sustaining growth in excess of 25% annually [3,4].

1.1 Motivations

Lack of Force Feedback in RMIS

The development of RMIS has resulted in growing interest in research to improve surgeon training and proficiency as well as patient safety [5]. Current design of RMIS eliminates all natural haptic feedback since the surgeons no longer manipulate either the tissue or the instrument directly [6]. This limitation is a significant handicap in performing the technically more dedicate surgical tasks such as suturing a coronary arterial anastomosis with fine polypropylene suture, in which the application of excessive forces may break sutures or tear tissue. The consequences of such surgical errors can cause an increase in operation time, irreversible injury or even patient's death [7].

In robotics research, haptic feedback refers to transmission of physical signals (force, pressure, temperature, etc.) through real or simulated interaction between robots, humans and environments [6]. The goal of haptic studies in RMIS is to provide a feeling for surgeons that they are contacting patients directly. Such devices usually include haptic sensors which can acquire haptic signals on the patient side and display devices which can transfer signals to

surgeons. Both parts working together can help surgeons be able to distinguish tissues types. Also they can guide surgeons to apply a "suitable" force to manipulate tissue: strong enough to avoid slippage but not too high to damage the tissue.

Challenge in Designing Haptic Devices for RMIS

It is a big challenge to design haptic devices for RMIS because it is required to provide wide-range haptic information to surgeons without losing the minimal invasivity and high dexterity [6]. Commercially available force sensors have been used to measure contact forces accurately. Several attempts have successfully been made by attaching specialized force sensors to the jaws of an existing grasper [9] or redesigning the instruments [10]. However, severe environmental constraints in RMIS, like size, biocompatibility, and sterilizability, prevent wide use of such sensors. Besides, it is costly to install additional sensors to current RMIS instruments which are frequently replaced.

Limited Employment of FEA in RMIS

One potential methodology for analyzing grasper-tissue interaction is Finite Element Analysis (FEA), which has served as an industry standard for prototype and design. FEA experiments can be carried out without ethical approval or financial issue; while testing a large amount of grasper designs in-vivo would be more complicated and expensive. A number of studies have presented the FEA simulation results of contact mechanics between robotic finger and objects [23-24]. Using non-linear finite element simulations, Xydas et al. found the normal force over fingertip radius relationship matched well with experimental results for a board range of normal force [23]. Tian et al. found an accurate match in deformation of a grasped object between 3-D scanner and FEA nonlinear elasticity model respectively [24]. Although these studies are not specific to grasping soft tissue in MIS, their results of correlation between simulations and experimental data do suggest that FEA could be an effective tool for understanding stress and strain distributions in tissue under loads.

Increasing Interests in Assessment of Tissue Damage and Grasping Quality

While the majority of research interests on RMIS have focused on haptic feedback during grasping [11-15], until recently little attention has been given to the tissue damage or grasp

stability properties of RMIS grasper instruments. Most of such experiments investigating tissue-grasper interaction were performed in vitro, which limits the applicability of the results to clinical conditions. Also these studies assessed tissue injury and grasp security simply by visual inspection, such as whether a visible tissue tear and gross slip occurred [16-18]. Some studies, however, suggested 1) subtle tissue abnormalities may exist and be nearly invisible to naked-eye examination [19-20]; 2) Slip, especially incipient slip, will not occur evenly over the surface [21, 22]; both of which indicate the need for evaluating tissue damage and grasp stability on a finer scale.

1.2 Medical Significance

The evaluation of force and tissue damage under external loads in RMIS may guide engineers to create or modify surgical instruments to improve patient safety as well as surgeon training [5]. Instruments which can automatically display the force and tissue damage may decrease surgical complications [Figure 1.1]. Also, improved design of the grasper may reduce tissue damage or/and provide more grasp stability. The surgical simulator performance could be improved by incorporating more realistic tissue material properties and predicting tissue damage for the student.

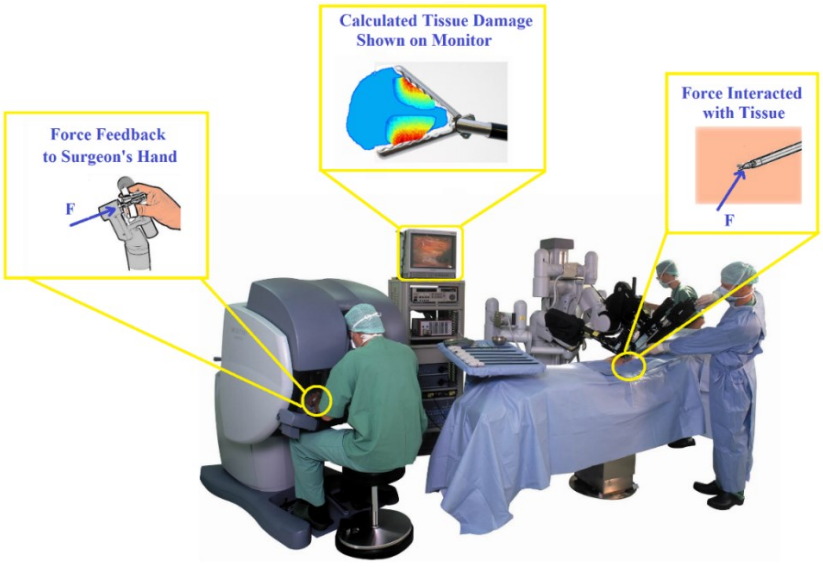

Figure 1.1 Demonstration of how our study can be applied in RMIS. During the operation of RMIS, surgeons can feel the applied force as well as observing how severe the tissue damage could be due to the grasping force.

1.3 Objectives

This study aims to investigate the grasper-tissue interface both in computational simulation and experiments. The three primary goals of this study are: 1) investigate the effects of the boundary conditions and material properties of the FE liver tissue model on the damage prediction for compression in RMIS; 2) explore the quantitative relationship between deformation and force. Through such a function, the forces applied to the soft tissue would be predicted without using force sensors; and 3) build up a numerical method for testing graspers with various jaw patterns for reducing tissue damage and preventing slippage.

1.4 Arrangement of Dissertation

Thus far we have explained the motivations and medical benefits of computing and measurement of force and tissue damage in RMIS. Chapter 2, 3 and 4 present modified manuscripts that have either been published (Chapter 2&4) or are ready to be submitted. Chapter 2 describes the theoretical foundation and numerical issues of the nonlinear FEA simulation for liver. Chapter 3 experimentally explores the quantitative relationship between deformation and force using customized grasper jaw with force sensing. Chapter 4 contains a comparison of grasping quality for various grasper jaw patterns. Chapter 5 summarize the contributions and contribution of this dissertation.

1.5 References for Chapter 1

[1] Market engineering research for the U.S. market for general surgery laparoscopy access and closure instruments. Medical and Healthcare Marketplace Guide, 1999. Publisher: Frost & Sullivan London 071 730 3438. Dialog File Number 767 Accession Number 523034. [Cited 2001 Oct 18]. Available from: URL: http://www.dialogselect.com/business/cgi/present

[2] NJ Soper, LM Brunt, K Kerbl. Laparoscopic general surgery. New England Journal of Medicine. 10;330(6):409–419;1994.

[3] http://www.cnn.com/2013/08/02/tech/da-vinci-robot-surgery/index.html

[4] http://www.intuitivesurgical.com/company/

[5] S De. The Grasper-Tissue Interface in Minimally Invasive Surgery: Stress and Acute Indicators of Injury. Ph.D. Thesis, University of Washington, 2008.

[6] AM Okamura. Haptic feedback in robot-assisted minimally invasive surgery. Current Opinion in Urology. 19:102-107; 2009.

[7] BT Bethea, et al. Application of haptic feedback to robotic surgery. Journal of Laparoendoscopic and Advanced Surgical Techniques Part A. 14 (3):191-195, 2004.

[8] A.M. Okamura. Methods for haptic feedback in teleoperated robot-assisted surgery. Industrial Robot: An International Journal, 31(6):499-508, 2004.

[9] J Dargahi, et al. Modeling and testing of an endoscopic piezoelectric-based tactile sensor. Mechatronics. 17: 462-467, 2007.

[10] B Kubler, et al. Development of actuated and sensor integrated forceps for minimally invasive robotic surgery. The International Journal of Medical Robotics and Computer Assisted Surgery, 1(3):96-107, 2005.

[11] T Hu, G Tholey, JP Desai, AE Castellanos. Evaluation of a Laparoscopic Grasper with Force Feedback. Surgical Endoscopy, 18(5): 863-867, 2004.

[12] M MacFarlane, J Rosen, B Hannaford, C Pellegrini, M Sinanan. Force feedback grasper helps restore the sense of touch in minimally invasive surgery. Journal of Gastrointestinal Surgery, 3(3):278–285, 1999.

[13] J Rosen, B Hannaford, M MacFarlane, M Sinanan. Force Controlled and Teleoperated Endoscopic Grasper for Minimally Invasive Surgery - Experimental Performance Evaluation. IEEE Transactions on Biomedical Engineering, 46:1212-1221, Oct, 1999.

[14] G. Tholey, JP Desai, AE Castellanos. Force feedback plays asignificant role in minimally invasive surgery: results and analysis. Annals of Surgery. 241(1):102–109, 2005.

[15] K Vakili, MS Flander, TR Sepp, MCorral, JD Diaz, A Slocum, GSL Teo. Design and Testing of a Pressure Sensing Laparoscopic Grasper. Proceedings of the 2011 Design of Medical Devices Conference DMD2011. April 12-14, 2011, Minneapolis, MN, USA

[16] AJ Shakeshaft, JA Cartmill, WR Walsh, CJ Martin. A curved edge moderates high pressure generated by a laparoscopic grasper. Surgical Endoscopy. 15:1232–1234, 2001.

[17] DD Marucci, J A Cartmill, WR Walsh, C. J. Martin. Patterns of failure at the instrument tissue interface. Journal of Surgical Research. 93(1):16-20, 2000.

[18] EA Heijnsdijk, VH de, J Dankelman, DJ Gouma. Slip and damage properties of jaws of laparoscopic graspers. Surgical Endoscopy, 18: 974-979, 2004.

[19] JC Kalff, WH Schraut, RL Simmons, AJ Bauer. Surgical manipulation of the gut elicits an intestinal muscularis inflammatory response resulting in postsurgical ileus. Annals of Surgery, 228(5):652-663, 1998.

[20] R Anup, KA Balasubramanian. Surgical stress and the gastrointestinal tract. Journal of Surgical Research. 92(2):291-300, 2000.

[21] J Stoll, P Dupont. Force Control for Grasping Soft Tissue. Proceedings of the 2006 IEEE International Conference on Robotics and Automation, May 2006, Orlando, FL, USA.

[22] VA Ho, S Hirai. Understanding Slip Perception of Soft Fingertips by Modeling and Simulating Stick-Slip Phenomenon. Robotics: Science and Systems, 2011.

[23] N Xydas, M Bhagavat, I Kao. Study of soft-finger contact mechanics using finite elements analysis and experiments. Proceedings of IEEE International Conference on Robotics and Automation, 2179–2184, 2000.

[24] J Tian, YB Jia. Modeling deformable shell-like objects grasped by a robot hand. Proceedings of the IEEE International Conference on Robotics and Automation, 1297-1302, 2009.

Chapter 2. Finite Element Analysis for Evaluating Liver Tissue Damage Due to Mechanical Compression

2.1 Overview

The development of robotic-assisted minimally invasive surgery (RMIS) has resulted in increased research to improve surgeon training, proficiency and patient safety. Minimizing tissue damage is an essential consideration in RMIS. Various studies have reported the quantified tissue damage resulting from mechanical compression; however, most of them require bench work analysis, which limits their application in clinical conditions of RMIS. We present a new methodology based on nonlinear finite element (FE) analysis that can predict damage degree inside tissue. The effects of the boundary conditions and material property of the FE model on the simulated von Mises stress value and tissue damage were investigated. Four FE models were analyzed: two-dimensional 2D plane strain model, 2D plane stress model, full three-dimensional 3D model, and 3D thin membrane model. Nonlinear material properties of liver tissue used in the FEA were derived from previously reported in vivo and in vitro experiments.

Our study showed that for integrated von Mises stress and tissue damage computations, the 3D thin membrane model yielded results closest to the full 3D analysis and required only 0.2% of the compute time. The results from 3D thin membrane and the full 3D models fell below plane-strain model and above the plane-stress model. Both stress and necrosis distributions were impacted by the material property of FE models. This study can guide engineers to design surgical instruments to improve patient safety. Additionally it is useful for improving the surgical simulator performance by reflecting more realistic tissue material property and displaying tissue damage severity.

2.2 Introduction

Extensive research on robotic-assisted minimally invasive surgery (RMIS) has focused on haptic feedback during grasping [1-5], however, little attention has been given to tissue damage resulting from grasping. A number of previous studies have quantified tissue damage specifically

** This is a modified version of the published manuscript: Lei et al. Finite Element Analysis for Evaluating Liver Tissue Damage Due to Mechanical Compression. Journal of Biomechanics, Vol. 48, Issue 6, 948-955. 2015.

from general mechanical compression. Famaey et al. [6, 7] quantitatively studied the damage to smooth muscle cells of rat abdominal arteries after in vivo clamping to well-defined loading levels by using an isometric contraction model. De et al. [8, 9] proposed a damage-stress relationship based on measuring hepatic necrosis as a function of stress from in vivo experiments. Our study adopted De et al.'s quantitative study of necrosis for two reasons. First, we have extensive experimental data from De et al.'s and Rosen et al.'s earlier works. Second, the liver is widely modeled as isotropic and homogeneous which simplifies parameter identification and FEM [9, 16].

The results from these quantitative studies can be used by finite element analysis (FEA) to predict tissue damage in a RMIS simulator. However, a tissue model needs to be established and validated for such surgery simulation [10]. It is well known that most soft tissue is nonlinear, inhomogeneous and viscoeleastic [11]. However, liver is considered to be a good model for continuum mechanics study because it is approximately isotropic and homogenous in uniform histology cross sections [12, 13]. If the strain rate effect is excluded, that is to say, the strain only changes with location but not with time, the mechanical response of liver tissue can be described by elastic model [14].

Uniaxial tension and compression are commonly used methods to investigate isotropic and homogeneous material. There are numerous published studies covering uniaxial tests on various soft tissues [10, 13, 15], however, most of them were performed in vitro. The research presented in Rosen et al. [16]. is the only published study in vivo compression testes using a motorized endoscope grasper.

Our study investigates whether there is significant difference in simulating tissue damage between various in vivo and in vitro experiments. Additionally, we compare and contrast the effectiveness of the two-dimensional 2D and three-dimensional 3D FEA simulation in investigating the mechanical response of soft tissue to external loads. 2D models are preferred in industry because they are quicker and simplify the analysis during the initial design phase [17, 22]. However, there could be some physical characteristics that exist in 3D models that cannot be

simulated in a 2D model. At this time, few reports have evaluated how these geometrical assumptions affect the reaction force and tissue damage computations in RMIS simulation.

The objective of the current study is to investigate the effects of the boundary conditions and material properties of the FE liver tissue model on the damage prediction for compression in RMIS. This type of investigation requires a balance between real world and computational efficiency. In this study, we extended earlier 2D, non-linear finite element analyses to 3D, dramatically increasing the size of the computation. The liver tissue was considered nonlinear to maximize accuracy and homogenous and elastic to increase computational efficiency. Nonlinear finite element analyses were performed using ANSYS Mechanical APDL 14.0 under various geometrical assumptions: 2D plane strain, 2D plane stress, full 3D, and 3D thin membrane. The resulting stress distribution and the integrated stress value were compared among the four models. The spatial distribution of tissue damage was calculated from the stress distributions based on De et al.'s necrosis-stress function [9]. Additionally, three nonlinear material properties were studied in the full 3D model. Finally, the computed stress distribution, integrated stress value, and the tissue damage in the form of hepatic necrosis were compared.

2.3 Methods

2.3.1 *The Material model for tissue and grasper*

The modeling methods for this research are similar to a recent study [21] in which 2D simulations were used. Soft tissue is often inhomogeneous and anisotropic and its compounds vary throughout the whole structure. Carter et al. [12] found solid organs, particularly the liver and spleen, could be treated as approximately isotropic and homogenous. Because of the high water content of the liver tissue, we can consider it to be incompressible [14]

We adopted the nonlinear biomechanical property of the liver from Rosen et al.'s experiments [16]. In that work, porcine liver was tested both in vivo and in vitro under uniaxial compressive loadings using a custom-made device called the Motorized Endoscopic Grasper (MEG) and in vitro using a servohydraulic material testing system by MTS Corporation (Eden Prairie, MN).

Compression stress (σ) and strain (ε) experimental data were plotted with the associated elastic phenomenological curve fitting function [16]:

$$\sigma = \beta(e^{\alpha\varepsilon^2} - 1) + \gamma\varepsilon \qquad \text{(Eq2.1)}$$

Another common approach for studying the mechanical behavior of soft tissue is to use the constitutive physical-law based model [10, 16]. This study employs the Ogden model, which is a well-established hyperelastic material model to describe the nonlinear stress-strain material behavior [18]. In the Ogden model, the material behavior is described by means of the strain energy density function:

$$W_O = \sum_{i=1}^{N} \frac{\mu_i}{\alpha_i}[\lambda_1^{\alpha_i} + \lambda_2^{\alpha_i} + \lambda_3^{\alpha_i} - 3 + \frac{1}{d_i}(J-1)^{2i}] \qquad \text{(Eq2.2)}$$

where N is the model's order, α_i and μ_i are the parameters to be determined experimentally, and d_i represents the change in volume. λ_k(k=1, 2, 3) and J refer to the principal stretch and the Jacobian of the deformation gradient respectively. Assuming that the liver is incompressible, the Jacobian of the deformation gradient becomes 1 ($J = \lambda_1\lambda_2\lambda_3 = 1$). Eq2.2 can then be simplified as below:

$$W_O = \sum_{i=1}^{N} \frac{\mu_i}{\alpha_i}[\lambda_1^{\alpha_i} + \lambda_2^{\alpha_i} + \lambda_3^{\alpha_i} - 3] \qquad \text{(Eq2.3)}$$

Classical continuum mechanics provides us with the principal stress, $\sigma_i = \lambda_i \frac{\partial W_O}{\partial \lambda_i}$, where λ_1 represents the stretch ratio in the direction of compression and σ_1 represents the corresponding principal stress. Since approximately an unconfined compression test was performed in Rosen et al.'s study [16], the other two principal stresses are approximated as zero ($\sigma_2 = \sigma_3 = 0$). Thus we will have $\lambda_2 = \lambda_3 = \lambda_1^{-1/2}$. Plugging λ_2 and λ_3 into Eq 2.3 yields:

$$\sigma_c = \sum_{i=1}^{N} \mu_i[\lambda_1^{\alpha_i} - \lambda_1^{-\alpha_i/2}] \qquad \text{(Eq2.4)}$$

Adopting the notation of Rosen et al. [24], with the compression load, $\sigma_c = -\sigma$, and $\lambda = 1 - \varepsilon$, we can then numerically fit Rosen et al.'s phenomenological stress-strain curves to Eq 2.4 by the following steps: 1) The phenomenological model parameters β, α and γ in Rosen et al.'s study [24] were the statistical mean values derived from several measurements. For each measurement, the liver tissue failed at different maximum strain, ranged from 0.35 to 0.6. Thus we choose strain ranging from 0 to 0.35 as the data-fitting region. 2) The corresponding stress is calculated by Eq 2.1 by the increments of 0.01. 3) The strain and stress from step 2 are imported into MATLAB Curve Fitting Tool (Mathworks Inc.). Using the trust-region algorithm and least absolute residuals (LAR) method, we can obtain the parameters of the 1st-order Ogden model (Eq 2.4, N=1) with the coefficient of determination R^2<0.98 (see Table 2.1).

Table 2.1 The parameters for the least-square fitting 1st-order Ogden model with the phenomenological model under various experiment conditions.

Experiment Condition	Phenomenological Model [16]	1st-order Ogden Model
MEG, in vivo	β=7377, α=21 , γ=3289	α_1=16.02 , μ_1=0.002934
MEG, in vitro	β=7972, α=20, γ=781	α_1=15.44 , μ_1=0.003163
MTS, in vitro	β=8450, α=26 , γ=1679	α_1=20.82 , μ_1=0.002227

The plot in Figure 2.1 compares the stress-stretch curves of the Ogden fit model with the original phenomenological curves in Rosen et al.'s study. In the region where 1>stretch>0.8, Figure 2.1 shows that the MEG in vivo curves are close to MEG in vitro curves but far from MTS in vitro curves.

Surgical graspers are considered to be composed of an isotropic linear elastic material (stainless steel) with the Young's modulus E=190GPa and the Poisson's ratio ν=0.27 [8].

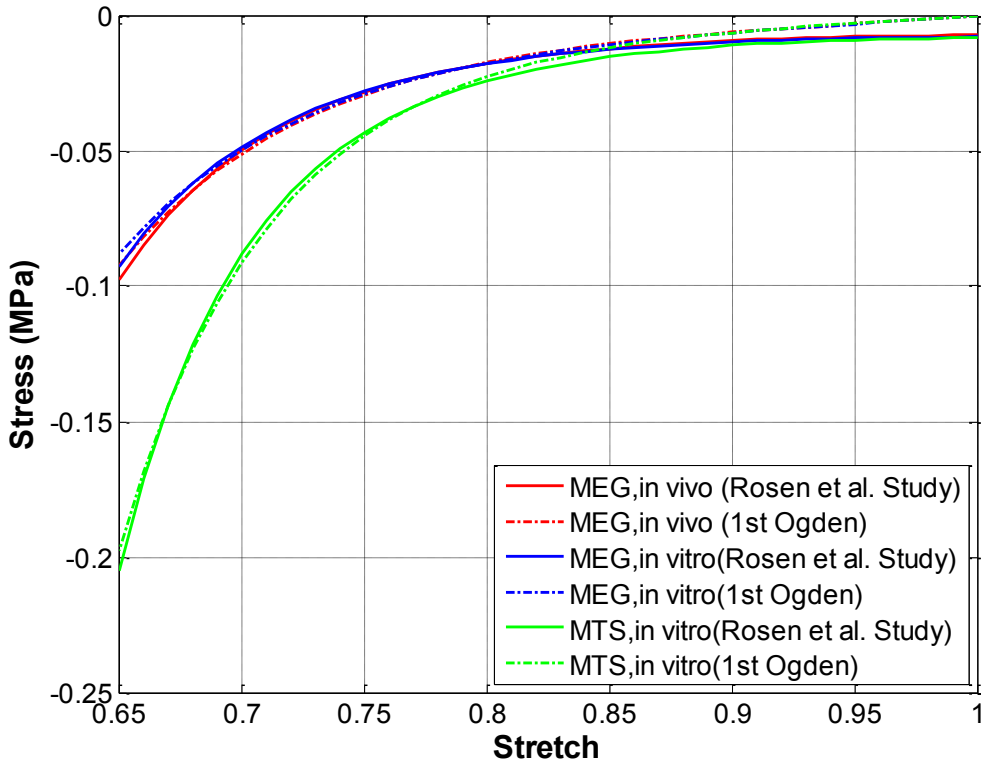

Figure 2.1 Stretch-stress curves for various nonlinear tissue models.

2.3.2 *Two-Dimensional Finite element models*

Two assumptions are made for the 2D models: the plane strain model, which assumes the out of plane-strains are zero and the plane stress model, which assumes the out of plane-stresses are zero.

The outline of 2D models of the tissue-grasper contact shows the geometry and applied displacement vector (Figure 2.2A). The dimension of the liver tissue slice is set to 10mm height by 20mm width. The grasper is set to be 2mm height by 5mm width. Because of the symmetry during grasping, only half of the tissue (5mm height×20mm width) is considered in the analysis. The nodes on the bottom line (y=-5mm) can only have freedom along the x direction. The applied displacement of the grasper increases from 0 mm to 2mm by the increments of 0.01mm in the negative y direction (Uy=0~-2mm).

The tissue is modeled with 4-noded axisymmetric, quadrilateral, solid elements. The meshing size for the tissue is uniform to facilitate the comparison with three-dimensional models. The grasper domain is meshed using the same element type but its size is gradually refined for the portions which will potentially be involved in the grasper-tissue interaction (Figure 2.2B).

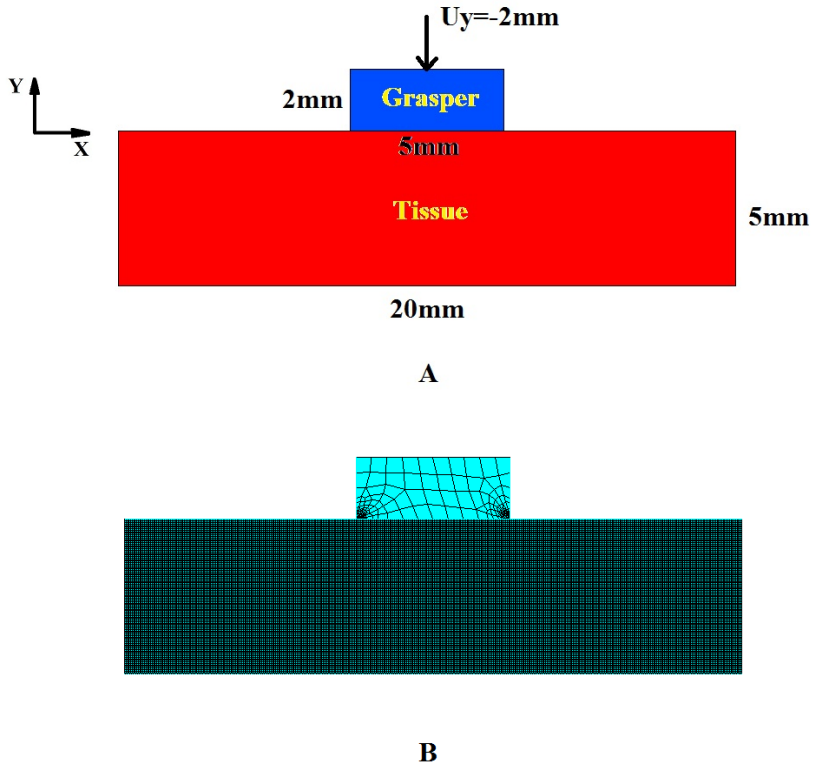

Figure 2.2 2D Finite element model of tissue and grasper. A) Illustration of geometry and applied displacement; B) meshing size of tissue=0.05mm.

2.3.3 *Three-Dimensional Finite element models*

The three-dimensional 3D model of the tissue and grasper with geometry and displacement is shown in Figure 3A. Two 3D models are analyzed in the study: the 3D thin membrane model and the full 3D model. The dimensions of the thin membrane model (Figure 2.3B) are: 10mm high, 20mm wide, and 0.2mm thick. The size of grasper is set at 2mm high, 5mm wide and 3mm thick. For the full 3D model, dimensions of the tissue and grasper blocks are 10mm high, 20mm wide, 20mm thick and 2mm high, 5mm wide, 3mm thick respectively (Figure 2.3C). Similarly to the 2D models, because of the symmetry during grasping, only half of the tissue is considered in

our analysis. The nodes on the bottom surface (y=-5mm) can only have freedom along the x and z direction. The applied displacement of the grasper increases from 0 mm to 2mm by the increments of 0.01 mm in the negative y direction (Uy=0~-2mm). In the 3D model the meshing size for the grasper is set to be uniform at 0.5 mm. Table 2 lists the meshing sizes and element types of tissue for each model.

Table 2.2 Meshing size and element type of 3D finite element tissue models.

<table>
<tr><td></td><td>Meshing type</td><td>Solid element type</td><td colspan="2">Meshing size</td></tr>
<tr><td rowspan="2">3D thin membrane</td><td rowspan="2">Uniform meshing</td><td rowspan="2">8-noded hexahedral</td><td colspan="2">0.2 mm</td></tr>
<tr><td colspan="2">0.05 mm</td></tr>
<tr><td rowspan="6">Full 3D</td><td>Uniform meshing</td><td>8-noded hexahedral</td><td colspan="2">0.2 mm</td></tr>
<tr><td rowspan="5">Refined meshing</td><td rowspan="5">10-node Tetrahedral</td><td colspan="2">Variable meshing size</td></tr>
<tr><td>Refined meshing region</td><td>Meshing size</td></tr>
<tr><td>|x|>8mm,|z|>4mm, -5<y<-4mm</td><td>≈1.5 mm</td></tr>
<tr><td>8mm>|x|>4mm ,2.4<|z|<4mm, -4<y<-2mm</td><td>≈0.75mm</td></tr>
<tr><td>4mm>|x|>3mm, 1.2<|z|<2.4mm, -2<y<-1mm</td><td>≈0.0375 mm</td></tr>
</table>

			$\|x\|<3mm$, $\|z\|<1.2mm$, $-1<y<0mm$	≈0.01875 mm

To compare the results of 3D with the 2D models, the center cut plane along the z direction is extracted from the 3D simulation results. Figure 2.3E illustrates the location of the center cut plane in the 3D model. The cutting plane commands in ANSYS APDL were employed to map and linearize the stresses onto the cut plane.

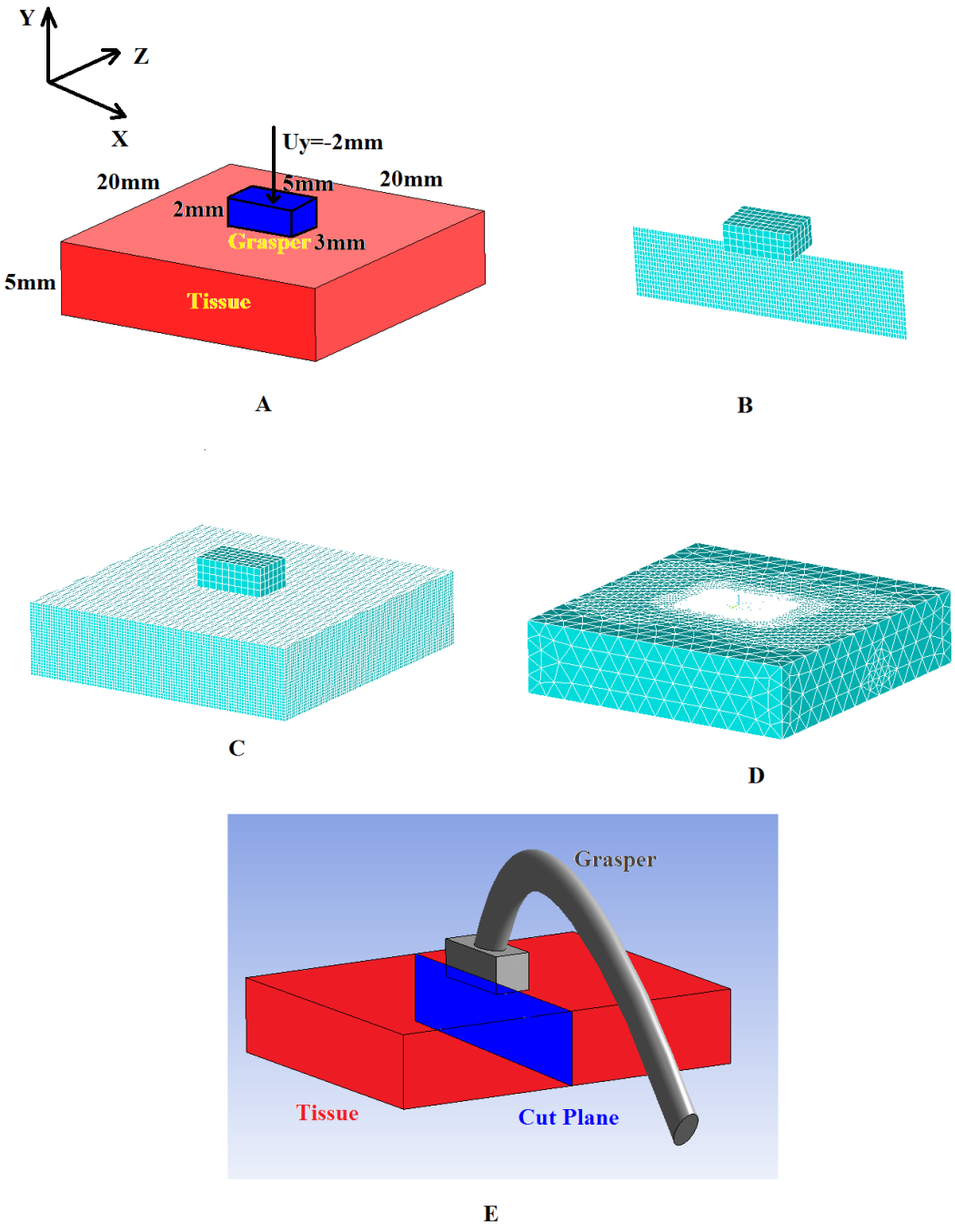

Figure 2.3 3D Finite element model of tissue and grasper. A) geometry and applied displacement in full 3D model; B) 3D thin membrane model; C) full 3D model; D) refined meshing of tissue for full 3D model. E) Center cut plane (blue area) in full 3D model. Red areas sketch tissue while grey solid areas sketch grasper.

For both 2D and 3D models, we use the Augmented Lagrangian Method to analyze the contact between tissue and grasper. The friction coefficient is assumed to 1.0. Appropriate values of normal penalty stiffness (FKN) and penetration tolerance (FTOLN) are assigned to help the solver converge and avoid penetration. Detailed information about algorithms for frictional contact can be found in the ANSYS Theory Document Release [23].

2.3.4 *Calculation of tissue damage*

We utilized the stress magnitude value from De et al. (2008)'s study. Three hours after animals were euthanized, the test tissues were harvested and processed for staining. Multiple sections were taken from each compressed tissue sample parallel to the direction of compression. Cell death, as represented by percent area of necrosis, was quantified by image analysis software. Through a nonlinear mixed effect model, the hepatic necrosis as a function of stress was obtained as below [9]:

$$\%Necrosis = a + \frac{B * {\sigma_v}^C}{D^C + {\sigma_v}^C} + Duration * E \qquad \text{(Eq2.5)}$$

σ_v and Duration refer to equilibrium von Mises stress and duration of grasping (seconds) respectively. It should be noted that since the value of a is negative (a=-4.27) in (Eq2.5), the general population fit would show negative necrosis at zero stress, which is biologically impossible. De et al. [9] held the compression stresses for Duration at 10, 30 and 60 seconds respectively and found the factor of duration had a very small effect. Thus Duration is not considered in our study and (Eq2.5) can be simplified as:

$$\%Necrosis = \frac{B * {\sigma_v}^C}{D^C + {\sigma_v}^C} \qquad \text{(Eq2.6)}$$

The parameter estimates for the best fit nonlinear mixed effect model are: B=81.42, C=4.67 and D=176.92 [9]. Then Eq 2.6 can be applied to compute the percentage of necrosis for each element in the FEA.

In 2D, the total equivalent tissue damage area $Damage_T$ in the entire area (5mm high×20mm wide) is calculated by:

$$Damage_{A_T} = \sum_i^N (\%Necrosis)_i * A_i \qquad \text{(Eq2.7)}$$

where $(\%Necrosis)_i$ refers to percent of necrosis at the i-th element. A_i refers to the contributory area of the i-th element. In 2D, the sum of the A_i is equal to 5mm high×20mm wide=100 mm². In 3D, the total equivalent tissue damage volume is 2000 mm^3 (5mm high×20mm wide×20 mm thick) and damage volume is calculated by the following equation:

$$Damage_{V_T} = \sum_i^N (\%Necrosis)_i * V_i \quad \text{(Eq2.8)}$$

where V_i refers to the contributory volume of the i-th point.

In order to investigate the relationship between total tissue damage and total stress, the integrated von Mises stress, $Stress_{A_T}$ in 2D space and $Stress_{V_T}$ in 3D space, is calculated similarly:

$$Stress_{A_T} = \sum_i^N (\sigma_{A,i} * A_i) \quad \text{(Eq2.9)}$$

$$Stress_{V_T} = \sum_i^N (\sigma_{v,i} * V_i) \quad \text{(Eq2.10)}$$

$\sigma_{v,i}$ refers to the von Mises stress at the the i-th node.

2.4 Results

Four examples of the calculated von Mises stress distribution under 2mm compression displacement with various boundary conditions are given in Figure 2.4A-D. For the 2D plane strain model, stress in 80% of the area directly beneath the grasper was over 300 kPa (Figure 2.4A). For 2D plane stress, most of the stress in the area directly beneath the grasper was around 80 kPa (Figure 2.4B). For both the 3D thin membrane cut plane and the full 3D cut plane, the stress on the contact surface peaked at the two grasper corners to over 300 kPa, and reduced in the middle. Directly beneath the grasper, both 3D cut plane models had stress value around 200 kPa.

After mapping stress to percentage necrosis of each element area using Eq2.5, we created a computed necrosis distributions in 3D space. One plotted example is shown in Figure 2.5, which indicates that the stresses around the corners and edges at the grasper-tissue contact surface contributed most to the tissue damage (red color). The tissue damage decreased with the

increasing distance from the contact surface, but remained localized in XZ plane to the region of contact.

A) 2D Plane strain. Meshing size=0.05mm;

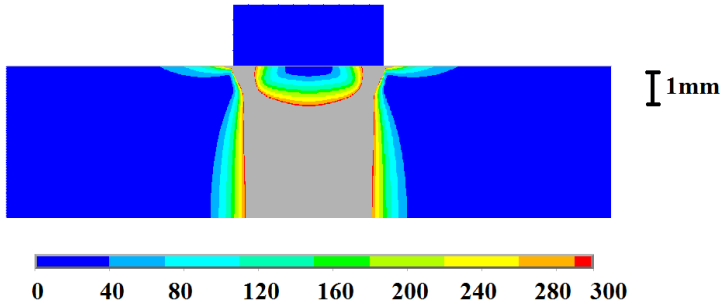

B) 2D Plane stress. Meshing size=0.05mm;

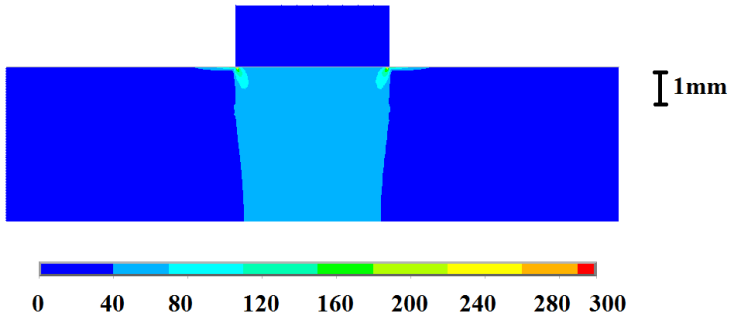

C) 3D thin membrane. Cut plane. Meshing size=0.05mm;

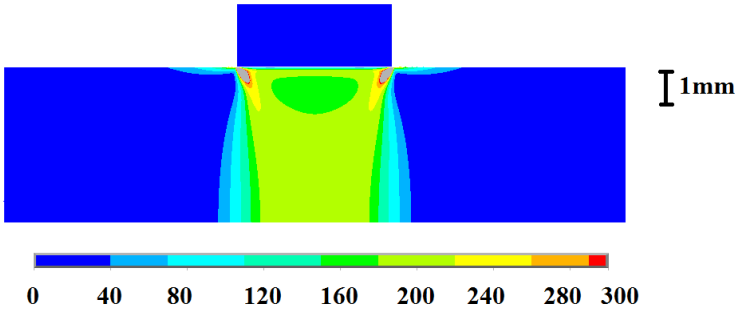

D) Full 3D. Cut plane. Meshing size=0.2mm;

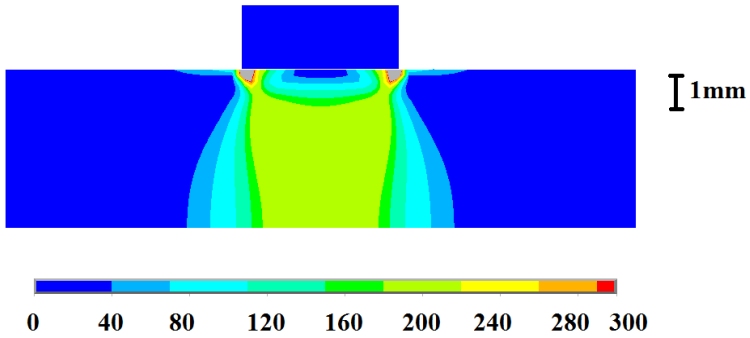

Figure 2.4 von Mises stress plot of liver tissue plane using nonlinear material properties. Color scale is in kPa. The applied displacement is Uy=-2mm (squeezing downward). Areas with stress more than 300 kPa are shown in silver grey. The deformation of tissue is not shown.

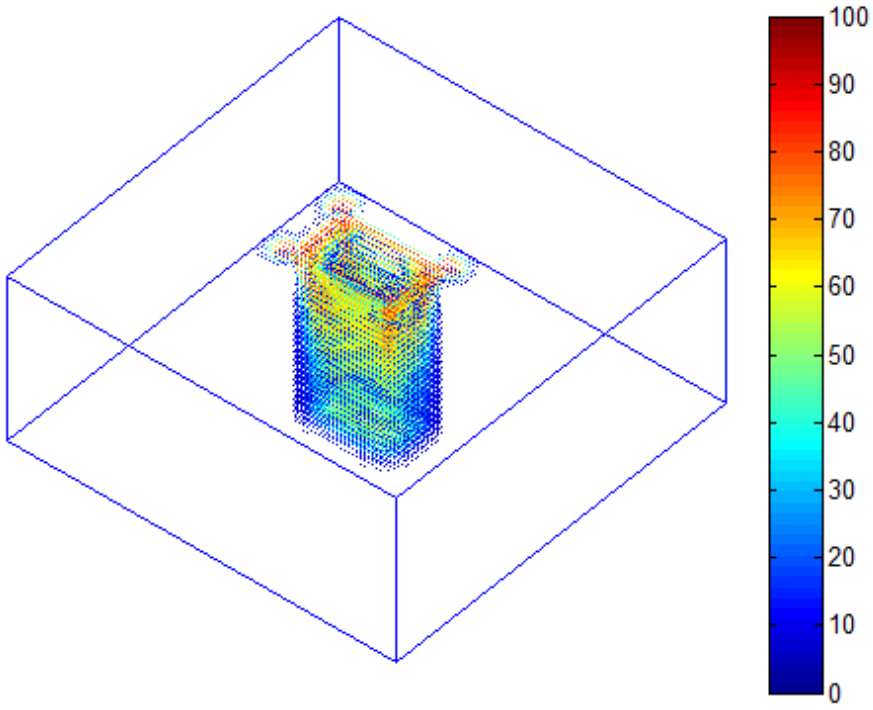

Figure 2.5 Full 3D contour of tissue damage in term of necrosis percent (%). Nonlinear material property is derived from MEG in vivo experiments. The meshing size of tissue is 0.2mm. The applied displacement is Uy=-2mm.

The integrated von Mises stress was calculated through adding up each element's von Mises stress multiplied by its contributory area (Eq 2.9 & Figure 2.6A). The tissue damage in the form of necrosis percentage was calculated using Eq2.5 (Figure 2.6B). For each displacement shown in Figure 2.6A and 2.6B, both integrated von Mises stresses and necrosis percentage of 3D thin membrane model were closest to those of full 3D model, with peak differences of 6% and 17% respectively. However, the computational time for 3D thin membrane was only 0.2% of the time for the full 3D model. Both the 3D thin membrane and the full 3D model yielded results that fell between 2D plane strain (upper limit) and 2D plain stress (lower limit).

Due to the nonlinear property of the necrosis-stress curve, the ratio of integrated von Mises stress for the full 3D model over 2D plane model was different from that of the necrosis percentage. For example, at the displacement Uy=-1.8mm, the 2D plane strain model yielded integrated von Mises stress 0.4 times more than the full 3D model while its calculated necrosis percentage was 1.1 times more than that of full 3D model.

A) Integrated von Mises stress with various boundary conditions;

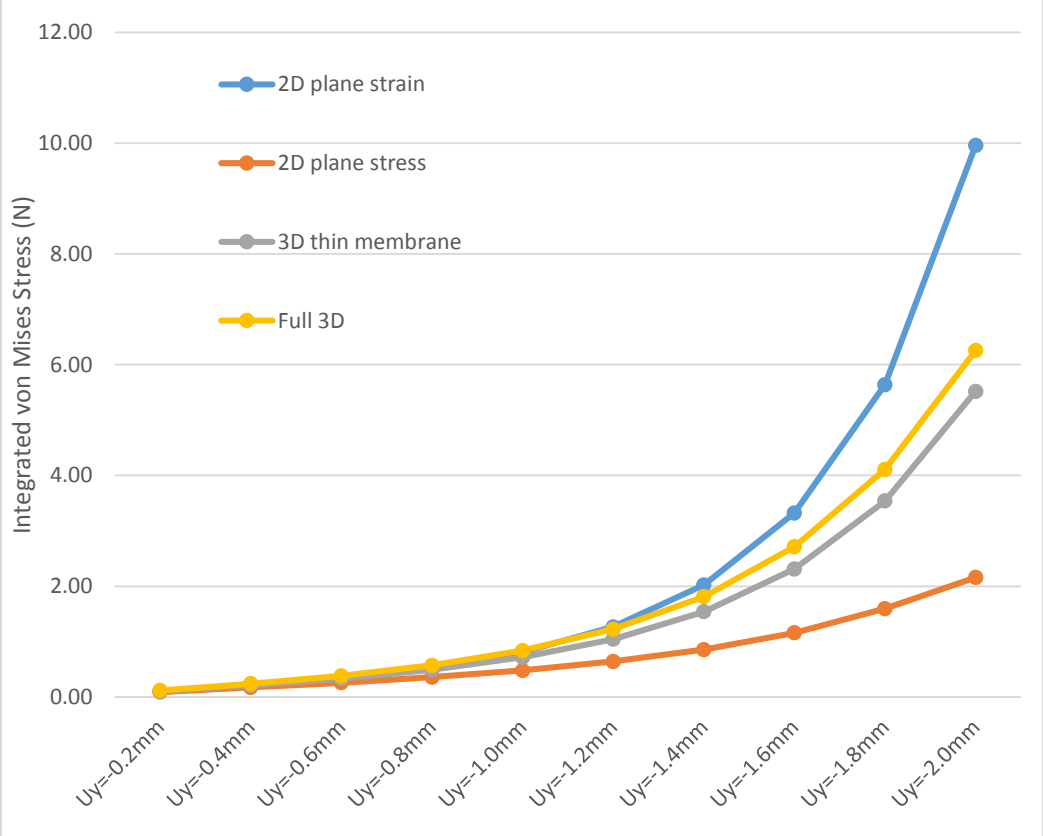

B) Equivalent tissue damage area percentage with various boundary conditions.

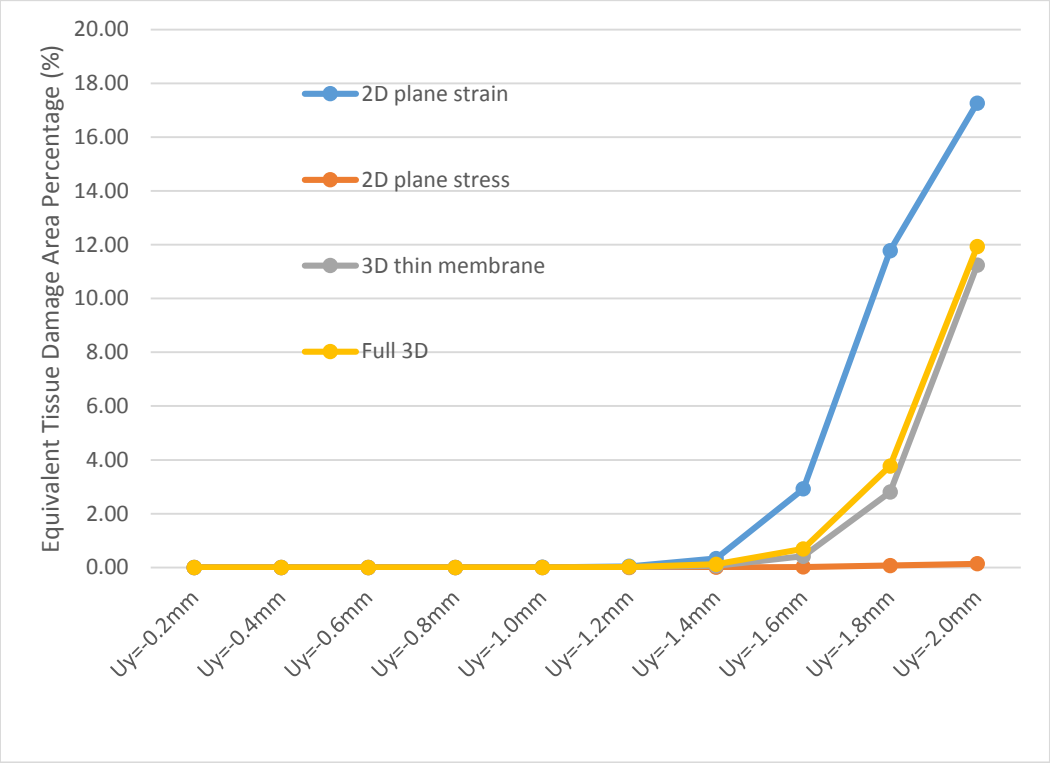

Figure 2.6 Integrated von Mises stress and tissue damage area percentage in 2D space with nonlinear tissue properties derived from MEG in vivo experiments.

A histogram showing the element percentage for three levels of von Mises Stress (Figure 2.7A-B) was calculated for different Ogden model parameters corresponding to the three of Rosen et al.'s experimental conditions (Table 2.1). Figure 2.7A showed that in full 3D space, the results of the model parameters derived from MEG in vivo and MEG in vitro tests had the similar stress distribution in all three ranges. The model parameters derived from MTS in vitro yielded slightly less percentage of stress at lower compression (higher stretch) range, but higher percentage of stress at higher compression (lower stretch) range. Similar trends were seen in 3D cut plane space (Figure 2.7B). The volume percentages of liver tissue damage in full 3D space for these

three material properties were also calculated (Figure 2.8). The results indicated similar tissue damage with MEG in vivo and MEG in vitro; also for each displacement step, model parameters derived from MTS in vitro yielded more tissue damage than both MEG in vivo and MEG in vitro.

A) Histogram of stresses in 3D space;

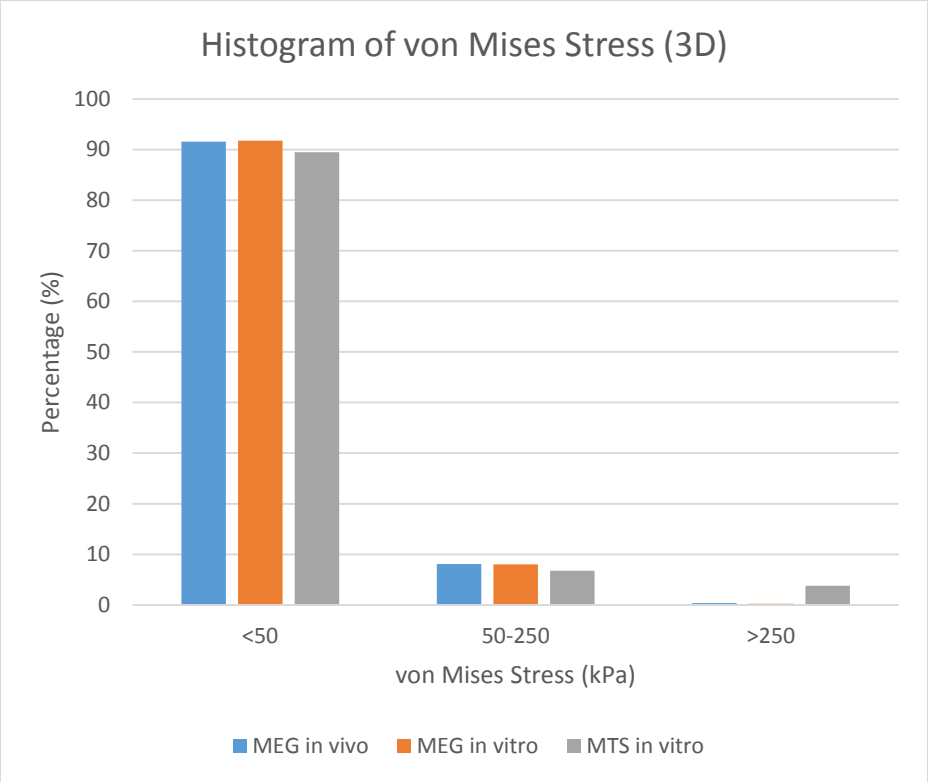

B) Histogram of stresses in 3D cut plane space;

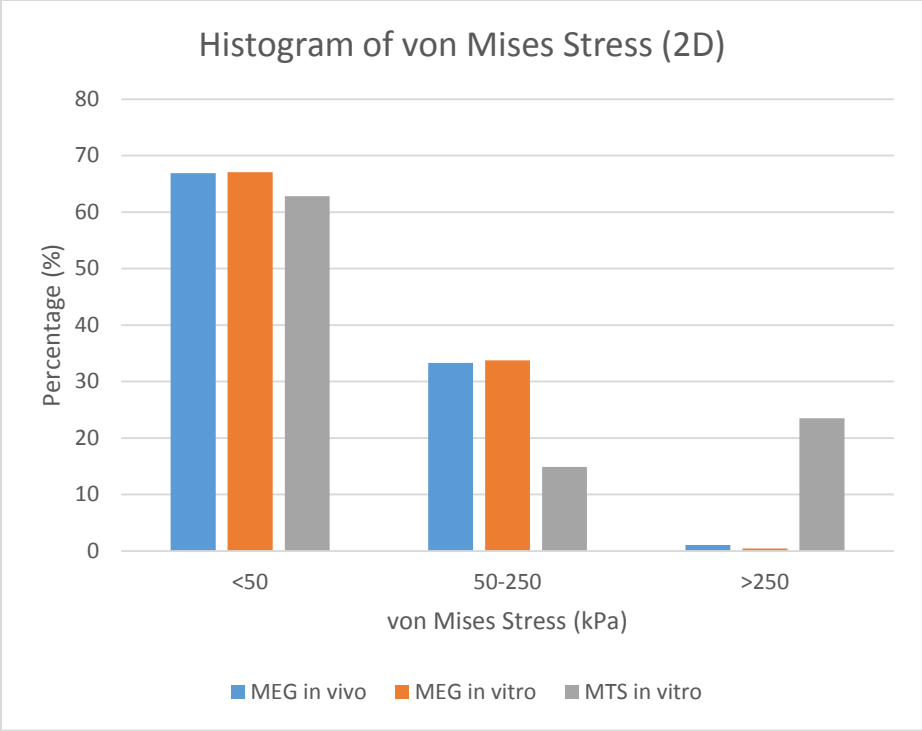

Figure 2.7 Histogram of von Mises stresses of liver tissue using nonlinear material properties derived from MEG in vivo, MEG in vitro and MTS in vitro experiments. The meshing size of tissue is 0.2mm. The applied displacement is Uy=-2mm.

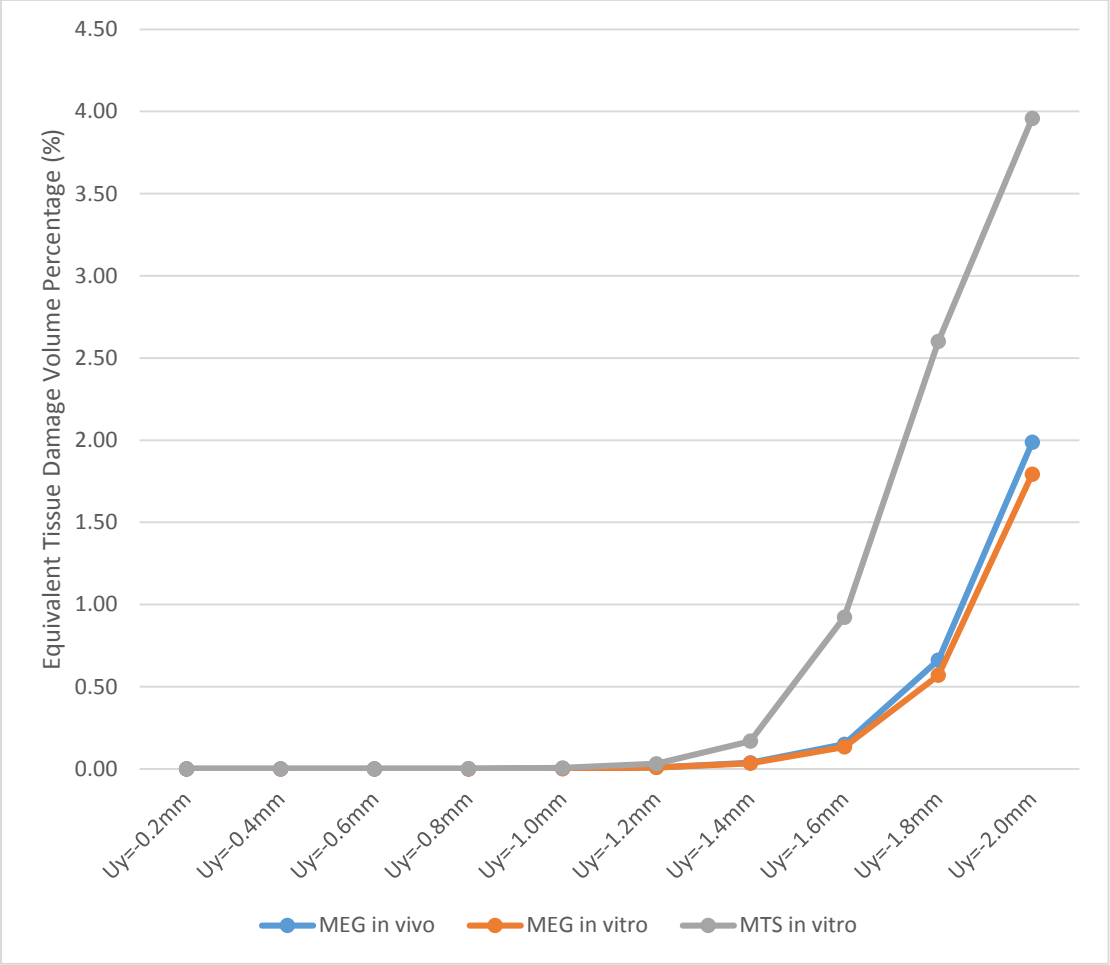

Figure 2.8 Equivalent tissue damage volume percentage with various nonlinear material properties. Full 3D model.

The integrated von Mises stress and predicted tissue damage area were calculated for uniform and refined meshing size of liver tissue. The results indicated that both integrated force and damage were only slightly impacted by the two meshing methods. However, for each displacement step, the calculation time was decreased by 72%-85% with the refined meshing size method.

2.5 Discussion and Conclusions

As far as we know, our study is the first to match a continuum mechanics Ogden model with in vivo uniaxial experimental data of liver. Also it is the first to use nonlinear tissue properties to predict tissue damage resulting from grasping in RMIS. The technique explored in this study can be useful for researchers to develop and test various design of graspers for improving patient safety and surgeon training. Instruments which can automatically display the tissue damage may decrease surgical complications. The surgical simulator performance can be improved by reflecting more realistic tissue material properties and predicting tissue damage for the student.

The influence of the boundary and material assumptions made in our liver tissue damage model of grasper-tissue interaction was studied using geometrically nonlinear finite element analyses with 2D plane strain, 2D plane stress, 3D thin membrane and full 3D models. Three different nonlinear material properties were derived from published in vivo and in vitro studies. The von Mises stress distribution, integrated von Mises stress and equivalent tissue damage percentage were compared for various geometrical boundaries and material properties. In order to investigate the meshing sensitivity of the FE model, the results from two meshing methods were recorded.

Our results showed that results from the 2D plane strain and 2D plane stress models formed the upper and lower bound of the results obtained from full 3D model cut plane. The results from the 3D thin membrane model were very close to the results from the full 3D model in the center 2D cut plane (Figure 2.6).

We found that both von Mises stress distribution and tissue damage were impacted by the nonlinear material Ogden model parameters in our data set. The results from MEG in vivo and MEG in vitro were close but there exist significant differences between them and the results from MTS in vitro especially at larger strains. With the MTS parameters, computations yielded more area with higher stress. As a result, the calculated tissue damage percentage was much higher for MTS in vitro. The significant differences between MEG and MTS results may be caused by different experimental testing conditions between MEG and MTS tests, such as differences of loading controls and boundary conditions. While this variability makes finding a

universal numerical model of tissue damage difficult, it is worthwhile to check the consistence of the experimental conditions of stress-damage tests with those of strain-stress tests for a more accurate prediction of liver tissue damage.

3D models clearly represent allow for more accurate representation of practical problems. However, full 3D FEA consumes much more modeling and computational time than 2D FEA. Our study indicated that a 3D thin membrane model may be a good alternative to full 3D model since it can yield the closest results to full 3D model while dramatically reducing the computational time by 99.8%. It was also found that refining meshing can reduce computational time by over 70% and have little impact on the results.

Limitations and Future Directions

Our refined meshing tissue model calculation was not able to converge if the applied displacement was larger than 1.4 mm, i.e. 28% percent vertical applied strain. Some approaches we tried to overcome this computational difficulty included curving the edge of the grasper, adjusting the computational parameters normal penalty stiffness (FKN) and penetration tolerance (FTOLN), decreasing the sub-step of displacement, and applying other algorithms in ANSYS, but model convergence beyond 28% strain was not obtained.

The liver tissue material in this study was assumed to be isotropic and homogenous. Additionally the tissue's mechanical properties were assumed not to change after the tissue cell was damaged. In reality, the liver tissue is biologically complex and is composed of various substructures like stroma and hepatocytes with different stress-strain characteristics. After being damaged, the crushed vessels inside the tissue can cause blood loss and the dead tissue cells may release a number of chemicals, both of which would change the local material properties.

The present study discussed the stress concentrations and related the stress results to the tissue damage based on the tissue damage-stress function as studied by De et al. [9]. However, there may be different damage mechanisms. Recent research proposed excessive strain as another direct factor for initiating pressure-induced deep tissue injury [19, 20]. Future studies should also

compare the strain with stress concentration and which factor has a stronger correlation with the measured tissue damage.

With additional in-vivo validation studies, we hope to develop an accurate FE model with more feasible computational time, by which the tissue damage resulting from mechanical compression in RMIS can be displayed to surgeons in real-time. Also it could improve the surgical simulator performance for the student or professional. Researchers can use the 3D computational models to rank different designs of grasper performance while causing the least damage, or they can use a computationally efficient 2D model for early warning during a procedure. In a relative measurement, the absolute accuracy is less important than relative rankings within each model. A computationally efficient model may be used with force sensing and possibly machine vision (segmentation and simple measurements) to provide an early warning system for liver damage during robotic surgery.

Acknowledgement

This research was funded by NSF (60167194). We would like to acknowledge Dr. Eric Seibel, Department of Mechanical Engineering, University of Washington for his comments and advices in this study. Special thanks to Sophia Hannaford for editing.

2.6 References for Chapter 2

[1] T Hu, G Tholey, JP Desai, AE Castellanos. Evaluation of a Laparoscopic Grasper with Force Feedback. Surgical Endoscopy, 18(5): 863-867, 2004.

[2] M MacFarlane, J Rosen, B Hannaford, C Pellegrini, M Sinanan. Force feedback grasper helps restore the sense of touch in minimally invasive surgery. Journal of Gastrointestinal Surgery, 3(3):278–285, 1999.

[3] J Rosen, B Hannaford, M MacFarlane, M Sinanan. Force Controlled and Teleoperated Endoscopic Grasper for Minimally Invasive Surgery - Experimental Performance Evaluation. IEEE Transactions on Biomedical Engineering, 46:1212-1221, Oct, 1999.

[4] G. Tholey, JP Desai, AE Castellanos. Force feedback plays a significant role in minimally invasive surgery: results and analysis. Annals of Surgery. 241(1):102–109, 2005.

[5] K Vakili, MS Flander, TR Sepp, MCorral, JD Diaz, A Slocum, GSL Teo. Design and Testing of a Pressure Sensing Laparoscopic Grasper. Proceedings of the 2011 Design of Medical Devices Conference DMD2011. April 12-14, 2011, Minneapolis, MN, USA.

[6] N Famaey, E Verbeken, S Vinckier, B Willaert, P Herijgers, J Vander Sloten. In vivo soft tissue damage assessment for applications in surgery. Medical Engineering and Physics, 32:437–443, 2010.

[7] N Famaey, J Vander Sloten, E Kuhl. A three-constituent damage model for arterial clamping in computer-assisted surgery. Biomechanics and Modeling in Mechanobiology, DOI: 10.1007/s10237-012-0386-7, 2012.

[8] S De, J Rosen, A Dagan, B Hannaford, P Swanson, M Sinanan. Assessment of tissue damage due to mechanical stresses. International Journal of Robotic Research, 26:1159–1171, 2007.

[9] S De. The Grasper-Tissue Interface in Minimally Invasive Surgery: Stress and Acute Indicators of Injury. Ph.D. Thesis, University of Washington, 2008.

[10] YB Fu, CK Chui. Modeling and Simulation of Porcine Liver Tissue Indentation using Finite Element Method and Uniaxial Stress-Strain Data. Journal of Biomechanics, http://dx.doi.org/10.1016/j.jbiomech.2014.04.009.

[11] YC Fung. Biomechanics: mechanical properties of living tissue. Springer, Berlin Heidelberg, New York, 1981.

[12] FJ Carter, TG Frank, et al. Measurements and modeling of the compliance of human and porcine organs. Medical Image Analysis. 5(4), 231-236, 2001.

[13] C Chui, et al. Combined compression and elongation experiments and non-linear modeling of liver tissue for surgical simulation. Medical and Biological Engineering and Computing. 42(6):787–798, 2004.

[14] Z Gao, K Lister and JP Desai. Constitutive modeling of liver tissue: experiment and theory. Annals of Biomedical Engineering, 38(2):505, 2010.

[15] Berkay Yarpuzlu, et al. Correlation between the mechanical and histological properties of liver tissue. Journal of the Mechanical Behavior of Biomedical Materials, 29:403-416, 2013.

[16] J Rosen, JD Brown, S De, M Sinanan, B Hannaford. Biomechanical properties of abdominal organs in vivo and postmortem under compression loads. Journal of Biomedical Engineering, 130(2): 021020, 2008.

[17] Krueger et al. Comparison of 2D finite element modeling assumptions with results from 3D analysis for composite skin-stiffener debonding. Composite Structures, 57:161-168, 2002.

[18] RW Ogden. Large deformation isotropic elasticity: on the correlation of theory and experimental for compressible rubberlike solids. Proceedings of the Royal Society of London, Series A (Mathematical and Physical Sciences), 328(1575), 567-583, 1972.

[19] RGM Breuls, CVC Bouten, et al. Compression induced cell damage in engineered muscle tissue: an in vitro model to study pressure ulcer aetiology. Annals of Biomedical Engineering, 31, 1357-1364, 2003.

[20] KK Ceelen, A Stekelenburg, et al. Compression-induced damage and internal tissue strains are related. Journal of Biomechanics, 41(16), 3399-404, 2008.

[21] L Cheng, B Hannaford. Evaluation of Liver Tissue Damage and Grasp Stability Using Finite Element Analysis. Computer Methods in Biomechanics and Biomedical Engineering, Nov 19, 1-10, 2014, available online.

[22] RA Romeed, SL Fok, NH Wilson. A comparison of 2D and 3D finite element analysis of a restored tooth. Journal of Oral Rehabilitation, 33: 209–215, 2006.

[23] ANSYS® Academic Research, Release 16.0, Help System, Coupled Field Analysis Guide, ANSYS, Inc.

Chapter 3. Feature Descriptors of Tissue Deformation Caused by Tissue-Grasper Interaction

3.1 Overview

This paper studies the feasibility of estimating the applied grasping force from the information of tissue deformation. We are interested in the tissue deformation caused by tissue-tool interaction. We propose two feature parameters, length and depth, to describe the size of tissue deformation. The two descriptors are extracted firstly by the imaging techniques for porcine liver deformation in vitro and then marked by finite element analysis (FEA) in simulation environment. The results indicate the proposed feature descriptors are correlated to the applied force. Also our test results suggest such functional relations be useful in guiding surgeons to apply safe grasping force to reduce the risks of tissue damage.

3.2 Introduction

The development of RMIS has resulted in growing interest in research to improve surgeon training and proficiency as well as patient safety [1]. Current design of RMIS eliminates all natural haptic feedback since the surgeons no longer manipulate either the tissue or the instrument directly [2]. The goal of force feedback studies in RMIS is to provide a feeling for surgeons that they are not operating surgery robots remotely but instead are physically contacting patients directly. Such devices usually include haptic sensors which can acquire force signals on the patient side and display devices which can transfer signals to surgeons [2]. Both parts working together can guide surgeons to apply a “suitable” force to manipulate tissue: strong enough to avoid slippage but not too high to damage the tissue.

Commercially available force sensors have been used to measure grasping forces accurately. Several attempts have successfully been made by attaching specialized force sensors to the jaws of an existing grasper [3] or redesigning the instruments [4]. However, severe environmental

** This is a modified version of the manuscript in preparation for journal submission.

constrains in RMIS, like size, biocompatibility, and sterilizability, prevent wide use of such sensors. Besides, it is costly to install additional sensors to current RMIS instruments which are frequently replaced.

There exist many works quantitatively relating the applied force to the deformation in RMIS. However, most of them are either for: 1) surgery simulation in which applying mechanical loads like force or displacement, simulated tissue deformation would be presented in a virtual environment [5-7]; 2) for identifying tissue in which soft tissue experiments were performed to measure surface deformation and force responses resulting from indentation loading depending on various indentation depths. Then inverse finite element modeling (IFEM) was used for tissue parameter identification [8, 9].

A few other researchers proposed that the applied external force can be predicted via use of a neural network from the superposition of basic volumetric deformation modes computed off-line [10, 11]. Though such methods can achieve approximate accuracy for surgery simulation, they may not be suitable for estimating force feedback since they require the whole volumetric shape of organs, often not measurable during RMIS. A recent study applied a virtual-template-based algorithm to calculate the penetration depth through monocular images. Then the nonlinear strain-stress tissue model was used to estimate the interaction force between MIS tool and lamb liver in vitro [23]. However, specular light reflection on the tissue surface made it hard to select and match feature points for the algorithm without human intervention, which limits its application in providing force feedback real-time.

An essential part of deformation based force computation is measuring the deformation. The most measured parameter of tissue deformation is the depth, which has been related to the compression force in many studies [19, 20]. However, the depth is only one-dimensional (1D) while tool-tissue interaction in grasping is three-dimensional (3D). Fig.3.1A-B illustrate the 3D deformation of lung lobe due to the grasper-tissue interaction in the selected region. In this study, we adopt the most commonly used technique in clinical assessment of wound, linear measurement, to approximately represent the size of tissue deformation. In this paper, a three-

dimensional (3D) thin membrane model is studied to extract the two feature descriptors of length and depth.

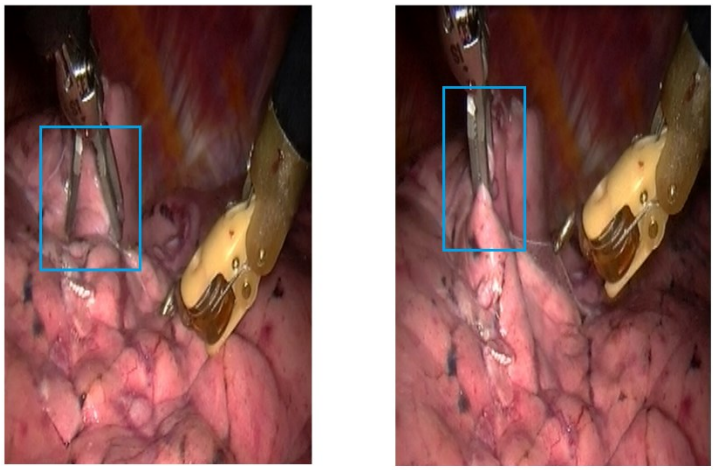

(A) **(B)**

Figure 3.1 Captured images from video of in vivo lung lobectomy procedure (downloaded from the Hamlyn Centre Laparoscopic / Endoscopic Video Dataset, Imperial College, UK [14]). The blue block marked the region of interest before (A) and after grasping (B).

The objective of the paper is to study the feasibility of estimating the applied force by detecting the length and depth of tissue deformation due to grasping. Two methods are performed for achieving this goal:

1) In vitro experiments.

Two long standing approaches: shape from shading (SFS) and stereo 3D reconstruction methods are tested on porcine liver in vitro. Though SFS method can only recover relative orientation information instead of the information in a metric coordinate, it can work together with the stereo technique to overcome this drawback [18]. Thus two high-definition webcams are set to capture the stereo images.

2) FEA simulation.

A major challenge for accurate FEA simulation is to establish a validated tissue model. It is well known that most soft tissue is nonlinear, inhomogeneous and viscoeleastic [12]. Among the soft tissue, liver is considered to be a good model for continuum mechanics study. Due to

its uniform histology cross sections, it is approximately isotropic and homogenous [13, 15]. If the strain rate effect is excluded, i.e., the strain only changes with location but not with time, the mechanical response of liver tissue can be described by nonlinear elastic model [16]. In this study, we applied our previously developed continuum mechanical model of porcine liver for the FEA simulation [17];

Our results prove that the feature descriptors of tissue deformation, length and depth, are both quantitatively correlated to the applied force. This result indicates the possibility of estimating the grasping force by using the available image-processing techniques, even when the depth information is missing. The study can be useful for researchers to develop new force feedback system for robotic grasping.

3.3 Methods-In Vitro Experiment

3.3.1 *Calibration of Force Sensor*

Fig 3.2A shows the apparatus designed to measure compressive force of grasping with a pair of low profile force sensors (FSS015WNSB, Honeywell). This force sensor exhibits a change of voltage related to force. Coins were placed to rest on the thin steel plate inside of the grasper surface (Figure 3.2 B). The weight of the coins increased from 0 to 120g gradually, i.e. the applied force of gravity increase from 0 to 1176 mN. The voltage output of the force sensor and weight of coins were recorded simultaneously. A plot of the weight of coins, Fc (mN), versus the force sensor measurements, V_{Blue} (mN) for the blue jaw and V_{Red} (mV) for the red jaw, is shown in Figure 3.3. The equations for the linear fit are

$$Fc = 74.37 * V_{Blue} + 37.3 \quad \text{(Eq 3.2)}$$

$$Fc = 72.26 * V_{Red} + 181.3 \quad \text{(Eq 3.3)}$$

The coefficient of determination R^2 for the force measurement was 0.9965 for the blue jaw and 0.9963 for the red jaw.

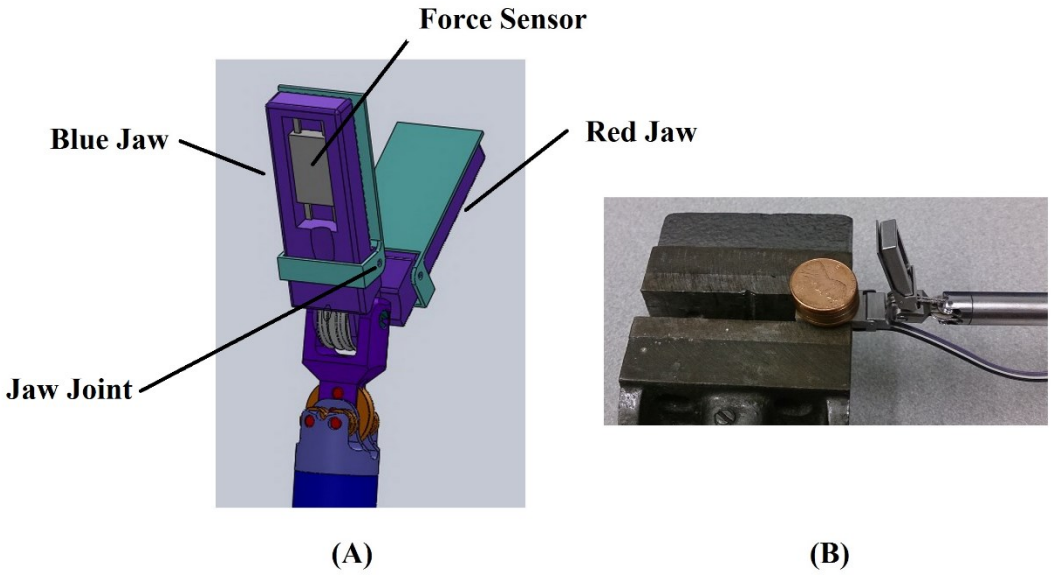

Figure 3.2 (A) Illustration of prototype design of the force sensors mounted to the grasper jaws. (B) A photograph of the calibration of force sensor with one-cent coins.

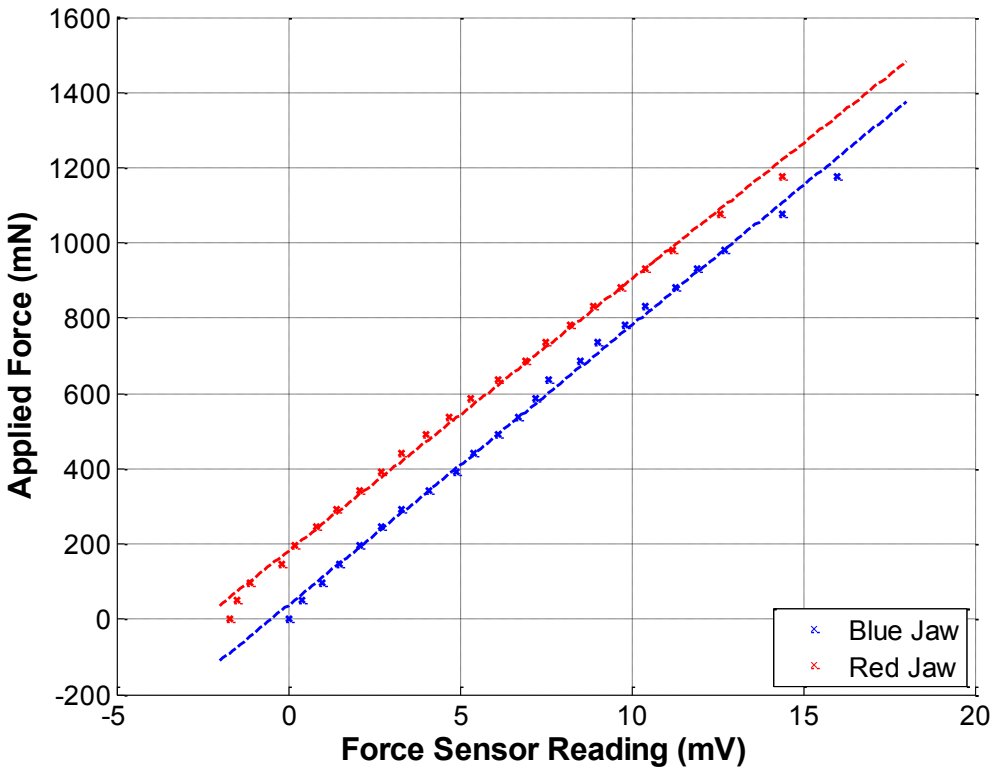

Figure 3.3 Applied force of gravity versus voltage reading of force sensor. Measurement points are indicated by crosses. The linear fits described by Eq 3.1 and Eq 3.2 are also shown as dash blue and red lines respectively.

3.3.2 *Experimental Setup*

Three packages of porcine livers were purchased from three different local grocery stores to make sure they are coming from different pigs. Then one sample from each package was cut to have similar 3D shape. Fig. 3.4A shows the in vitro experimental setup in this study. A customized manufactured Raven II™ (Applied Dexterity Inc., Seattle, WA) grasping tool assembly is placed on two aluminum brackets with its shaft leveled horizontally. The grasper jaws can be driven by rotating the spindles which are coupled to the jaws by steel cable. Two high-definition Microsoft LifeCam Studio (TM) cameras (Camera #1 and Camera #2) were fixed horizontally and vertically to capture the side and top view of the liver to be grasped. The Stryker™ Endoscoy Q-5000 Light Source is placed next to Camera #1 lens to simulate the RMIS illumination.

Initially the liver sample was placed on the tissue platform between the open grasper jaws with no torque added. The initial opening angles of both jaws for the three liver samples were set to be same. The jaws just slightly touched the liver sample, causing negligible deformation and we assume initial shape is underformed. Then the spindle was manually rotated to gradually close the grasper jaws. For each incremental step, one pair of images captured by Camera #1 and Camera #2 along with the output voltage of two force sensors were recorded simultaneously. All eight pairs of images were recorded for later image processing.

3.3.3 *Shape from Shading*

Shape-from-shading (SFS) is a classical passive method in computer vision for recovering the 3D shape of an object from single 2D greyscale image [24]. One major assumption for traditional SFS is that the objective surface is Lambertian, which means that the light is reflected evenly in all directions. However, due to the mucus layer of the soft tissue and high intensity of the light source, specular reflection commonly exists for RMIS images [18]. Specular reflections are also

well known property of surgical endoscopic image. In our experiment, we can see a number of white patches due to specular light reflection (Fig. 3.4C). For the case of a light source parallel to the camera, points on the white patches are called singular points whose surface normal direction is the same as the lighting direction [25].

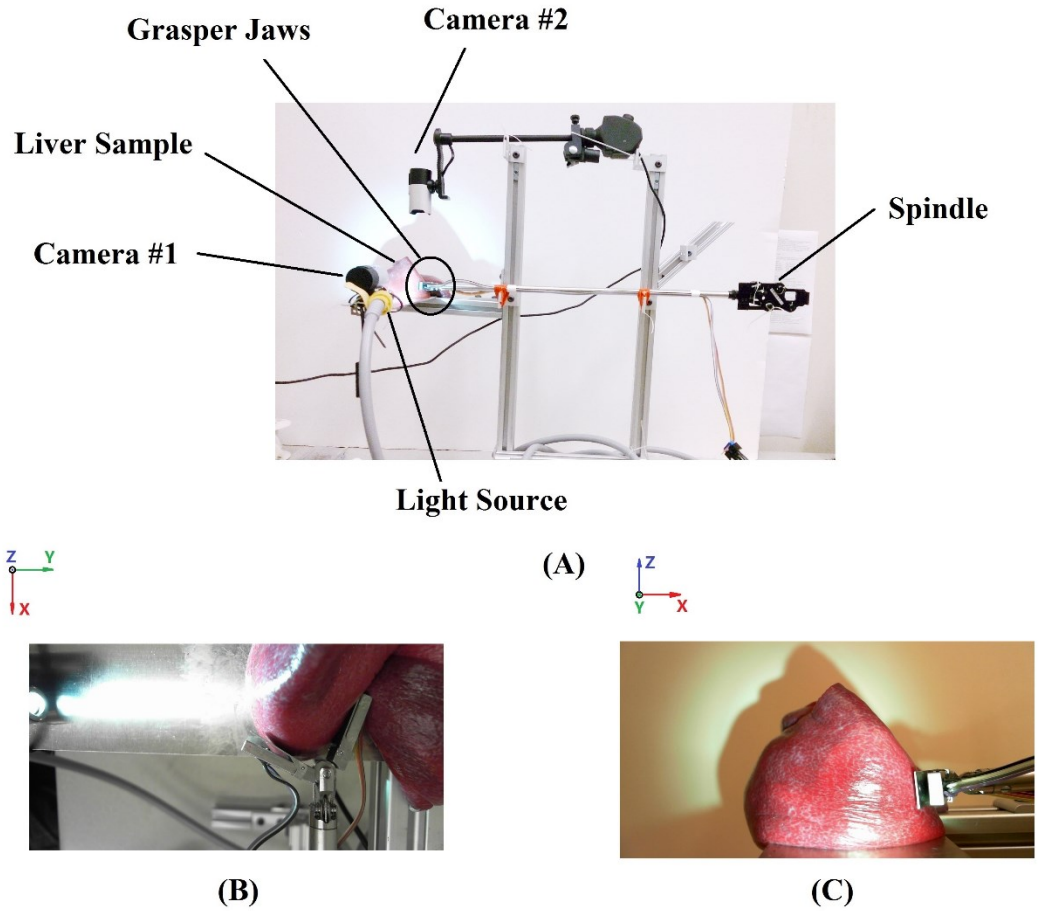

Figure 3.4 Experimental setup for testing porcine live in vitro (A) and the sample pictures captured by Camera #2 (B) and Camera #1 (C).

The singular points can be classified as convex, concave and saddle [26]. Although these points can cause significant error in recovering the depth data along the Y direction (Fig. 3.4C), they may be useful to reveal the deformed area projected on the XZ plane. To illustrate this effect, we took images from a plane and cylinder using the setup (Figure 3.5). The point P has the same coordinates on both left and right images. Comparing the images of flat and cylinder surfaces, the attribution of point P changes from singular to non-singular as curvature is increased, which

indicates deformation has happened (flat surface to cylinder's curved surface). Similarly, if the attribution of point P changes from non-singular to singular, it also indicates deformation.

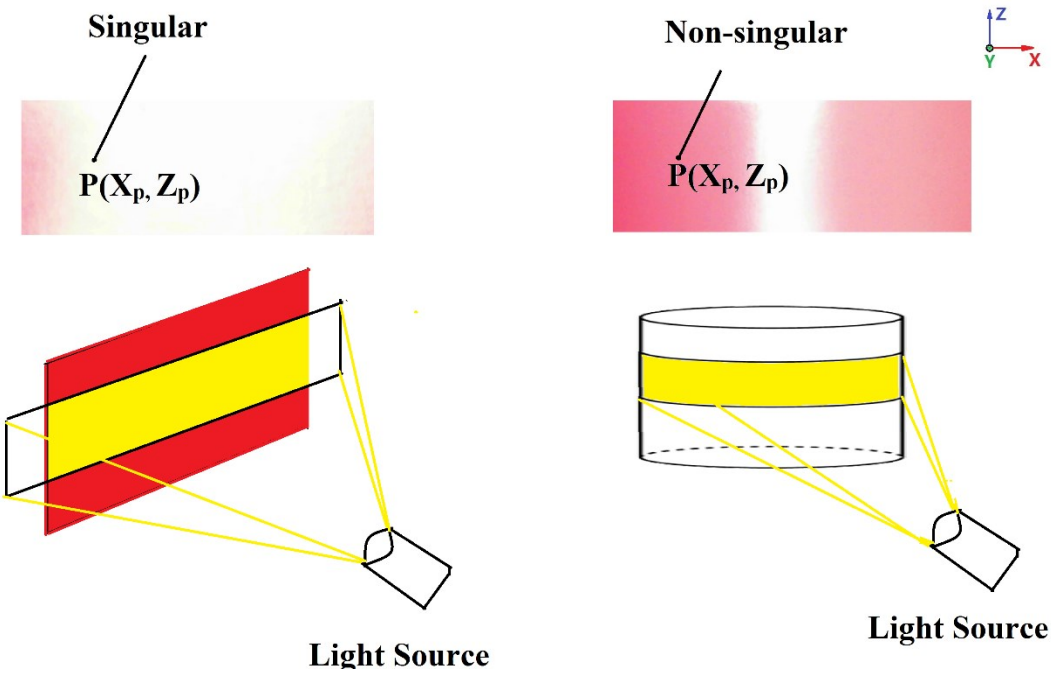

Figure 3.5 Illustration of singular and non-singular points. Left: red electrical tape on a flat surface whose normal direction is approximately parallel to the lighting direction. Right: a cylinder covered with the same tape.

In our in vitro liver sample measurements, we compared the positions of singular points between the images taken by Camera #1 and track the deformation area on the XZ plane. We first converted the RGB image to grey intensity image and adjusted the exposure rate and contrast ratio to highlight the areas with singular points (Fig. 3.6A). By overlaying the image of deformed tissue with the original undeformed one, we can find the areas where singular points have shifted. The length of deformation in the camera frame P_L is the distance between the left most point of the shifting area identified by the moved singular points along the jaw midline and the tip of jaw. By placing a ruler close to the tissue sample and parallel to the camera lens, we found that 1mm in space was mapped to 102 pixels in the camera frame. Thus the length of deformation in space L=P_L/102. Since the distance between Camera #1 and tissue sample is much longer than the depth of deformation, the impact of depth field on L is negligible.

We also recorded the opening angle of the moving jaw (blue jaw), θ, for each loading step (Fig 3.6B). As the initial opening angle is θ_0 and jaw length, L_{jaw}=30mm. The depth of deformation D can be calculated as:

$$D = L_{jaw} * (\sin\theta_0 - \sin\theta) \quad \text{(Eq 3.4)}$$

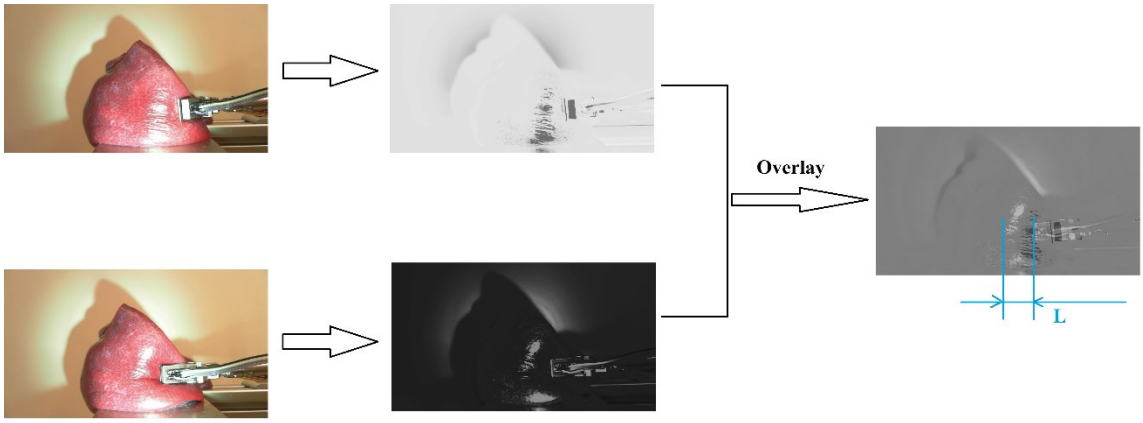

(A)

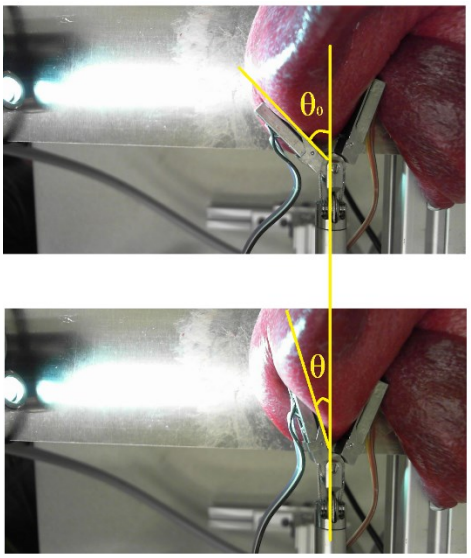

(B)

Figure 3.6 Indicators of length and depth for in vitro experiments. (A) Singular points are marked in black for the undeformed surface while they are marked in white for the deformed surface. (B) Opening angles of the blue grasper jaw are θ_0 before deformation and θ after deformation respectively.

3.4 Methods-Finite Element Analysis

3.4.1 *Biomechanical Model for Tissue*

The modeling methods for this research are similar to a recent study [17] in which a three-dimensional thin membrane model were used to get accuracy comparable to 3D simulation, but computation time comparable to 2D. Soft tissue is often inhomogeneous and anisotropic and its compounds vary throughout the whole structure. Carter et al. found solid organs, particularly the liver and spleen, could be treated as approximately isotropic and homogenous [13]. Also because of the high water content of the liver tissue, we can consider it to be incompressible [16].

The modeling of continuum mechanics is the same with Section 2.3.1. We only list the equations below for reference.

$$\sigma = \beta(e^{\alpha\varepsilon^2} - 1) + \gamma\varepsilon \quad \text{(Eq 3.5)}$$

$$W_O = \sum_{i=1}^{N} \frac{\mu_i}{\alpha_i}[\lambda_1^{\alpha_i} + \lambda_2^{\alpha_i} + \lambda_3^{\alpha_i} - 3 + \frac{1}{d_i}(J-1)^{2i}] \quad \text{(Eq 3.6)}$$

$$W_O = \sum_{i=1}^{N} \frac{\mu_i}{\alpha_i}[\lambda_1^{\alpha_i} + \lambda_2^{\alpha_i} + \lambda_3^{\alpha_i} - 3] \quad \text{(Eq 3.7)}$$

$$\sigma_c = \sum_{i=1}^{N} \mu_i[\lambda_1{}^{\alpha_i} - \lambda_1{}^{-\alpha_i/2}] \quad \text{(Eq 3.8)}$$

Adopting the notation of Rosen et al. [19], with the compression load, σ_2=-σ and λ=1-ε, we then numerically fit Rosen et al.'s phenomenological stress-strain curves to Eq 3.5. The parameters for the least-square fitting 1st-order Ogden model are α_1=16.02 and μ_1=0.002934.

3.4.2 *Finite element model for tissue-grasper interaction*

Nonlinear finite element analyses are performed using ANSYS Mechanical APDL 14.0 under the 3D thin membrane assumption (Fig. 3.7). A series of key points are manually selected in the 2D RGB image to approximately sketch the liver shape on the XY plane. The meshing sizes and thickness of both tissue slice and grasper jaw are all set to 0.4 mm. The red jaw is fixed and the blue jaw can only revolve around the joint. The yellow portion of tissue is set to have no degrees

of freedom to help the convergence in simulation. The applied displacement at the tip of the blue jaw increases from 0 to 15mm with an increment of 0.03mm in the positive Y direction. For each displacement step, the coordinates of jaw tip (x_{jaw},y_{jaw}) are recorded. (x_0,y_0) represents the initial location of jaw tip. Because of tissue deformation upon the blue jaw's closing, some of the nodes on the tissue surface above the blue jaw tip will change along the X direction compared to their original position (when the applied displacement=0). We record the position of the left most node of tissue as (x_{m_0},y_{m_0}) and the coordinates of the left most node as (x_m,y_m) when deformation happens. The depth and of length of deformation on XY plane is $D_{XY}=|y_{jaw} - y_0|$ and $L_{XY}=|x_m - x_{m\_0}|$.

The principle of level is used to calculate the equivalent force applied on the sensor F_s as below:

$$F_s = \frac{\sum_{i=1}^{n} F_i L_i}{L_s} = \frac{\sum_{i=1}^{n} (\sigma_i A_i) L_i}{L_s} \qquad \text{(Eq 3.9)}$$

where the force at the i-th node $F_i = \sigma_i A_i$. A_i refers to the contributory area of the i-th point and is equal to 0.4mm×0.4mm=0.16 mm². σ_i represents the contact pressure at the the i-th node. L_i refers to the distance between the i-th node and the jaw joint connecting the thin steel plate to grasper body (see Figure 3.7B). The distance between the measurement point of force sensor and the jaw joint L_s=13.5 mm.

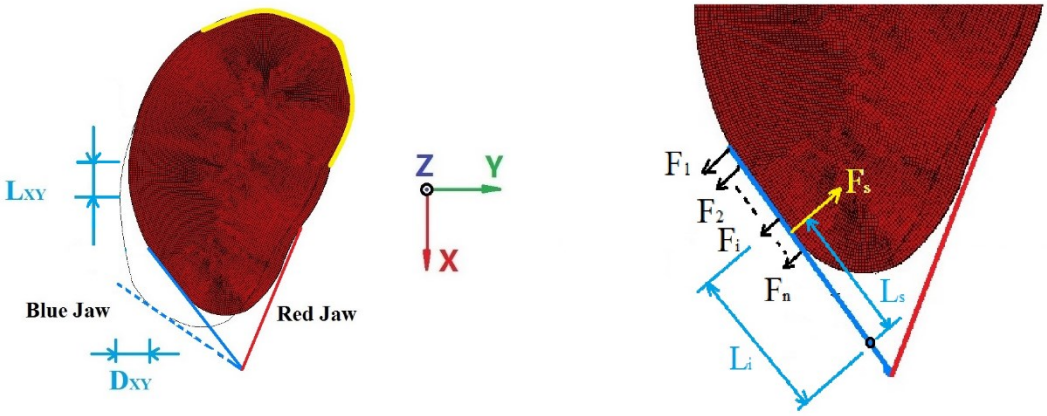

(A) (B)

Figure 3.7 A) Two feature descriptors of tissue deformation in simulation: length L_{XY} and depth D_{XY}. Underformed shape of tissue surface is indicated by lighter black lines. Dash blue line represents the initial position of the blue jaw. B) Illustration of equivalent force applied on sensor F_s.

3.5 Results

The measured force for both blue and red jaws with the length and depth of deformation are given in Figure 3.8A-B. For all three liver samples, the force on the blue jaw is more than the red jaw's for smaller deformation but becomes less than the red jaw's with increasing deformation. In Figure 3.8A, all six plotted curves have the pattern of an approximately exponential function, i.e. the grasping force increases much faster with higher magnitude of deformation. The force vs depth curves (Figure 3.8B) have similar curve patterns to the force vs length curve (Figure 3.8A).

Due to the empirical emphasis of this study, we adopt the phenomenological function similar to Eq 3.5 to fit to the experimental data:

$$F = p(e^{m(\frac{d}{30})^2} - 1) + q\frac{d}{30} \qquad \text{(Eq 3.10)}$$

where F is the mean grasping force of blue jaw and red jaw, $F=(F_{Blue}+F_{Red})/2$, d represents the length of deformation (Fig 3.8A), or depth of deformation (Fig 3.8B). For each curve fitting, d range from 0 to 30 mm. The experiment data was imported into MATLAB Curve Fitting Tool (Mathworks Inc.). Using the Levenberg-Marquardt algorithm (LMA) and least absolute residuals (LAR) method, we fit the parameters in Eq 3.10 with the coefficient of determination R^2 (see Table 3.1).

Table 3.1 The parameters for the least-square fitting phenomenological model under various in vitro experiment conditions.

Experiment Condition	Phenomenological Model Represented by Eq 3.10
Liver Sample #1, Length	m_1= 29.47, p_1 = 0.00028, q_1 = 0.0807, R^2=0.989
Liver Sample #2, Length	m_2= 6.396, p_2 = 1.181, q2 = 0.0079, R^2=0.992
Liver Sample #3, Length	m_3= 62.91, p_3 = 0.00015, q_3 = 0.0731, R^2=0.991

Liver Sample #1, Depth	m_4= 4.24, p_4 = 0.0802, q_4 = 0.036, R^2=0.992
Liver Sample #2, Depth	m_5= 15.12, p_5 = 0.0059, q_5 = 0.028, R^2=0.998
Liver Sample #3, Depth	m_6= 1.921, p_6 = 0.3075, q_6 = 0.040, R^2=0.991

Three examples of calculated von Mises stress distribution by FEA are given in Figure 3.9. For both blue and red jaws, the stress on the contact surface peaked at the jaw tips and decreased along the jaw. However, the stress distribution on the blue jaw was different from the red jaw. In Figure 3.9C, for the blue jaw, 1% of the stress on the contact area is over 300 kPa, 2% is between 80 kPa and 300 kPa, and 97% is below 80 kPa; for the red jaw, 6% of the stress on the contact area is over 300 kPa, 53% is between 80 kPa and 300 kPa, and the rest 41% is below 80 kPa.

The calculated force by FEA for both blue and red jaws vs the length and depth of deformation are given in Figure 3.10A. Similar to the in vitro experiments, the force on the blue jaw is more than the red jaw's for the lower deformation range but becomes less than the red jaw's for higer deformation range. Using the same curve-fitting method with Eq 3.10, we can get the parameters in Table 3.2 from the FEA computations. The plot in Figure 3.10B compares the deformation-force curves resulting from the FEA under various experiment conditions.

Table 3.2 The parameters for the least-square fitting phenomenological model obtained by FEA.

Deformation Descriptor	Phenomenological Model Represented by Eq 3.10
Length	m_L= 16.13, p_L = 1.18, q_L = -0.05174, R^2=0.9981
Depth	m_D= 8.065, p_D = 1.233, q_D = 0.01461, R^2=0.999

A) Measured grasping forces for both jaws with different length of deformation.

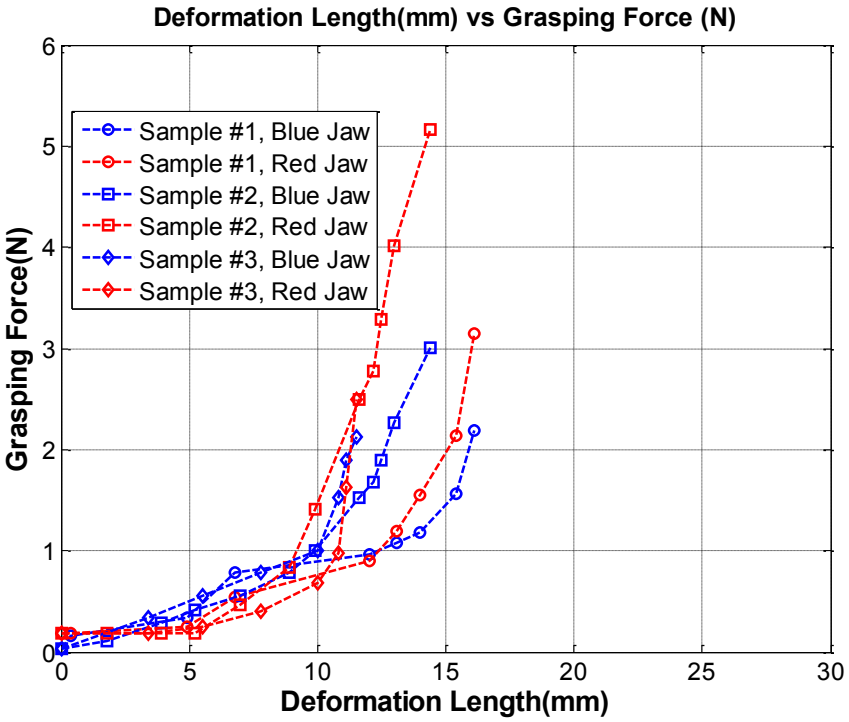

B) Measured grasping forces for both jaws with different depth of deformation.

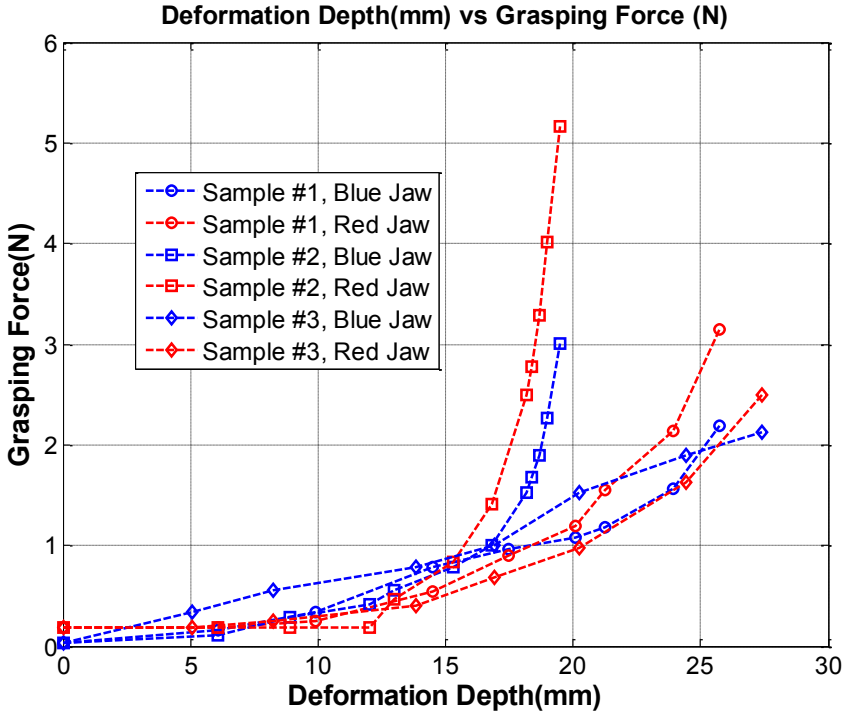

Figure 3.8

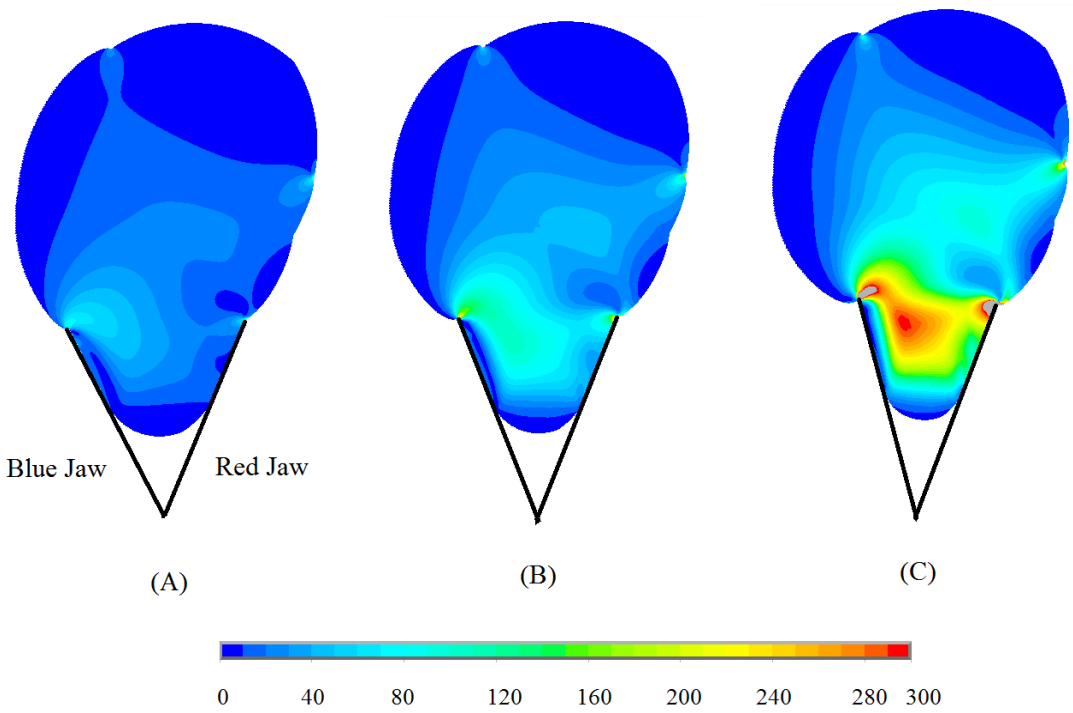

Figure 3.9 von Mises stress plot of liver tissue plane using nonlinear material properties. Color scale is in kPa. Areas with stress more than 300 kPa are shown in silver grey. The applied displacements are (A) Uy=4 mm, (B) Uy=8 mm, and (C) Uy=12mm (blue jaw squeezes the liver tissue rightward).

A) Calculated grasping forces for both jaws with different length and depth of deformation in FEA.

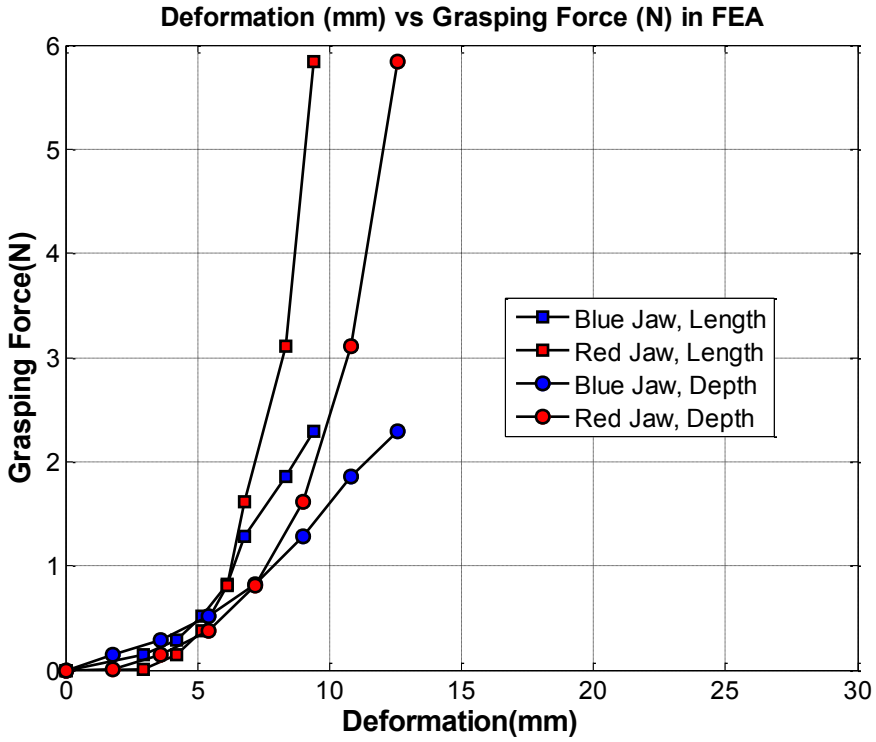

B) Best curve fitting under various experiment conditions.

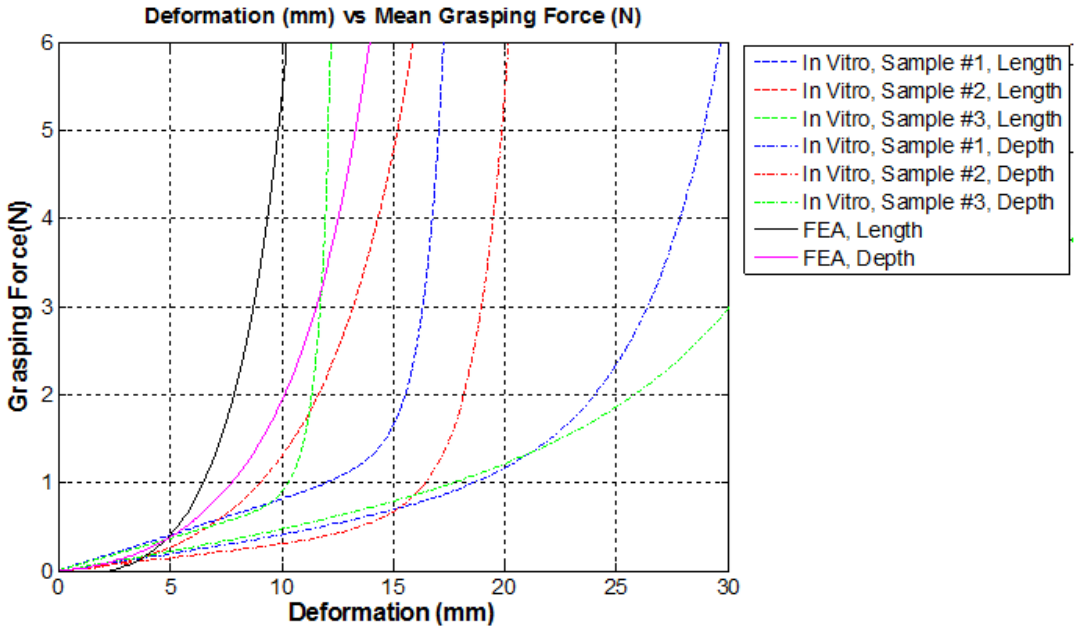

Figure 3.10

3.6 Conclusion and discussion

Grasping force prediction for RMIS through deformation and associated boundary conditions has been challenging due to experimental difficulties and computational complexity. As far as we know, our study is the first to capture surface deformation of liver as well as force responses at the grasper jaws similar to RMIS. The two feature descriptors of tissue deformation, length and depth, with respect to grasping force on three liver samples were obtained through stereo images in vitro. These data were fitted to a phenomenological function and compared to the simulation results of FEA. It was found that the best fitting curves of both in vitro experiments and FEA simulation have similar shape: stiffer at higher range of deformation than lower range. Thus with higher deformation magnitude, the grasping force is more sensitive to deformation.

We also observed that the calculated force through FEA was higher than that measured by in vitro experiments (Figure 3.10B). For example, when the length of deformation is 10 mm, the ratios of grasping force from FEA over that from in vitro experiments for the three liver examples were 6.6, 4.0 and 6.0 respectively. Similarly for the deformation depth of 10 mm, the ratios are 4.7, 6.2 and 4.0. The difference in forces may be due to the variety of the mechanical property of tissue. By testing more liver samples, we may get in vitro experimental data with statistically significance; this could be an interesting extension of our work. FEA Ogden models parameters were derived from Rosen et al.'s measurements in vivo. In vivo experiments are also suggested.

Our results show the force on the two grasper jaws was different for both in vitro experiments and FEA and the differences enlarge with higher deformation magnitude. This difference may be caused by the boundary conditions of the liver model: In the in vitro experiments, friction existed between the bottom portion of liver and the steel plate. Also the contact areas for both jaws may not always be consistent for each loading step due to the thickness of the jaws. In the FEA simulation, the top portion of the tissue model was constrained, which caused asymmetrical distribution of von Mises stress in the region under compression.

Eq 3.10 and Figure 3.10B can be used to determine the minimal required length of the tissue model for FEA simulation. Previous work has used a local region around the grasper-tissue

interaction area to compute simulated force feedback. However, it is not clear what should be the minimal size of such regions. If the model size is far more than required, the computation time will increase dramatically. By contrast, if the model size is smaller than required, we may get wrong simulation results.

Limitations

We make the assumption in this study that the liver tissue is elastic instead of viscoelastic, the grasping force was addressed to not change with time of grasping. In reality, the fluid content in biological tissues may be squeezed out of the local region gradually under compression, which could change the local deformation, even if the same force is applied.

For the purpose of simplification, dynamic forces were not considered in this study. That means, for any time during grasping, we assumed that the system was in static force equilibrium. To eliminate the edge effects when modeling higher strain, slippage was not be allowed in our simulation study.

In real RMIS, it is observed that only the regions projected by the laparoscopic light can be detected while other blocked regions cannot be observed or measured. That means that only partial surface deformation of tissue can be seen by the laparoscopic camera when the tissue is compressed by a grasper. One solution is to use multiple cameras shooting from various view angles; however, it is quite challenging to install stereo cameras inside human body due to the restriction of space. Future studies should address the methodology of obtaining the deformation descriptor through one single laparoscopic camera.

3.7 References for Chapter 3

[1] S De. The Grasper-Tissue Interface in Minimally Invasive Surgery: Stress and Acute Indicators of Injury. Ph.D. Thesis, University of Washington, 2008.

[2] AM Okamura. Haptic feedback in robot-assisted minimally invasive surgery. Current Opinion in Urology. 19:102-107; 2009.

[3] J Dargahi, et al. Modeling and testing of an endoscopic piezoelectric-based tactile sensor. Mechatronics. 17: 462-467, 2007.

[4] B Kubler, et al. Development of actuated and sensor integrated forceps for minimally invasive robotic surgery. The International Journal of Medical Robotics and Computer Assisted Surgery, 1(3):96-107, 2005.

[5] P Meseure and C Chaillou. Deformable body simulation with adaptative subdivision and cutting. Proceedings of WSCG, 361-370, 1997.

[6] K Tagawa, et al. Adaptive and Embedded Deformation Model: An Approach to Haptic Interaction with Complex Inhomogeneous Elastic Objects. IEEE World Haptics Conference, 169-174, 2013.

[7] U Kocak, et al. Dynamic Deformation Using Adaptable, Linked Asynchronous FEM Regions. Proceedings of the 25th Spring Conference on Computer Graphics, 197-204, 2009.

[8] BM Ahn, et al. Robotic palpation and mechanical property characterization for abnormal tissue localization. Medical & Biological Engineering & Computation 50(9):961-971, 2012.

[9] H Liu, et al. Inverse finite-element modeling for tissue parameter identification using a rolling indentation probe. Medical & Biological Engineering & Computation, 52(1):17-28, 2014.

[10] K Morooka, et al. Real-Time Nonlinear FEM with Neural Network for Simulating Soft Organ Model Deformation. Medical Image Computing and Computer-Assisted Intervention – MICCAI 2008 Lecture Notes in Computer Science, 5242: 742-749, 2008.

[11] X Chen, et al. Study on liver surgery navigation based on nonlinear finite element method. Journal of Japan Society of Computer Aided Surgery 5: 15-22, 2003.

[12] YC Fung. Biomechanics: mechanical properties of living tissue. Springer, Berlin Heidelberg, New York, 1981.

[13] FJ Carter, TG Frank, et al. Measurements and modeling of the compliance of human and porcine organs. Medical Image Analysis. 5(4), 231-236, 2001.

[14] S Giannarou, MV Scarzanella and GZ Yang. Probabilistic Tracking of Affine-Invariant Anisotropic Regions. IEEE Transactions on Pattern Analysis and Machine Intelligence, 99, 2012.

[15] C Chui, et al. Combined compression and elongation experiments and non-linear modeling of liver tissue for surgical simulation. Medical and Biological Engineering and Computing. 42(6):787–798, 2004.

[16] Z Gao, K Lister and JP Desai. Constitutive modeling of liver tissue: experiment and theory. Annals of Biomedical Engineering, 38(2):505, 2010.

[17] L Cheng, B Hannaford. Finite Element Analysis for Evaluating Liver Tissue Damage Due to Mechanical Compression. Journal of Biomechanics, Vol. 48, Issue 6, 948-955. 2015.

[18] P Mountney, D Stoyanov and GZ Yang. Three-Dimensional Tissue Deformation Recovery and Tracking: Introducing techniques based on laparoscopic or endoscopic images. IEEE Signal Processing Magazine, 27(4): 14-24, 2010.

[19] J Rosen, JD Brown, S De, M Sinanan, B Hannaford. Biomechanical properties of abdominal organs in vivo and postmortem under compression loads. Journal of Biomedical Engineering, 130(2): 021020, 2008.

[20] YB Fu, CK Chui. Modeling and Simulation of Porcine Liver Tissue Indentation using Finite Element Method and Uniaxial Stress-Strain Data. Journal of Biomechanics, 47(10): 2430-2435, 2014.

[21] RW Ogden. Large deformation isotropic elasticity: on the correlation of theory and experimental for compressible rubberlike solids. Proceedings of the Royal Society of London, Series A (Mathematical and Physical Sciences), 328(1575), 567-583, 1972.

[22] S De, J Rosen, A Dagan, B Hannaford, P Swanson, M Sinanan. Assessment of tissue damage due to mechanical stresses. International Journal of Robotic Research, 26:1159–1171, 2007.

[23] E Noohi, S Parastegari and M Žefran. Using Monocular Images to Estimate Interaction Forces During Minimally Invasive Surgery. 2013 IEEE/RSJ International Conference on Intelligent Robots and Systems (IROS), 4297-4302.

[24] PS Tsai and M Shah. Shape from shading using linear approximation. Image and Vision Computing, 1994.

[25] G Zeng, Y Matsushita, et al. Interactive Shape from Shading. IEEE Computer Society Conference on Computer Vision and Pattern Recognition, 1:343-350, 2005.

Chapter 4. Evaluation of Liver Tissue Damage and Grasp Stability Using Finite Element Analysis

4.1 Overview

Minimizing tissue damage and maintaining grasp stability are essential considerations in surgical grasper design. Most past and current research analyzing graspers used for tissue manipulation in minimally invasive surgery is based on in-vitro experiments. Most previous work assessed tissue injury and grasp security by visual inspection; only a few studies have quantified it. The goal of the present work is to develop a methodology with which to compute tissue damage magnitude and grasp quality that is appropriate for a wide range of grasper-tissue interaction. Using finite element analysis (FEA), four graspers with varying radii of curvature and four graspers with different tooth sizes were analyzed while squeezing and pulling liver tissue. All graspers were treated as surgical steel with linear elastic material properties. Nonlinear material properties of tissue used in the FEA as well as damage evaluation were derived from previously reported in-vivo experiments. Computed peak stress, integrated stress, and tissue damage, were compared. Applied displacement is vertical and then horizontal to the tissue surface to represent grasp and retraction. A close examination of the contact status of each node within the grasper-tissue interaction surface was carried out to investigate grasp stability.

The results indicate less tissue damage with increasing radius of curvature. A smooth wave pattern reduced tissue damage at the cost of inducing higher percentage of slipping area. This methodology may be useful for researchers to develop and test various designs of graspers. Also it could improve surgical simulator performance by reflecting more realistic tissue material properties and predicting tissue damage for the student.

** This is a modified version of the published manuscript: Lei et al. Evaluation of Liver Tissue Damage and Grasp Stability Using Finite Element Analysis. Computer Methods in Biomechanics and Biomedical Engineering, Nov 19, 1-10, 2014, available online.

4.2 Introduction

The grasper is a commonly-used instrument in either traditional or robotic-assisted minimally invasive surgery (MIS) [1, 2]. While some research has addressed haptic feedback during grasping [3-7], little attention has been given to the tissue damage or grasp stability properties of MIS instrument graspers. Some previous work showed, by measuring through a thin film pressure transducer, that rounding the edge of the grasper can reduce high stress generated at the tip [8]. When the grasper surface is serrated, increasing tooth size can induce more grip security but at the cost of increased tissue damage [9]; a smooth wave pattern grasper can cause significantly less tissue damage than a teeth pattern [9]; graspers with a larger contact area and a slight profile may prevent tissue damage and slip [10]. Most of these experiments were performed in vitro, which limits their applicability to clinical conditions. Also tissue injury and grasp security were assessed simply by visual inspection, such as whether a visible tissue tear or gross slip occurred. Some studies, however, suggested 1) subtle tissue abnormalities may exist and almost be unapparent to a naked-eye examination [11-12]; 2) Slip, especially incipient slip, will not occur evenly over the surface [13, 14]; both of which indicate the need for evaluating tissue damage and grasp stability on a finer scale.

One potential methodology for analyzing grasper-tissue interaction is Finite Element Analysis (FEA), which has served as an industry standard for prototype and design. FEA experiments can be carried out without animal care issues. A number of previous studies suggest that FEA could be an effective tool for understanding stress and strain distributions in tissue under loads [15, 16, 31].

The tissue damage specifically due to a mechanical load has been quantified. By using an isometric contraction model, Famaey et al. quantitatively studied the damage to smooth muscle cells of rat abdominal arteries after in-vivo clamping to well-defined loading levels [19, 20]. For porcine liver and small bowel, De et al. measured the acute indicators of tissue damage including cellular death and infiltration of inflammatory cells responding to stress magnitude applied in MIS [21]. De et al. also proposed a damage-stress relationship based on measuring hepatic necrosis as a function of stress from in-vivo experiments [22].

For object manipulation, a grasp can be treated as stable if there exists a non-slip region in the contact area given any arbitrary applied force [13, 23]. To detect the slip motion, two types of methods were employed by previous studies, which were not all specifically for MIS graspers: the first used tactile sensing/controlling systems along with various sensors to detect slipping states during manipulation [13; 25-26]; the second type focused on investigating the contact mechanics to model the slip-stick phenomenon [14, 27].

Our study used 2-D finite element analysis to develop a methodology to represent tissue damage magnitude and grasp quality that could be appropriate for varying grasper-tissue interaction. This study focused on liver tissue for two reasons. First we have extensive experimental data from De's earlier work [22]. Second, the liver is widely modeled as isotropic and homogeneous which simplifies parameter identification and FEM (see below). Nonlinear mechanical properties of liver tissue were applied at first to get the von Mises stress distribution within the tissue and then tissue damage was calculated based on De et al.'s necrosis-stress function computed from previous in-vivo experiments. Computed peak stress, integrated stress and tissue damage in the form of hepatic necrosis were compared step by step for an increasing applied displacement. A close examination of the contact status of each node within the grasper-tissue interaction surface was carried out to investigate grasp stability. By comparing the results with experimental counterparts, it can be concluded that the methodology may be useful for researchers to develop and test various designs of graspers.

4.3 Methods

4.3.1 *Material model for tissue and grasper*

Soft tissue is often inhomogeneous and anisotropic and its compounds vary throughout the whole structure. Carter et al. found solid organs, particularly the liver and spleen, could be treated as approximately isotropic and homogenous due to its uniform histology across species [17]. Also because of the high water content of the liver tissue, we can consider it to be incompressible [30]. Since the thickness of the grasper is much less than the tissue's, a plane strain assumption is applied in our application, i.e. there is no strain normal to the XY plane (Figure 4.3D). This

would allow for higher computational efficiency without losing essential information. The effects of these assumptions are further addressed in the discussion.

The modeling of continuum mechanics is the same with Section 2.3.1. We only list the equations below for reference.

$$\sigma = \beta(e^{\alpha\varepsilon^2} - 1) + \gamma\varepsilon \tag{Eq4.1}$$

$$W_O = \sum_{i=1}^{N} \frac{\mu_i}{\alpha_i}[\lambda_1^{\alpha_i} + \lambda_2^{\alpha_i} + \lambda_3^{\alpha_i} - 3 + \frac{1}{d_i}(J-1)^{2i}] \tag{Eq4.2}$$

$$W_O = \sum_{i=1}^{N} \frac{\mu_i}{\alpha_i}[\lambda_1^{\alpha_i} + \lambda_2^{\alpha_i} + \lambda_3^{\alpha_i} - 3] \tag{Eq4.3}$$

$$\sigma_c = \sum_{i=1}^{N} \mu_i[\lambda_1{}^{\alpha_i} - \lambda_1{}^{-\alpha_i/2}] \tag{Eq4.4}$$

Adopting the notation of Rosen et al. [24], with the compression load, $\sigma_c = -\sigma$ and $\lambda = 1 - \varepsilon$, We then numerically fit Rosen et al.'s phenomenological stress-strain curves to Eq 4.4. The parameters for the least-square fitting 1st-order Ogden model are: α_1=19.48 and μ_1=0.001687 with the coefficient of determination R^2=0.9993. The plot in Figure 4.1 compares the stress-stretch curves of the Ogden fit model with the linear models (Young's Modulus E=150kPa and E=300kPa) [22, 24]. It shows the stiffness of our Ogden fit nonlinear model falls in the range between linear models E=150kPa and E=300kPa in the region where 1>stretch>0.67.

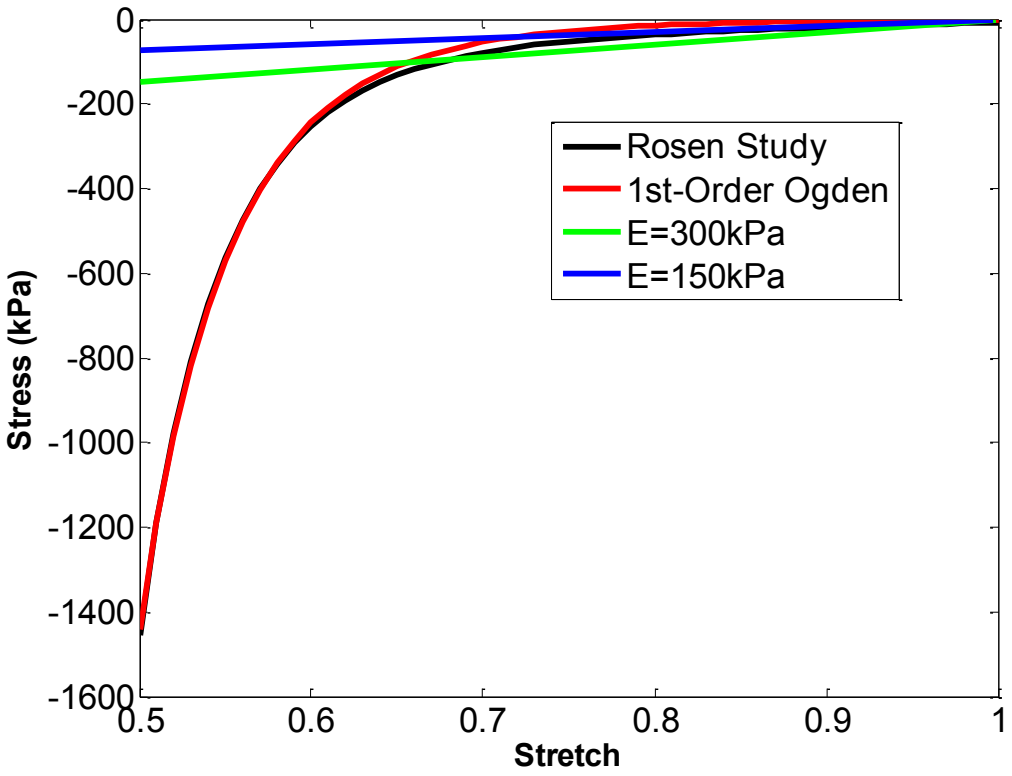

Figure 4.1 Stretch-stress curves for nonlinear and linear tissue models.

Surgical graspers are considered to be composed of an isotropic linear elastic material (stainless steel) with the Young's modulus E=190GPa and the Poisson's ratio ν=0.27 [21].

4.3.2 *Finite element model for tissue-grasper contact*

Four graspers with different radii of curvature and four graspers with different tooth patterns were analyzed in ANSYS Mechanical APDL 14.0 (Table 4.1). The dimension of the tissue is set to 8mm height×16mm width. Due to the symmetry of our problem, only half of the tissue (4mm height×16mm width) is considered in the analysis. The cross section of three different graspers are illustrated (Figure 4.2). The left surface of the tissue (Figure 4.3D) is completely constrained while the bottom surface can only have freedom along the x direction. The applied displacement of the grasper increases from 0 mm to 1mm in the negative y direction (Uy=0~-1mm) at first and then from 0 mm to 1mm along the x direction (Ux=0~1mm).

Table 4.1 Geometry parameters for each grasper we studied. Grasper width= 5mm, height=2mm.

Grasper Number	Pattern	R (mm)	D_p (mm)	α (degree)
1	Rectangular	0.05	N/A	N/A
2	Rectangular	0.25	N/A	N/A
3	Rectangular	0.5	N/A	N/A
4	Rectangular	0.75	N/A	N/A
5	Triangular	0.05	1	60
6	Triangular	0.05	0.5	60
7	Sin Wave	N/A	2	180
8	Sin Wave	N/A	1.1	180

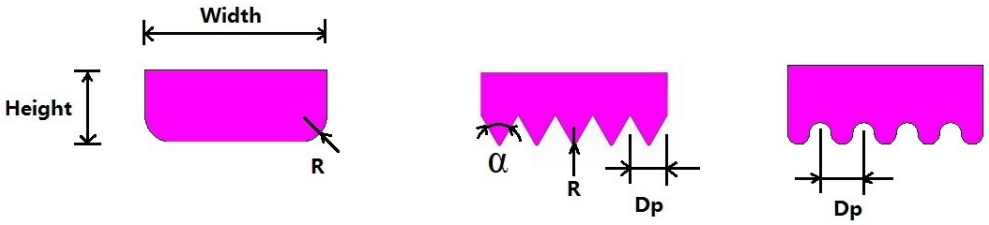

Figure 4.2 Geometries for different graspers we studied. R refers to radius of curvature and D_p refers to pitch size. Grasper width= 5mm, height=2mm, tooth angle α=60 degree.

The tissue is modeled with 8-noded axisymmetric, quadrilateral, solid elements. The meshing size for the tissue is set to be uniform to facilitate the tissue damage computation (Section 4.3.4). The grasper domain is meshed using the same element type but its size is gradually refined for the portions which will potentially be involved in the grasper-tissue interaction (Figure 4.3).

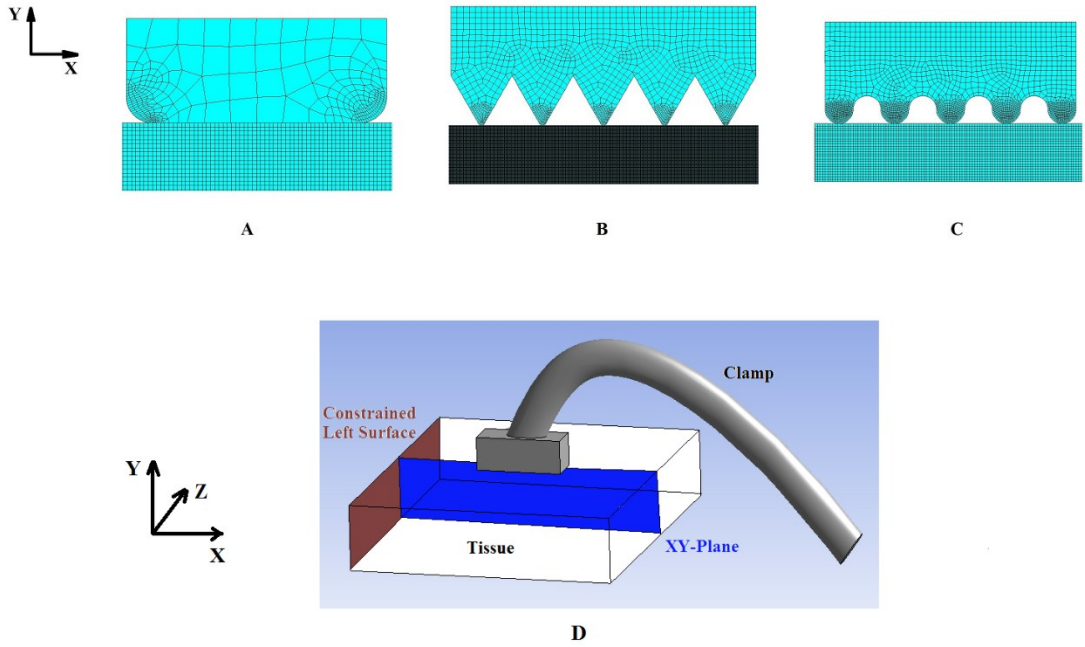

Figure 4.3 Finite element meshing of tissue and three grasper patterns. The grasper patterns are: A) rectangular radius of curvature=0.5 mm; B) 60 degree triangular pattern, pitch size=1mm; C) sine wave pattern, pitch size=1.1 mm. D) Illustration of left surface (brown area) and XY plane (blue area) in 3D model. Black lines sketch the tissue while grey solid sketches the clamp.

To choose a suitable meshing size for the tissue which will not give results highly sensitive to meshing size, five different meshing sizes for a single tooth and a rectangle block with curvature were tested. We found that when the ratio of curvature radius to meshing size is larger than 6 for the rectangular grasper (ratio>4 for tooth grasper), integrated force and damage were not sensitive to meshing size (sensitivity<0.1). Therefore, these two geometrical ratios were needed to set the meshing size of the tissue in our study.

4.3.3 *Finite Element Contact Analysis*

The interaction between tissue and grasper is modeled by finite element contact analysis, in which the Augmented Lagrangian Method is used for our study. Appropriate values of normal penalty stiffness (FKN) and penetration tolerance (FTOLN) are assigned to help the solver converge and avoid penetration.

Coulomb's law is employed to check the slip/stick status at each contact node:

$f_{fr} = \mu f_n$ if $f_s \geq \mu f_n$, which means slip;

$f_{fr} = f_s$ if $f_s < \mu f_n$, which means stick;

where f_{fr} is the friction force, f_s is the shear force, f_n is the normal force and μ is the coefficient of friction of the contact.

Assuming N_C is the number of nodes at the contact interface and N_{Slip} is the number of nodes in slip status, the equilibrium percentage of slipping area P_{Slip} can be calculated by $P_{Slip} = N_{Slip} / N_C$. Since both N_C and N_{Slip} may change with varying applied displacement conditions, P_{Slip} at various displacement intensities can be a suitable marker to reflect the tendency of slipping.

4.3.4 *Calculation of tissue damage*

The modeling of continuum mechanics is the same with Section 2.3.4. We only list the equations below for reference.

$$\%Necrosis = a + \frac{B * {\sigma_v}^C}{D^C + {\sigma_v}^C} + Duration * E \quad \text{(Eq4.5)}$$

$$\%Necrosis = \frac{B * {\sigma_v}^C}{D^C + {\sigma_v}^C} \quad \text{(Eq4.6)}$$

$$Damage_T = \sum_i^N (\%Necrosis)_i * \frac{A}{N} \quad \text{(Eq4.7)}$$

$$Stress_T = \sum_i^N (\sigma_{v,i} * \frac{A}{N}) \quad \text{(Eq4.8)}$$

4.4 Results

Four examples of the calculated von Mises stress distribution with various grasper shapes and the combined compression/retraction displacements are given in Figure 4.4A-D. For two rectangular graspers (Figure 4.4A and 4.4B), the stress on the contact surface peaked at the two corners and reduced in the middle. Though the contact area was not continuous for two toothed graspers (Figure 4.4C and 4.4D), similar trends were seen in that the local peak stress around the tooth tip in the center was significantly lower than those located at the two corners. For the grasper with

the 1mm, 60 degree tooth pattern, the peak von Mises stress was 134.0 kPa in the middle compared to 1079.5 kPa at the left corner and 302.9 kPa at the right corner.

A) Radius of curvature=0.05mm;

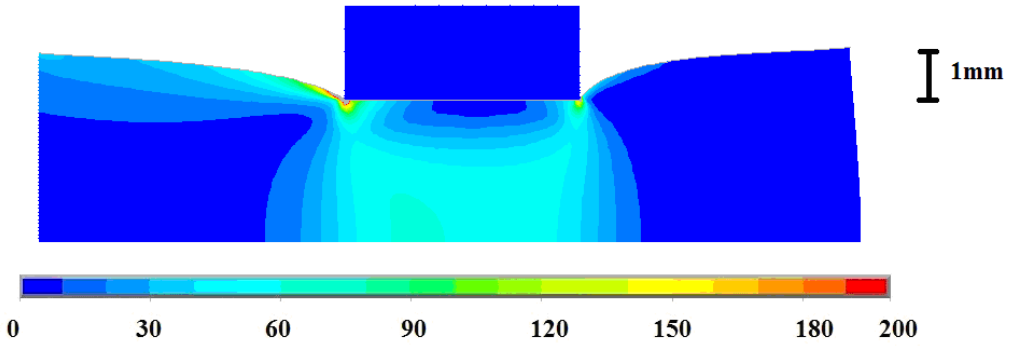

B) Radius of curvature=0.75mm;

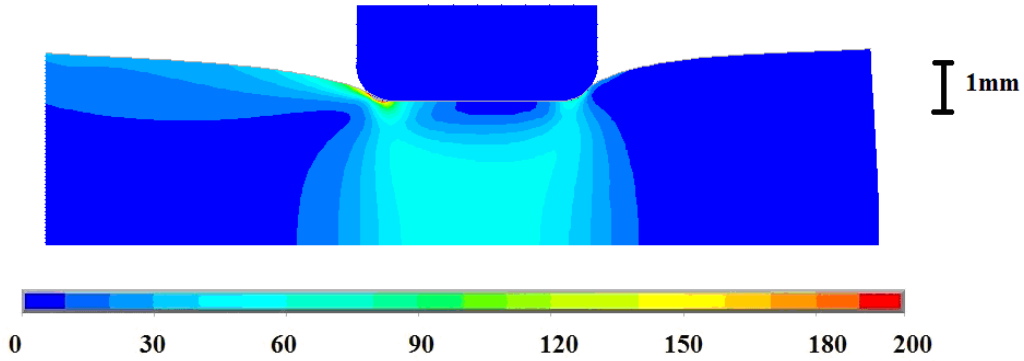

C) 60 degree triangle pattern, pitch size=1mm;

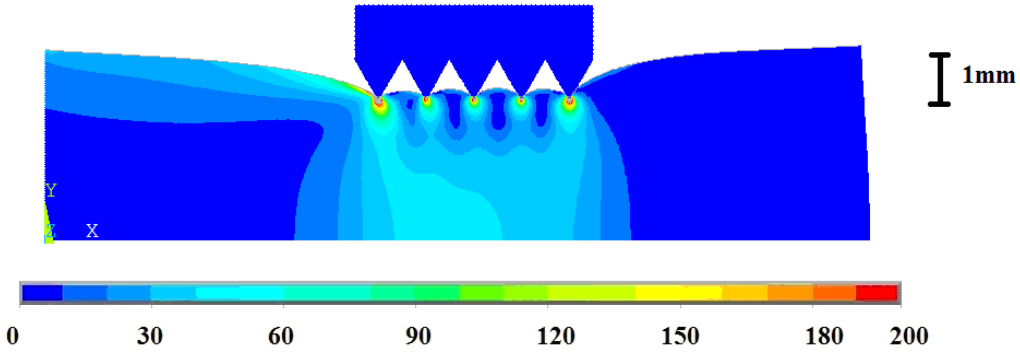

D) Sine wave pattern, pitch size=2 mm;

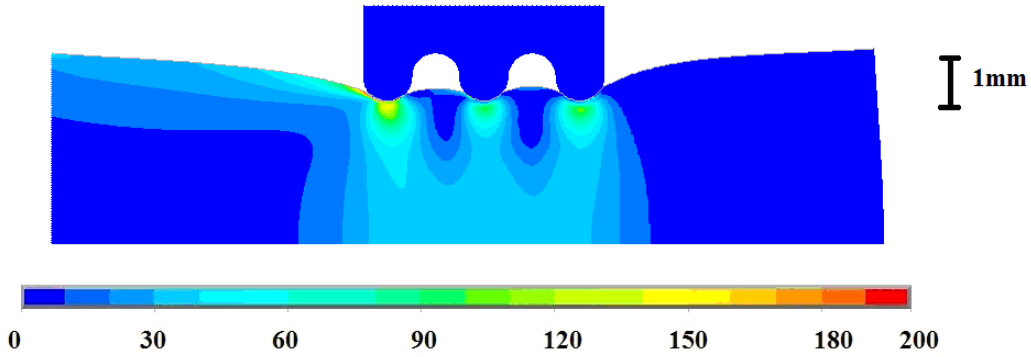

Figure 4.4 von Mises stress plot of FEA using nonlinear material properties. Scale is in kPa. The applied displacements are Uy=-1mm (squeezing downward) and then Ux=1mm (pulling to right side). Areas with stress more than 200 kPa are shown in silver grey.

After mapping stress to percentage necrosis of each element area using Eq4, we got the computed necrosis distributions. Two plot examples are shown in Figure 4.5A-B, which indicated that the stresses around the tooth tips at the grasper-tissue contact surface contributed most to the tissue damage. Due to the nonlinear property of the necrosis-stress curve, the contours of the necrosis distribution were different from that of the stress distribution in several regions.

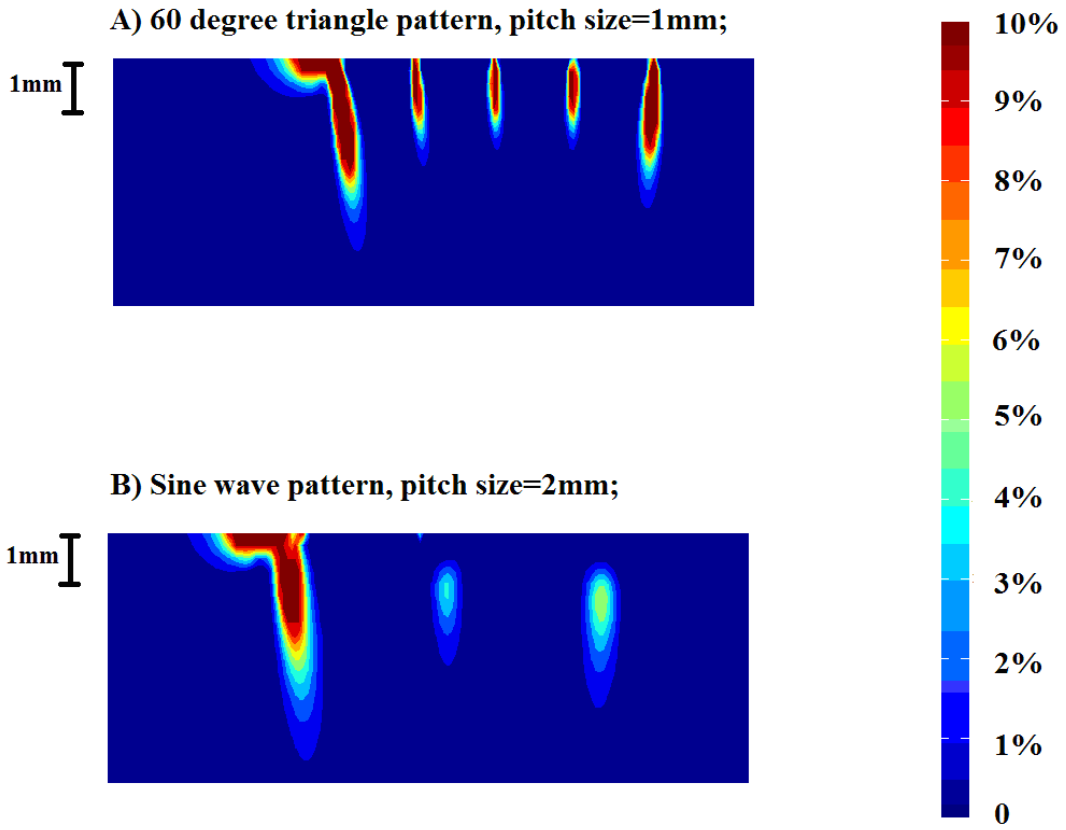

Figure 4.5 Zoomed contour of computed necrosis distribution. Deformation is not shown. Scale is in percent. Areas with percentage of necrosis more than 10% are shown in wine red. The applied displacements are Uy=-1mm (squeezing downward) and then Ux=1mm (pulling to right side);

The peak von Mises stress was calculated for the rectangular graspers with different corner radii (Figure 4.6A). The results showed clear reduction in the corresponding peak von Mises stress with increasing radius of curvature.

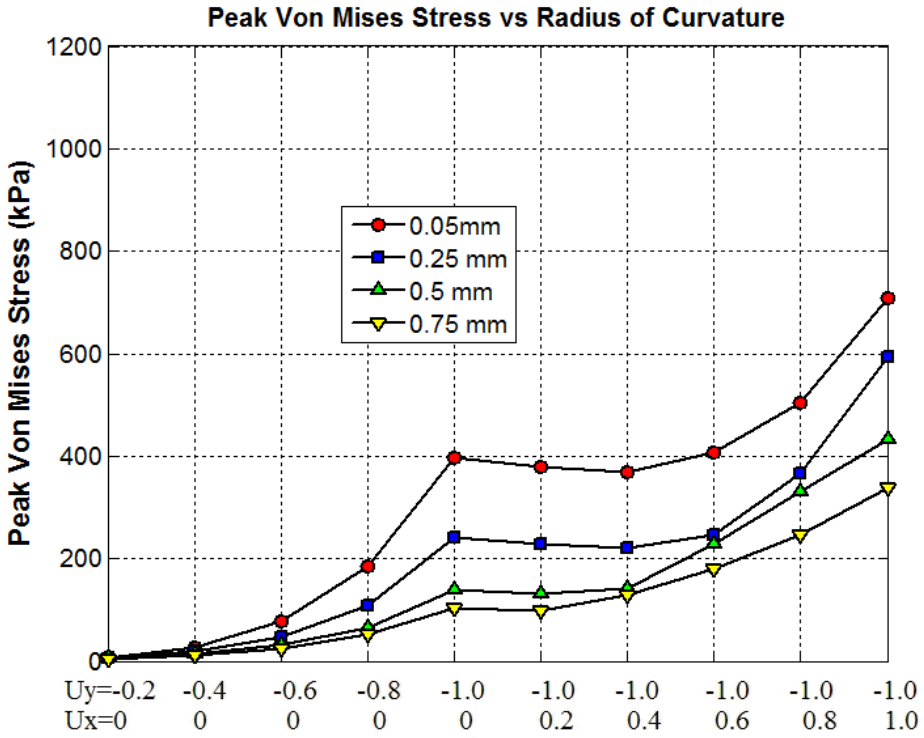

B) Integrated von Mises stress (N) with different radius of curvature.

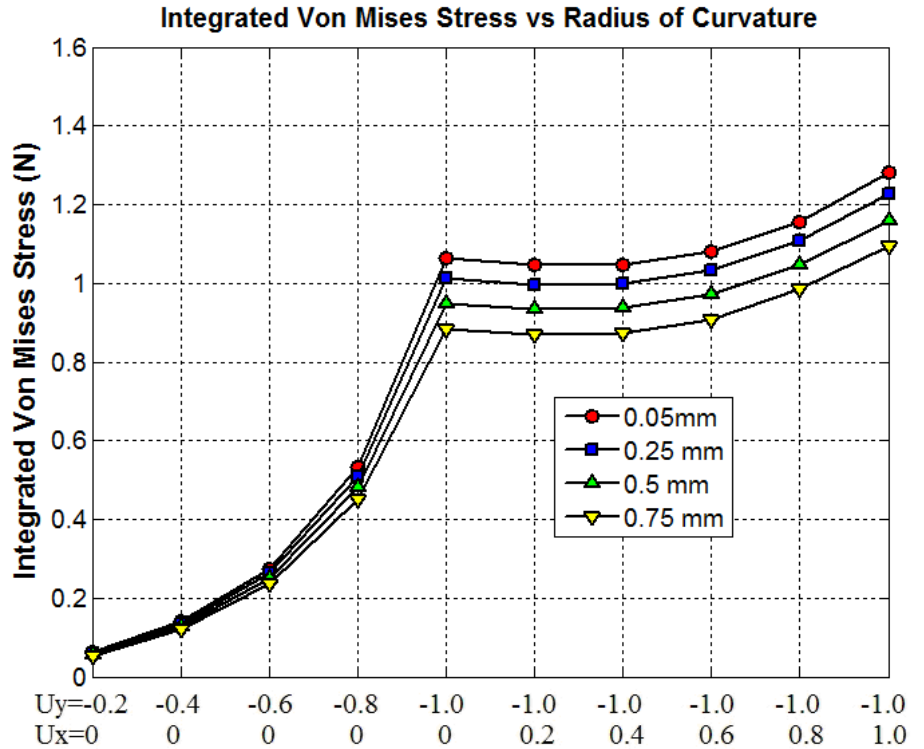

C) Equivalent tissue damage area with radius of curvature.

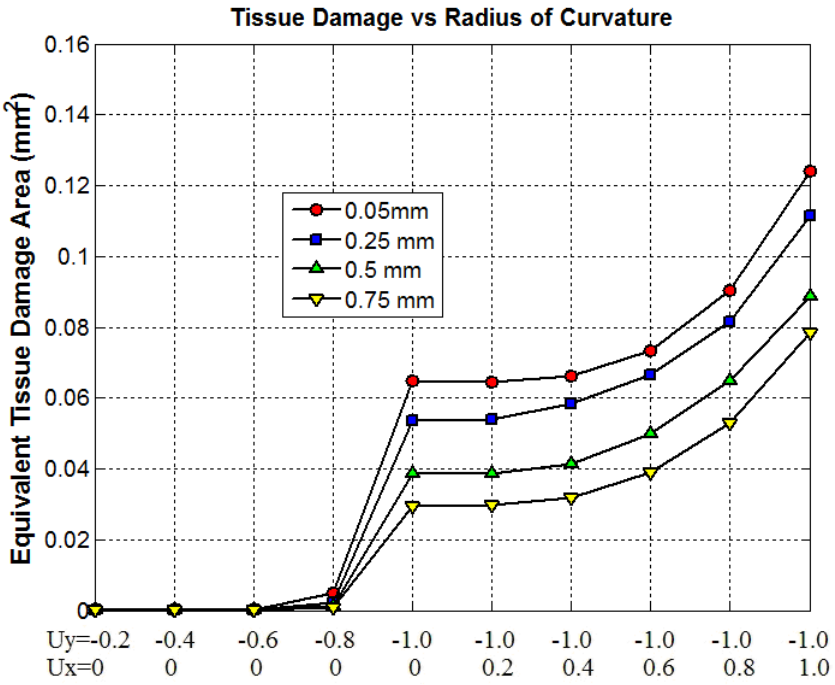

Figure 4.6 A) Peak von Mises stress(kPa) for rectangular graspers with different radius of curvature. The applied displacements are Uy and Ux (mm).

Through adding up each element's von Mises stress multiplied by its area, the integrated von Mises stress can be calculated. For each displacement shown in Figure 4.6B, the integrated von Mises stresses decreased with increasing radius of curvature, though the difference was less than 10%.

Tissue damage in the form of necrosis was calculated using Eq4.4 (Figure 4.6C). The results indicated less tissue damage with increasing radius of curvature; also for each displacement step, the difference between radius=0.05mm and radius=0.25mm was similar with either that between radius=0.25mm and radius=0.5mm or that between radius=0.5mm and radius=0.75mm.

Four graspers with the four different tooth patterns were applied to the same nonlinear tissue model at the applied displacement of Uy=-1mm and Ux=0~1mm. The wave tooth pattern reduced the peak von Mises stress by about 50% compared to the triangular tooth pattern (Figure 4.7A). Integrated von Mises stresses for each displacement step were also computed (Figure 4.7B), but by this measure, grasper patterns with smaller tooth size generated slightly more

overall stress than those with bigger teeth. Computing the equivalent tissue damage area (Figure 4.7C) showed significantly lower cellular death with the wave tooth pattern than with the triangular tooth pattern. Also the tooth size clearly impacted the tissue damage results: for the wave tooth pattern, a smaller tooth size increased tissue damage; for the triangular tooth pattern, however, the trend was opposite.

A) Peak von Mises stress (kPa) with different tooth patterns. The applied displacements are Uy and Ux (mm).

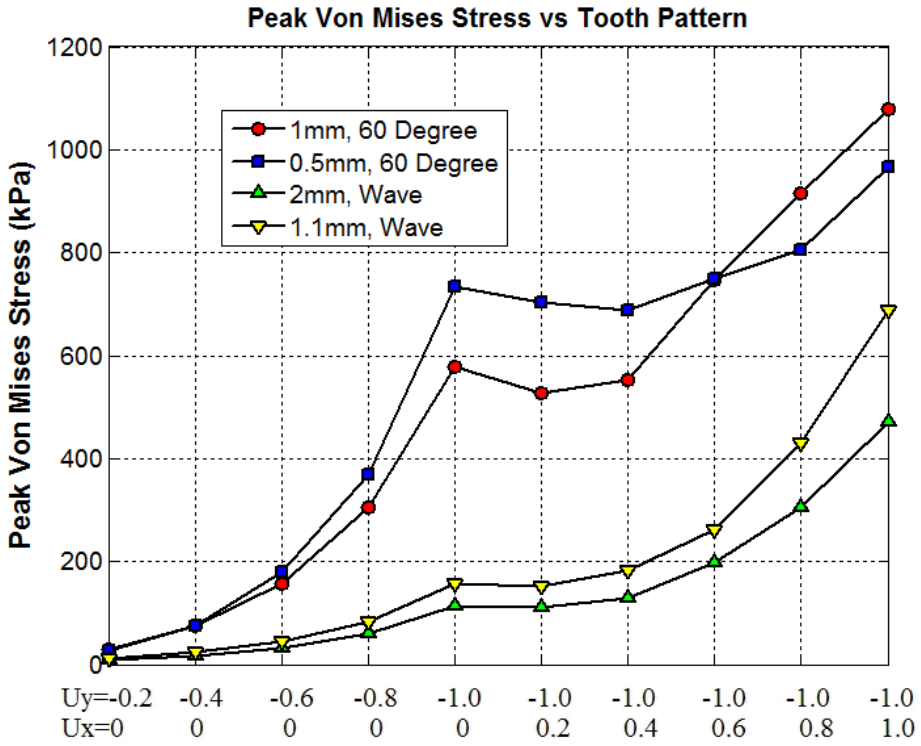

B) Integrated von Mises stress (N) with different tooth patterns.

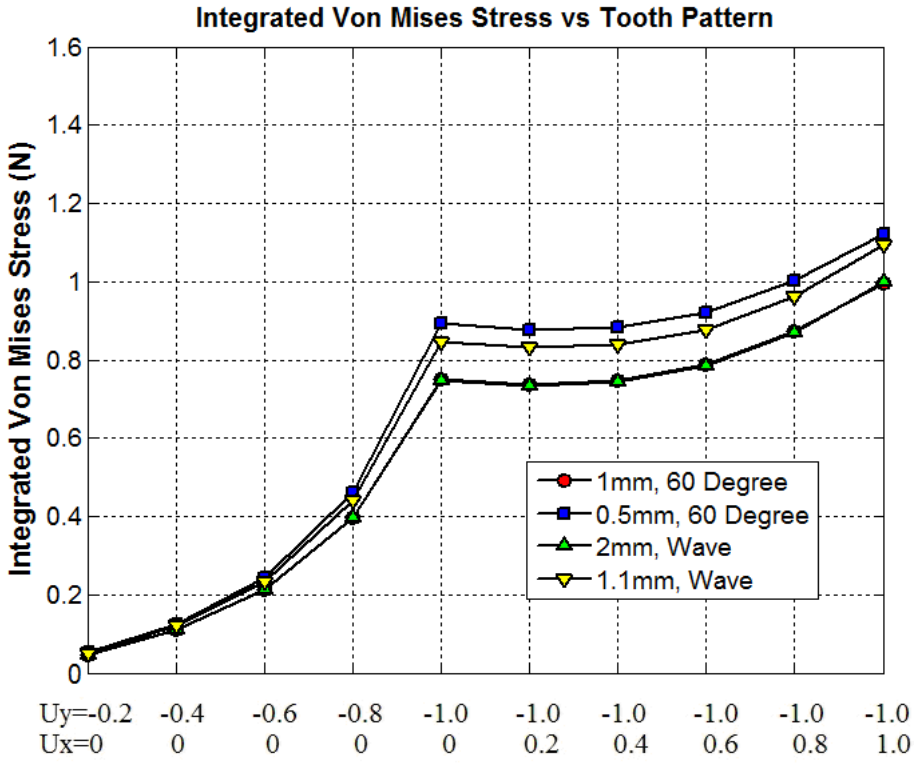

C) Equivalent tissue damage area with different tooth patterns.

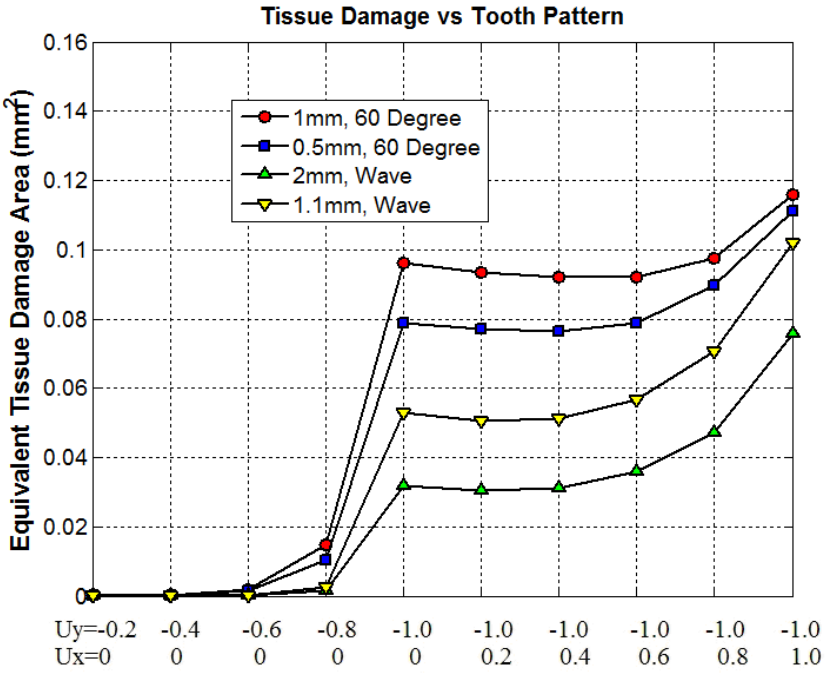

Figure 4.7

The computed percentage of slipping contact area due to pulling tissue showed no slippage for triangular tooth patterns with coefficients of 0.5 or 1.0. For wave tooth patterns, the percentage of slipping area (Figure 4.8) enlarged with increasing pulling displacement. Also it was obviously impacted by the tooth size: smaller wave teeth had more slippage than larger teeth.

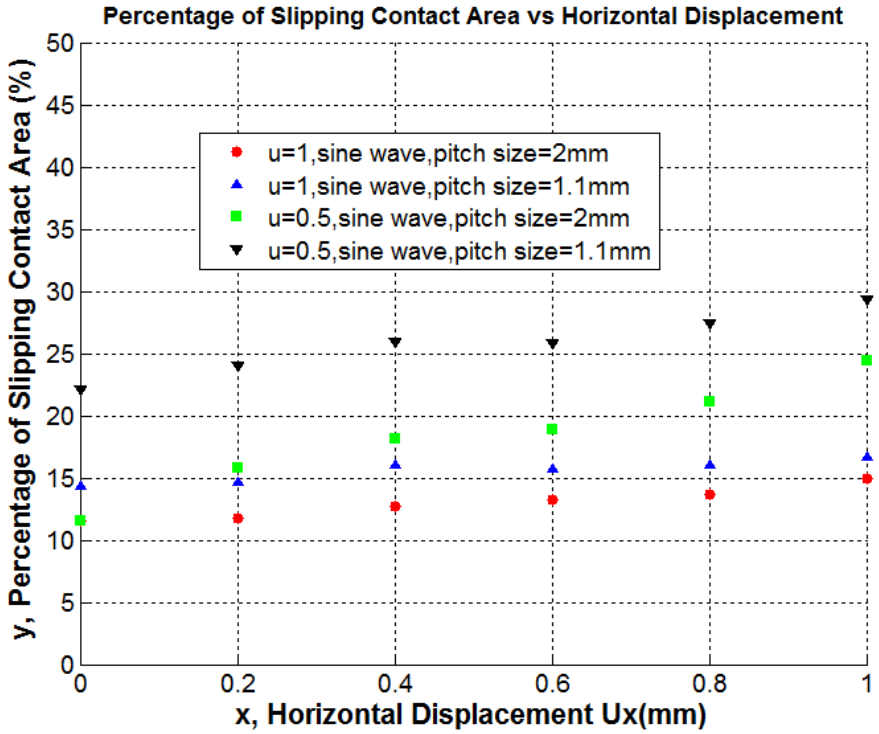

Figure 4.8 Percentage of slipping contact area with friction coefficient μ and pitch number. Scale is in percent. Slipping elements were only observed with the smooth wave tooth pattern. The applied displacements are holding Uy=-1mm (squeezing downward) and increasing Ux from 0 to 1mm (pulling to right side);

4.5 Discussion and Conclusions

We used a two dimensional FE model of the liver with nonlinear mechanical properties to investigate the stability and safety of a variety of tool geometries. To study an application such as surgical retraction, we applied both compression and horizontal applied displacements. It was observed that the high stress concentration may result in a higher risk of tissue injury at the edge of graspers [8], which indicates a need to identify the magnitude of peak stress in tissue. In order to investigate the relationship between total tissue damage and total stress, the integrated von

Mises stress was recorded. The equilibrium percentage of slipping area was calculated with increasing horizontal applied displacement to predict the tendency of slipping for various graspers.

Our results showed clear reduction in the peak von Mises stress with increasing radius of curvature (Table 4.2). De et al.'s simulation with linear material properties found that a 0.5mm radius of curvature can reduce peak stress by 65% compared to zero radius of curvature [22]. Shakeshaft et al. reported a similar reduction rate of more than 50% based on in-vitro experimental results [8]. Our simulation, as far as we know, is the first to use nonlinear tissue properties and indicates reduction of peak stresses by 25%~74%, varying with applied displacements.

Table 4.2 Peak von Mises stresses (kPa) with different grasper patterns. The applied displacement is [Uy,Ux] (mm).

Grasper Number	[-0.2,0]	[-0.4,0]	[-0.6,0]	[-0.8,0]	[-1,0]	[-1,0.2]	[-1,0.4]	[-1,0.6]	[-1,0.8]	[-1,1]
1	7.32	27.72	76.62	183.86	397.35	379.18	369.26	407.53	504.47	708.66
2	6.17	18.48	48.23	108.97	240.69	229.45	219.87	245.29	367.19	593.89
3	5.47	13.40	31.80	65.84	138.12	130.93	140.47	228.47	330.57	432.84
4	4.59	10.64	25.36	51.92	102.39	97.49	129.73	180.17	245.73	339.22
5	29.52	75.62	157.43	306.31	578.00	526.08	552.66	746.96	915.69	1079.50
6	26.14	75.64	179.77	369.97	733.10	702.85	688.04	749.84	806.04	967.33
7	8.10	17.76	32.66	59.89	113.18	110.23	127.66	198.40	304.84	470.48
8	10.59	23.91	45.21	82.87	156.61	152.51	181.46	261.31	430.25	688.66

De et al. showed tissue damage decreased with increasing radius of curvature but the difference was small [22]; in our study, however, the damage increases were significant for all four different curvature radii (Figure 4.6C). The reason may be that De et al. used a linear model vs. our nonlinear one.

Marucci et al. concluded in their in-vitro experimental work that a wave tooth pattern resulted in significantly less tissue trauma than a triangle tooth pattern. They found tissue slippage occurred

with both 2-mm and 3-mm wave tooth patterns but not with the triangle tooth pattern [9]. Although Marucci et al. used compression force and pulling displacement, we applied displacement for both compression and pulling directions; the similar results bolster the idea that FEA could be an effective tool for developing graspers with maximal grasp security and minimal tissue damage. Additionally, FEA can be carried out without the cost and difficulties of testing in-vivo or in-vitro.

Although our computations predict large differences in tissue damage between various grasper shapes, the computed absolute amount of cellular death was small in all our test cases. For example, the peak equivalent tissue damage area value of 0.12 square millimeters (Figure 4.7C) represents only 0.19% of cells totally damaged in the 4mmx16mm area. The peak stresses at the grasper-tissue contact surface contributed most to the tissue damage but only in small localized regions. The small absolute value of damage might be clinically inconsequential in a single grasp. However, considering that many grasps may be applied during a surgery procedure, even a tiny reduction in tissue injury during a single grasp could generate a big overall difference.

Limitations and Future Directions

The maximum applied displacements in this study were Uy=-1mm (vertical squeezing) and then Ux=1mm (pulling to right side), which were equivalently 25 percent vertical and 6.25 percent horizontal applied strain. The strains imposed on tissue are less than those in real grasping, where novice surgeons sometimes employ a "death grip" to avoid slipping [13]. Also to relate the applied displacement to the macroscopic grasping pressure (force to contact area), we carried out a contact pressure (vertical direction) versus displacement analysis for the four graspers with varying radii of curvature (Table 4.3). During the process of squeezing, the curves of pressure-displacement match well with the 1st order Ogden stress-strain curve in Figure 4.1. However, we did not perform such analysis for the graspers with different tooth sizes, which might be quite challenging due to the complicated contact surface.

Table 4.3. Vertical contact pressure (kPa) corresponding to the applied displacement [Uy,Ux] (mm) with different grasper patterns.

Grasper Number	[-0.2,0]	[-0.4,0]	[-0.6,0]	[-0.8,0]	[-1,0]	[-1,0.2]	[-1,0.4]	[-1,0.6]	[-1,0.8]	[-1,1]
1	3.03	5.77	11.34	24.71	52.27	47.93	47.43	47.00	46.52	46.01
2	2.58	6.31	12.28	24.29	51.51	47.15	46.82	46.38	48.80	44.87
3	2.57	5.71	11.39	22.68	47.76	46.79	46.34	45.93	45.49	43.07
4	2.82	5.96	11.73	22.30	50.07	46.14	45.58	45.31	46.01	42.65

Higher applied vertical strain of up to 0.32, i.e. Uy=-1.3mm, could be applied to our tissue model for different tooth patterns without calculation errors; but if a horizontal displacement was applied afterward, the calculation was not able to converge. Some unsuccessful attempts to overcome this computational limitation included trying various values of model parameters like normal penalty stiffness (FKN) and penetration tolerance (FTOLN), refining the meshing at the contact interface, decreasing the sub-step of displacement and applying other algorithms in ANSYS.

Slippage was allowed in this study, which may result in edge effects in higher strain models [22]. However, since the displacements were applied, and the results were compared step by step, the potential inaccuracy due to this edge effect could be eliminated. Also this study did not test graspers with denser teeth. More teeth need finer meshing of tissue in FEA, which could consume dramatically larger amounts of computing time.

The tissue material in this study was assumed to be nonlinear, isotropic and homogeneous. In reality, biological tissues are fundamentally complex, and may be composed of various substructures with different strain-stress characteristics. Another assumption was that the tissue's mechanical properties would not change after being damaged. Using a FEM of the liver microstructure and inhomogeneity, De et al. were not able to determine a pattern of damage which matched experimental results [21]. Once tissue cells are injured, they may physically break down or release a number of chemicals which initiate inflammation and change the local response to external loads.

In our study, a two-dimensional (2D) plane strain FE model was applied to represent the interaction between the tissue and grasper. It is known that all practical problems are three-dimensional (3D). However, the 2D plane strain model was appropriate as we were simulating a very thin compression site. Also a test three-dimensional FE model [22] showed that there was very little strain perpendicular to the center plane, which was consistent with our plane strain assumption. Our results are based on a 2D plane-strain FE model which has successfully predicted tissue damage distributions [22]. The limitations of this model include assumptions of isotropy and geometrical boundary conditions. Future work will address the effects of these modeling aspects on prediction of tissue damage.

Tissue damage may be caused by various mechanisms. The present study only simulated the tissue damage as a function of stress as studied by De et al. [22]. More recently, damage due to strain has received some attention [28, 29]. Although stress and strain are related by the constitutive relation, they can differ because of various definitions of strain and 2D/3D geometry. Future studies will address which factor has a stronger correlation with measured tissue damage.

Different soft tissues may have different damage criteria. Our soft tissue damage model is particularly based on in vivo liver experiments reported by Rosen et al. [24] and De et al. [22]. One limitation of the present study is that our numerical simulations of the liver may not be applicable to some other soft tissues. Future work will address the comparison of FEM simulation between various soft tissues when more in vivo experiment reports are available.

Future studies will also focus on identifying optimal grasper designs for multiple tissues using this methodology. With additional in-vivo validation studies, we hope to develop a more accurate FE model which can reduce calculation time and present the dynamic interaction between grasper and tissue in real-time.

4.6 References for Chapter 4

[1] Market engineering research for the U.S. market for general surgery laparoscopy access and closure instruments. Medical and Healthcare Marketplace Guide, 1999. Publisher: Frost & Sullivan London 071 730 3438. Dialog File Number 767 Accession Number 523034. [Cited 2001 Oct 18]. Available from: URL: http://www.dialogselect.com/business/cgi/present

[2] NJ Soper, LM Brunt, K Kerbl. Laparoscopic general surgery. New England Journal of Medicine. 10;330(6):409–419;1994.

[3] T Hu, G Tholey, JP Desai, AE Castellanos. Evaluation of a Laparoscopic Grasper with Force Feedback. Surgical Endoscopy, 18(5): 863-867, 2004.

[4] M MacFarlane, J Rosen, B Hannaford, C Pellegrini, M Sinanan. Force feedback grasper helps restore the sense of touch in minimally invasive surgery. Journal of Gastrointestinal Surgery, 3(3):278–285, 1999.

[5] J Rosen, B Hannaford, M MacFarlane, M Sinanan. Force Controlled and Teleoperated Endoscopic Grasper for Minimally Invasive Surgery - Experimental Performance Evaluation. IEEE Transactions on Biomedical Engineering, 46:1212-1221, Oct, 1999.

[6] G. Tholey, JP Desai, AE Castellanos. Force feedback plays asignificant role in minimally invasive surgery: results and analysis. Annals of Surgery. 241(1):102–109, 2005.

[7] K Vakili, MS Flander, TR Sepp, MCorral, JD Diaz, A Slocum, GSL Teo. Design and Testing of a Pressure Sensing Laparoscopic Grasper. Proceedings of the 2011 Design of Medical Devices Conference DMD2011. April 12-14, 2011, Minneapolis, MN, USA

[8] AJ Shakeshaft, JA Cartmill, WR Walsh, CJ Martin. A curved edge moderates high pressure generated by a laparoscopic grasper. Surgical Endoscopy. 15:1232–1234, 2001.

[9] DD Marucci, J A Cartmill, WR Walsh, C. J. Martin. Patterns of failure at the instrument tissue interface. Journal of Surgical Research. 93(1):16-20, 2000.

[10] EA Heijnsdijk, VH de, J Dankelman, DJ Gouma. Slip and damage properties of jaws of laparoscopic graspers. Surgical Endoscopy, 18: 974-979, 2004.

[11] JC Kalff, WH Schraut, RL Simmons, AJ Bauer. Surgical manipulation of the gut elicits an intestinal muscularis inflammatory response resulting in postsurgical ileus. Annals of Surgery, 228(5):652-663, 1998.

[12] R Anup, KA Balasubramanian. Surgical stress and the gastrointestinal tract. Journal of Surgical Research. 92(2):291-300, 2000.

[13] J Stoll, P Dupont. Force Control for Grasping Soft Tissue. Proceedings of the 2006 IEEE International Conference on Robotics and Automation, May 2006, Orlando, FL, USA.

[14] VA Ho, S Hirai: Understanding Slip Perception of Soft Fingertips by Modeling and Simulating Stick-Slip Phenomenon. Robotics: Science and Systems, 2011.

[15] N Xydas, M Bhagavat, I Kao. Study of soft-finger contact mechanics using finite elements analysis and experiments. Proceedings of IEEE International Conference on Robotics and Automation, 2179–2184, 2000.

[16] J Tian, YB Jia. Modeling deformable shell-like objects grasped by a robot hand. Proceedings of the IEEE International Conference on Robotics and Automation, 1297-1302, 2009.

[17] FJ Carter, TG Frank, et al. Measurements and modeling of the compliance of human and porcine organs. Medical Image Analysis. 5(4), 231-236, 2001.

[18] RW Ogden. Large deformation isotropic elasticity: on the correlation of theory and experimental for compressible rubberlike solids. Proceedings of the Royal Society of London, Series A (Mathematical and Physical Sciences), 328(1575), 567-583, 1972.

[19] N Famaey, E Verbeken, S Vinckier, B Willaert, P Herijgers, J Vander Sloten. In vivo soft tissue damage assessment for applications in surgery. Medical Engineering and Physics, 32:437–443, 2010.

[20] N Famaey, J Vander Sloten, E Kuhl. A three-constituent damage model for arterial clamping in computer-assisted surgery. Biomechanics and Modeling in Mechanobiology, DOI: 10.1007/s10237-012-0386-7, 2012.

[21] S De, J Rosen, A Dagan, B Hannaford, P Swanson, M Sinanan. Assessment of tissue damage due to mechanical stresses. International Journal of Robotic Research, 26:1159–1171, 2007.

[22] S De. The Grasper-Tissue Interface in Minimally Invasive Surgery: Stress and Acute Indicators of Injury. Ph.D. Thesis, University of Washington, 2008.

[23] RS Fearing. Simplified grasping and manipulation with dextrous robot hands. IEEE Journal of Robotics and Automation, 2(4):188–195, 1986.

[24] J Rosen, JD Brown, S De, M Sinanan, B Hannaford. Biomechanical properties of abdominal organs in vivo and postmortem under compression loads. Journal of Biomedical Engineering, 130(2): 021020, 2008.

[25] D Goeger, N Ecker, H Woen. Tactile sensor and algorithm to detect slip in robot grasping processes. Proceedings of the IEEE International Conference on Robotics and Biomimetics, 1480-1485, 2009.

[26] S Shirafuji, K Hosoda. Detection and prevention of slip using sensors with different properties embedded in elastic artificial skin on the basis of previous experience. Robotics and Autonomous Systems (2012): doi:10.1016/j.robot.2012.07.016.

[27] T Maeno, S Hiromitsu, T Kawai. Control of grasping force by detecting stick/slip distribution at the curved surface of an elastic finger. Proceedings of the IEEE International Conference on Robotics and Automation, 3895-3900, 2000.

[28] RGM Breuls, CVC Bouten, et al. Compression induced cell damage in engineered muscle tissue: an in vitro model to study pressure ulcer aetiology. Annals of Biomedical Engineering, 31, 1357-1364, 2003.

[29] KK Ceelen, A Stekelenburg, et al. Compression-induced damage and internal tissue strains are related. Journal of Biomechanics, 41(16), 3399-404, 2008.

[30] Z Gao, K Lister and JP Desai. Constitutive Modeling of Liver Tissue: Experiment and Theory. Annals of Biomedical Engineering, 38(2):505, 2010.

[31] N Famaey, G Sommer, J Vander Sloten, et al. Arterial clamping: Finite Element Simulation and In Vivo Validation. Journal of the Mechanical Behavior of Biomedical Materials, 12, 107-118, 2012.

Chapter 5. Conclusion and Contribution

5.1 Conclusion

In this work, we studied the reality-based tissue model that can be applied in surgical simulator and force feedback console for robotic-assistant minimally invasive surgery. The research has three parts. In the first part, we developed a continuum mechanics model for von Mises stress and tissue damage under large deformation. It is found that the 3D thin membrane model generated very close results to full 3D model but reduced the computation time dramatically. However, it is not yet verified by in vivo experiments. In the second part, a custom designed force sensor was used to measure the grasping force on butch-shop materials while the surface deformation was recorded by one pair of stereo cameras. The two proposed descriptors of deformation, length and depth, were quantitatively related to the applied force and the relationship for both in vitro experiment and FEA results was the same. In the last part, we studied the impact of various grasper jaw patterns on the tissue damage and grasping quality by FEA. Our results indicated that larger radius of curvature on the tips of grasper teeth can reduce the tissue damage. A smooth wave teeth pattern is more likely to cause slippage but it can induce less tissue damage than a triangular tooth pattern.

5.2 Contribution

The key contributions from this work include: 1) a nonlinear finite element (FE) model suitable for tissue-grasper interaction; 2) a quantified relation between soft tissue deformation measured by a single camera and applied external forces; 3) a comparison of tissue damage produced by grasper patterns in RMIS. Each contribution is detailed as below:

Contributions of Chapter 2.

Built a nonlinear FEA model for simulating soft tissue consisting of

-A nonlinear material model based on Ogden strain energy, which is able to describe large deformation of soft tissue;

-A base model for the modeling and simulation of hepatic necrosis under in vivo conditions.

-A procedure which can reduce the computation cost of nonlinear FEM simulation;

Contributions of Chapter 3.

Investigated the correlation between characteristics of tissue surface deformation and applied force in FEA simulation and in vitro experiments consisting of

-A method for simulating the force through the deformation of organ models;

-A novel approach for detecting surface deformation of soft tissue;

-A method linking deformation with applied force under in vitro condition;

Contributions of Chapter 4.

Converted the information gleaned from previous objectives into actionable design insights for grasper shape in the form of tissue damage and grasp quality, specially

-A basic model which can be used to simulate tissue damage under various loading conditions;

-A methodology with which a researcher could develop and test various design of graspers.

Appendix1. Supplemental material for Chapter 3

A1.1 Background

The objective of this study is to investigate the quantitative relationship between tissue deformation and applied force. Previous studies on deformation and force in RMIS are mainly either for surgery simulator or for identifying tissue properties for a surgery simulator, the tissue property would be known with pre-given parameters. After applying certain mechanical loads like force or displacement, simulated tissue deformation would be presented in a virtual environment. Two popular approaches have been adopted for surgery simulation. One utilizes a mass-spring model. It is easy to use and fast in computation [1]. The other is the FEA-based simulation. Based on continuum mechanics, FEA is the most fundamental and widely used approach to compute both physically and visually realistic soft tissue deformations [2, 3]. The FEA-based simulation, however, is time-consuming because a large number of equations need to be solved. This drawback limits its application in real-time haptic force feedback which requires an update rate on the order of 1 kHz [2]. Some researchers proposed that the applied external force can be predicted via use of a neural network from the superposition of basic volumetric deformation modes computed off-line [4, 5]. Though such methods can achieve an acceptable accuracy for surgery simulation, they may not be suitable for estimating force feedback since they require the whole volumetric shape of organs, which are difficult to obtain during RMIS.

In prior tissue identification studies, soft tissue experiments were performed to measure surface deformation and force responses of soft tissues resulting from indentation loading depending on various indentation depths. Then inverse finite element modeling (IFEM)-based methods were used for tissue parameter identification using either a poking [6] or a rolling indentation probe [7] for surgical palpation.

We are interested in whether is it is possible to predict the applied external force given known tissue properties and deformation measured at the surface. It is hypothesized that when an external force is applied on soft tissue, the shape of surface deformation of tissue has a quantitative relationship with the magnitude and direction of the force. Through such functional relations, the applied forces can be predicted once the deformation shape is detected.

A1.2 Defined Problems

This study proposes that there is a quantitative relationship between applied force and surface deformation shapes of soft tissue [Figure A1.2B]. The surface deformation could be simply represented by a series of principle parameters. The study will include two steps. First, we need to find such principle parameters that are proven by FEA to have a functional relationship with the applied force. The second step is to detect such parameters through in vitro experiments as well as proving that there is also a functional relation between surface deformation and force in reality.

A1.3 Methods

To solve the defined problems, the solution procedure includes two parts: simulation and in vitro experiments. For simulation, with known tissue mechanical properties, FEA experiments are performed to calculate surface deformation and force responses of soft tissue resulting from various indentation loadings. The expected quantitative relationship between the shape of surface deformation of tissue and the magnitude/direction of the force can be represented by $F^S = f^S(P_i)$, in which F^S is the applied force and P_i is the series of principle surface deformation parameters. Also in the simulation part, we will study two degree-of-freedom (DOF) force: grasping/squeezing first, and then pulling.

Through in vitro experiments, the principle deformation parameters are expected to be measured by our specially designed instrument or 3D imaging devices such as the PrimeSense(TM) depth camera; meanwhile, the force sensor can record the applied experimental force precisely. The calculated force derived from deformation parameters through the deformation-force function will be compared with the experimental applied force to test the validity. Figure 9 shows the solution procedure of both simulation and in vitro experiments.

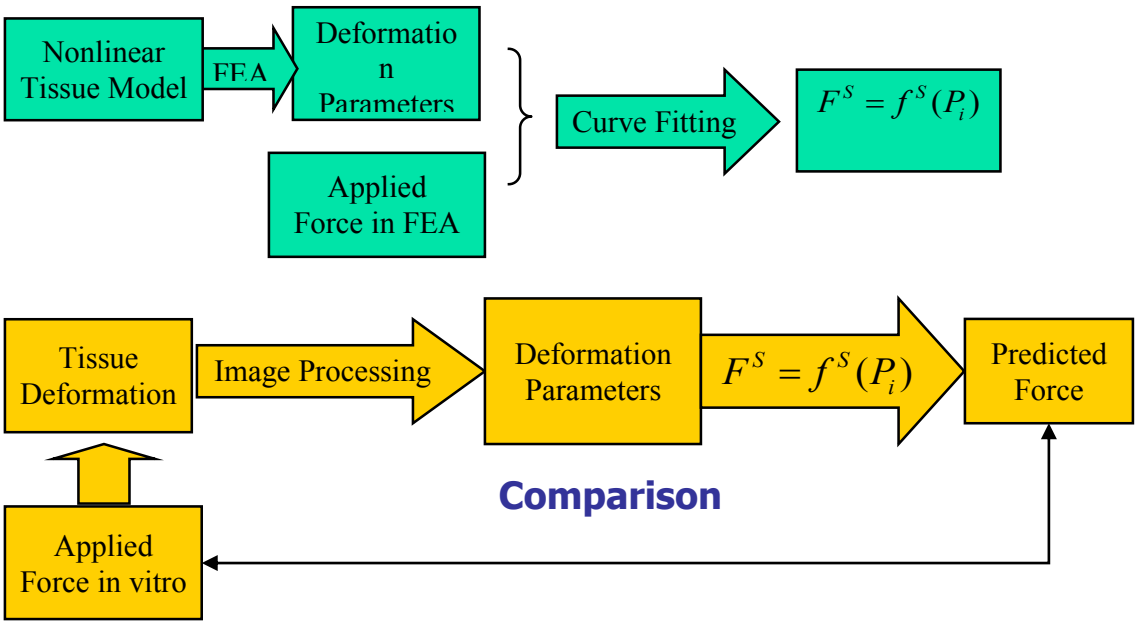

Figure A1.0.1 Solution procedure of predicting force through surface deformation of soft tissue. The green blocks represent the simulation part and the yellow blocks the in vitro experiments.

A1.3.1 FEA simulation

Similar to the study in Chapter 2, due to the symmetry of our problem, only half of the tissue (4mm height×16mm width) is considered and the bottom surface can only have freedom of motion along the x direction in the analysis. To simulate that the liver is attached to the anterior body wall through a falciform ligament, the region close to the falciform ligament is the objective of simulation, in which the left surface of the tissue model is completely constrained while there is no constraints on the right side (Figure 10).

The tissue is modeled with 8-noded axisymmetric, quadrilateral, solid elements. The material parameters for the 1st-order Ogden model are set to be α_1=19.48 and μ_1=0.001687. The meshing size for tissue is set to be uniform. The grasper domain is meshed using the same element type but its size is gradually refined for the portions which will potentially be involved in the grasper-tissue interaction (Figure10). Surgical graspers are considered to be composed of an isotropic linear elastic material (stainless steel) with the Young's modulus E=190GPa and the Poisson's ratio ν=0.27 [8].

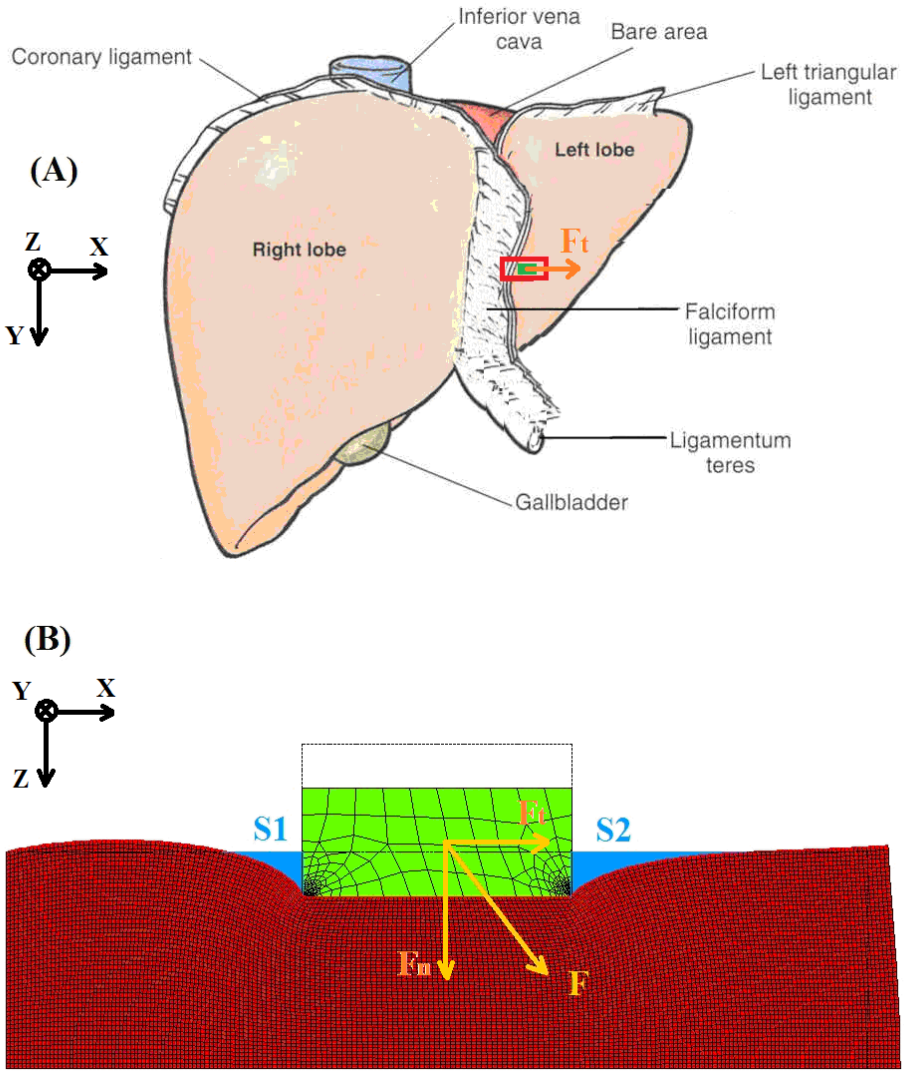

Figure A1.0.2 A) The exterior surface of the liver [9]. Area in red rectangle is the target location for simulation; B) Meshing size of grasper and tissue in 2D FEA. Green block represents grasper and red part means the soft tissue. Dotted lines mark the initial positions of grasper and tissue. S1 and S2 stand for the areas enclosed by deformed tissue contour, grasper boundary and underformed tissue contour. It is hypothesized that in vitro experiments, contour parameters such as S1 and S2 are able to be measured via the deformation sensors described in section A1.3.2.

A1.3.2 Phantom Tests

In order to compare the tissue surface deformation with the applied force, both of them need to be detected and recorded simultaneously. Several attempts have been made as stated in the following tests.

LED Based Deformation Sensor

As Figure A1.3A shows, a LED module can generate diffused light with luminous intensity only on its sides. The top side is attached to grasper jaw while the bottom is attached with opaque foil. No light comes out of the top and bottom sides. When the LED module is pressed against the top surface of soft tissue, there exists a deformed area with curved contour, adjacent to the emitting source. The image taken by the camera placed above the LED module can detect the deformation area in a region adjacent to the contact area. Meanwhile, the prototype device (Figure A1.3B) can measure the force by use of a 6-axis torque/force transducer (ATI Nano 17). After coordinate transformation, the applied force on the soft tissue can be derived.

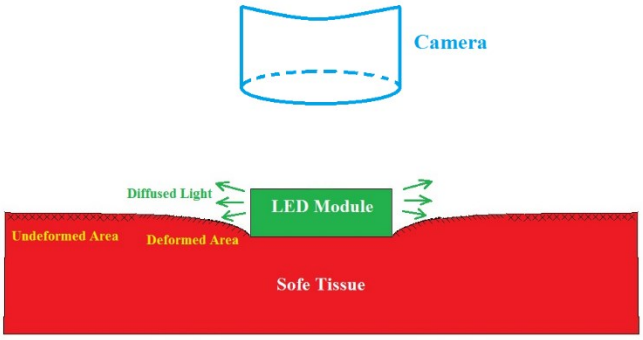

Figure A1.0.3A Illustration of the concept using LED for detecting soft deformation.

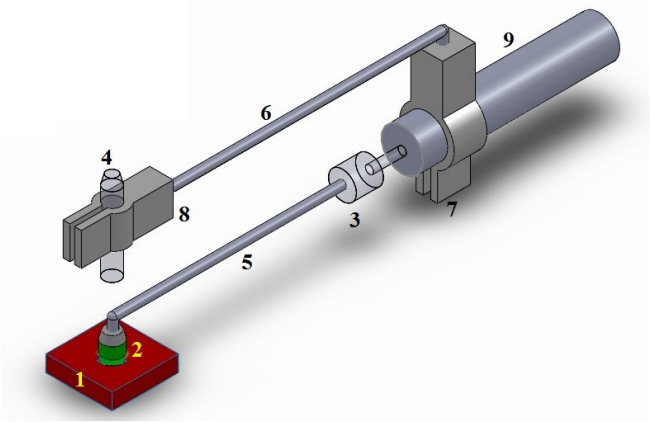

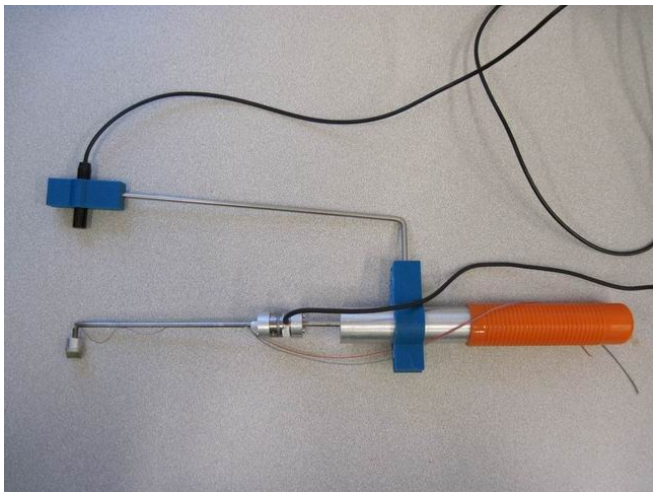

Figure A1.3B. Prototype design of LED based deformation sensor. 1. Soft Tissue; 2. Green High Brightness LED Module; 3. Force/Torque Sensor; 4. Camera; 5, 6. Rigid steel bar; 7, 8. Clips; 9. Handle. The top figure is the CAM file and the bottom figure shows the prototype we built so far.

To build phantom (ABS plastic model) with known deformation shapes for testing, ANSYS was firstly employed to simulate the deformed shape of soft tissue under applied strains of 10%, 20% and 30% respectively. The deformed models (Figure A1.4A) were uploaded to a 3D printer and then printed out to produce three ABS plastic tissue phantoms, each of which has one imprint of the grasper LED module with different surface contours. Figure A1.4B, C shows the radius of light spot increasing with the rising applied strain.

A) 

B) 

C) 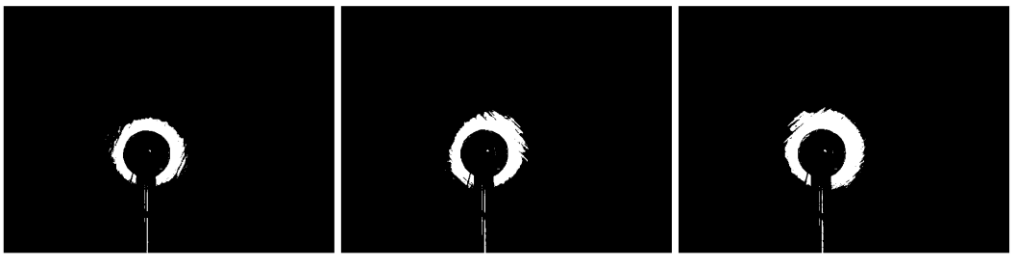

D) 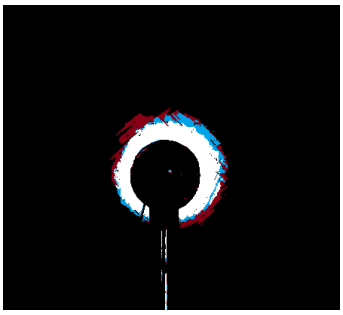

Figure A1.4. A) Rapid prototype printed phantom; B) Imaged captured by the prototype device. C) After image histogram analysis, binary images were obtained by setting all pixels in the grey degree (green component) range of 120~255 to be 1 (white) and the rest to be 0 (black); D) Overlapped image derived from binary images; white, blue and red light rings correspond to the strains of 10%, 20% and 30%, respectively.

RGB-D Camera

Another potential method for detecting surface deformation is using an RGB-D camera, which combine RGB color information with per-pixel depth information. The PrimeSense Carmine v1.09 (TM) is a low cost RGB-D camera (retail price $200) that has been developed for 3D sensing. The PrimeSense sensor projects an infrared speckle pattern, which is then captured by an infrared camera in the sensor, and compared to reference patterns stored, which were captured previously at known depths. The sensor then estimates the per-pixel depth based on which reference patterns the projected pattern matches best [10]. The maximal frames-per-second (FPS) rate is 30, at which the resolution of the color image is 640x480 pixels. The operation range of the Carmine v1.09 is 0.35~1.4m. At the 0.5m distance, the depth resolution is 1 mm and the spatial resolution is 0.9 mm.

To investigate whether the PrimeSense can distinguish the slight deformation, the previously mentioned three phantom tissues with various strains, 10%, 20%, 30% (accordingly depth of imprints:1mm, 2mm, 3mm) were placed in front of the PrimeSense camera at a distance of 0.35m [Figure A1.5A]. The OpenNI, an open source platform, was firstly employed to set the parameters of the camera as well as fetching the depth data, which contains the X, Y, Z coordinate values for each pixel. Then the depth data was processed through MeshLab, an open source 3D mesh processing software system. Several involved steps included computing the normal from a point set, Poisson Disk sampling, and Poisson surface reconstruction. Figure A1.5C shows there were obvious visual differences in surface deformation among the three phantoms. However, the characterization of such deformations has not yet been quantified.

A) 

B) 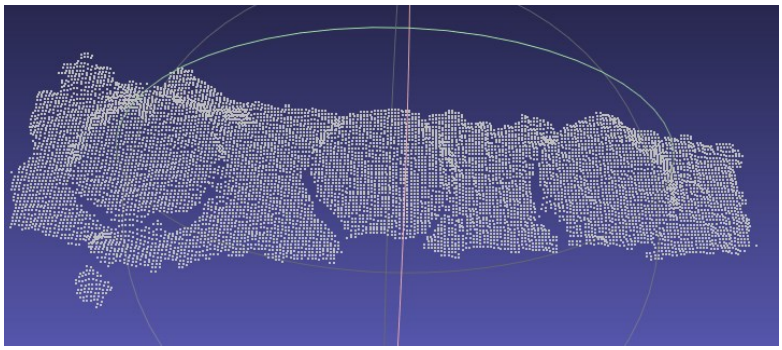

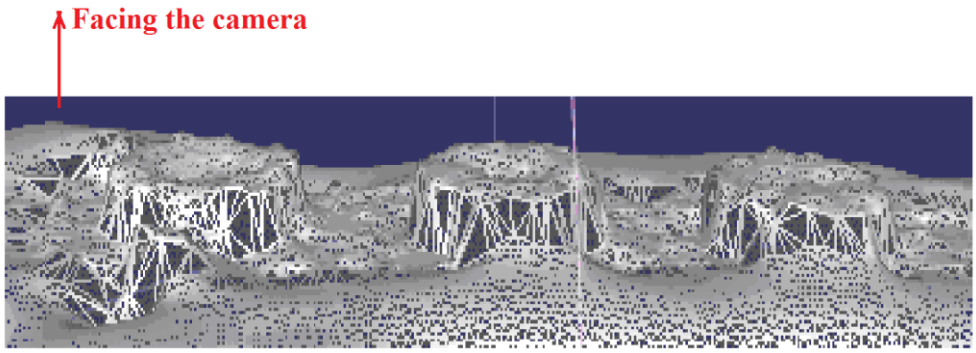

C)

Figure A1.5. A) Phantom tests through the PrimeSense camera; B) Rough fetched data by the depth camera, shown in the camera's view in MeshLab; C) Processed 3D depth data. From left to right, the applied strain rate decreases from 30% to 10%.

A1.4 Preliminary Results

A1.4.1 Simulation results

Two cases with different loading conditions were investigated by FEA: 1) the applied displacement of the grasper increased from 0 mm to 1mm in the negative y (grasping) direction (Uy=0~-1mm) at first and then from 0 mm to 1mm along the x (pulling) direction (Ux=0~1mm); 2) Uy=0~-0.5mm at first and then Ux=0~1mm. The displacement incremental was 0.1 mm. The contour areas S1, S2 along with the forces (tangential and normal directions) were recorded for each substep. For both loading conditions, the tangential force and the contour area difference S2-S1 have a significantly positive correlation with (Figure A1.6A). The least-square 3rd-order polynomial fitting function is

$$F_t = 0.4*(S2-S1)^3 + 0.56*(S2-S1)^2 + 0.4*(S2-S1) + 0.026 \qquad \text{(Eq A1.1)}$$

with the coefficient of determination R^2 =0.9947.

Similarly, the normal force and the contour area S2 have a significantly positive correlation (triangle markers in Figure 12B), which can be represented by the function:

$$F_n = 2.16*S2^3 + 1.46*S2^2 + 0.15*S2 + 0.174 \qquad \text{(Eq A1.2)}$$

with R^2 =0.9887.

The sum of contour areas S1+S2 are also plotted with normal forces (star markers in Figure A1.6B); however, no fitting function can be observed between them. Some other unsuccessful trials include the normal distance from the grasper-tissue contact boundary to the edge of the surface deformation contour D_i, and the projected distance of D_i on grasper-tissue interface plane.

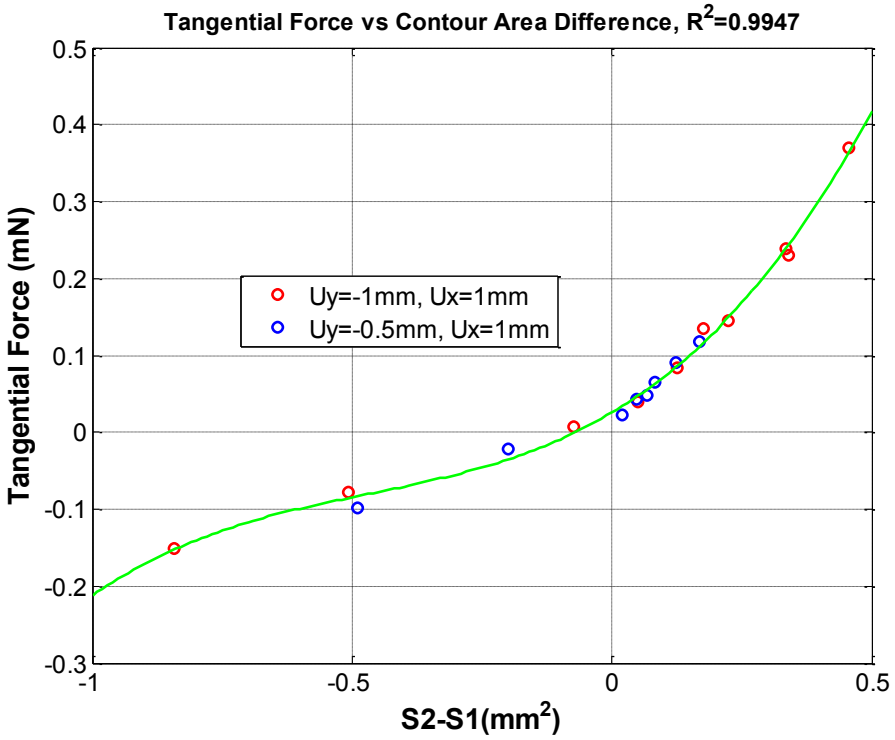

Figure A1.6A. Tangential force (mN) with the difference between contour areas (S2-S1). Green line represents the least-square 3rd-order polynomial fitting curve.

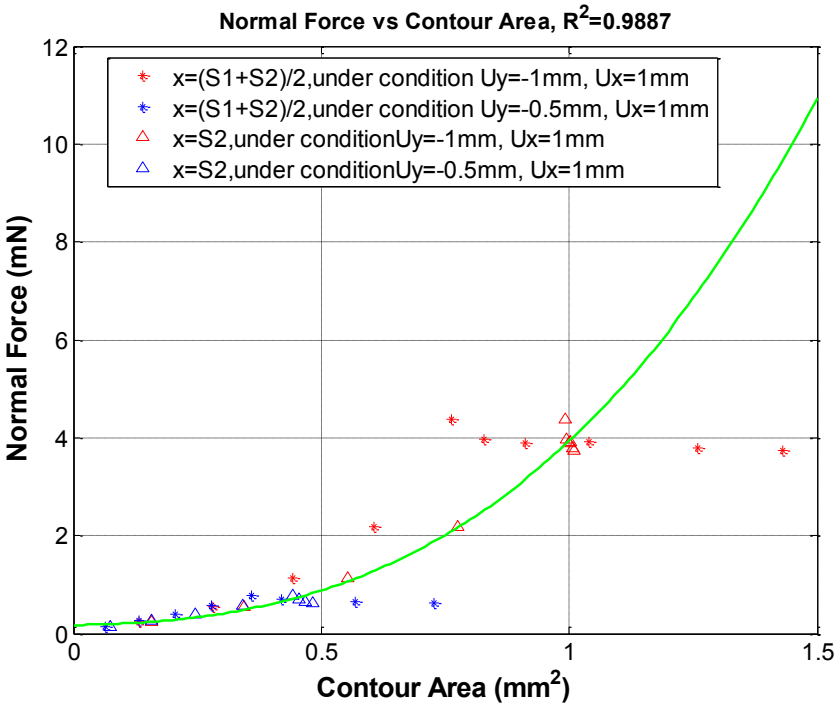

Figure A1.6B. Normal force (mN) with the contour areas S1, S2. Green line represents the least-square polynomial fitting curve for the case x=S2.

A1.4.2 Phantom tests results

With the LED deformation sensing device (Figure A1.3B), several trials have been performed to investigate the qualitative relationship between the surface deformation and the applied force on a sample of elastic material. A sample of commercially available artificial tissue (Simulab Corporation, Seattle, WA) was used to simulate soft tissue. The LED module tip of the device compressed the artificial tissue only on the Z direction gradually by free hand. Both RGB images and sensed force data were recorded for each loading step. Figure A1.7 shows that from left to right, the size of the intensive green light ring increased with rising applied Z-direction strain from step 1 to 5. However, from step 6 to 10, the change of the light ring was not obvious. Figure A1.8 shows that the force in the Y direction was close to zero for each loading step; however, no clear monotonic function was observed between the applied force in the Z direction and the loading steps. Besides, the force on the X direction was generally far away from zero for each step.

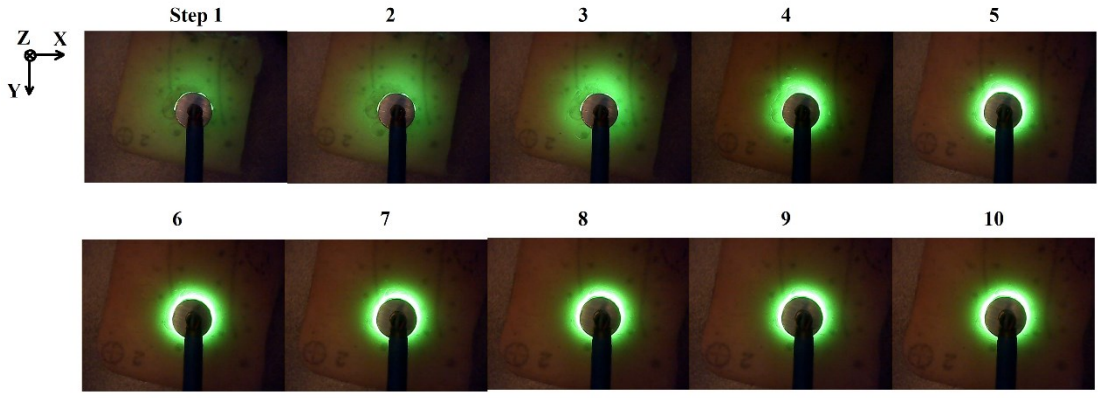

Figure A1.7. Rough fetched RGB images by the LED deformation sensing device. The color of LED source is green.

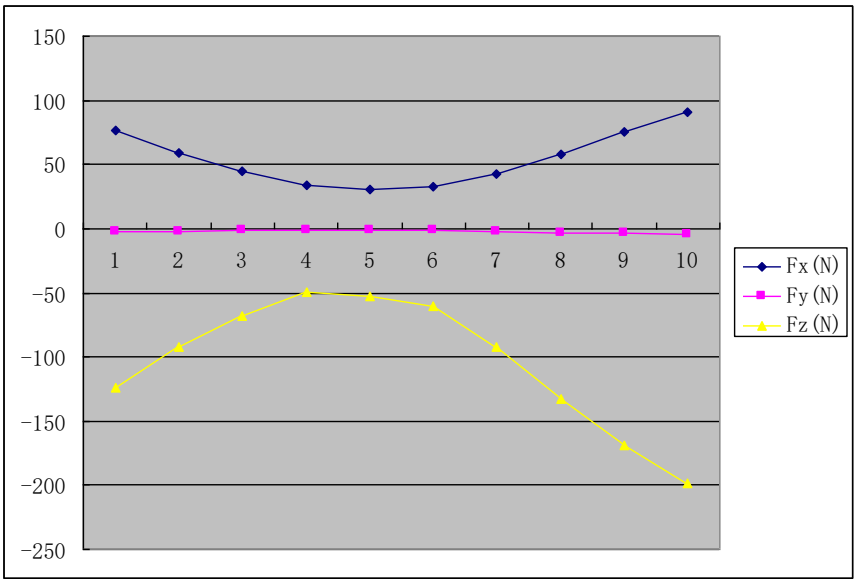

Figure A1.8. The values of three directional forces with loading steps.

A1.5 Reference for Appendix 1

[1] P Meseure and C Chaillou. Deformable body simulation with adaptative subdivision and cutting. Proceedings of WSCG, 361-370, 1997.

[2] K Tagawa, et al. Adaptive and Embedded Deformation Model: An Approach to Haptic Interaction with Complex Inhomogeneous Elastic Objects. IEEE World Haptics Conference, 169-174, 2013.

[3] U Kocak, et al. Dynamic Deformation Using Adaptable, Linked Asynchronous FEM Regions. Proceedings of the 25th Spring Conference on Computer Graphics, 197-204, 2009.

[4] K Morooka, et al. Real-Time Nonlinear FEM with Neural Network for Simulating Soft Organ Model Deformation. Medical Image Computing and Computer-Assisted Intervention – MICCAI 2008 Lecture Notes in Computer Science, 5242: 742-749, 2008.

[5] X Chen, et al. Study on liver surgery navigation based on nonlinear finite element method. Journal of Japan Society of Computer Aided Surgery 5: 15-22, 2003.

[6] BM Ahn, et al. Robotic palpation and mechanical property characterization for abnormal tissue localization. Medical & Biological Engineering & Computation 50(9):961-971, 2012.

[7] H Liu, et al. Inverse finite-element modeling for tissue parameter identification using a rolling indentation probe. Medical & Biological Engineering & Computation, published online, September 15th, 2013.

[8] S De, J Rosen, A Dagan, B Hannaford, P Swanson, M Sinanan. Assessment of tissue damage due to mechanical stresses. International Journal of Robotic Research, 26:1159–1171, 2007.

[9]http://academic.amc.edu/martino/grossanatomy/site/Medical/Lab%20Manual/Gastrointestinal/answers/stomach3.htm

[10] http://www.google.com/patents/US20070216894?dq=primesense

Appendix2. Supplemental material for Chapter 4

It is found in Chapter 2 that the FEA simulation results from the 2D plane strain and 2D plane stress models formed the upper and lower bound of the results obtained from full 3D model cut plane. Chapter 4 is a modified version of the manuscript that was published earlier than Chapter 2 and Chapter 4 only presents the simulation results from 2D plane strain. As a supplemental material for Chapter 4, Appendix 2 includes the simulation results from 2D plane stress using the same continuum mechanical model and grasper pattern as stated in Chapter 4. Our results show that though the absolute calculated von Mises stress values from 2D plane stress are less than those from 2D plane strain, the conclusion of Chapter 4 "There is less tissue damage with increasing radius of curvature. A smooth wave pattern reduced tissue damage at the cost of inducing higher percentage of slipping area." still stands. Figure A2.1-2.2 illustrate the simulation results from 2D plane stress.

A) Peak von Mises stress(kPa) for rectangular graspers with different radius of curvature. The displacement loads are Uy and Ux (mm).

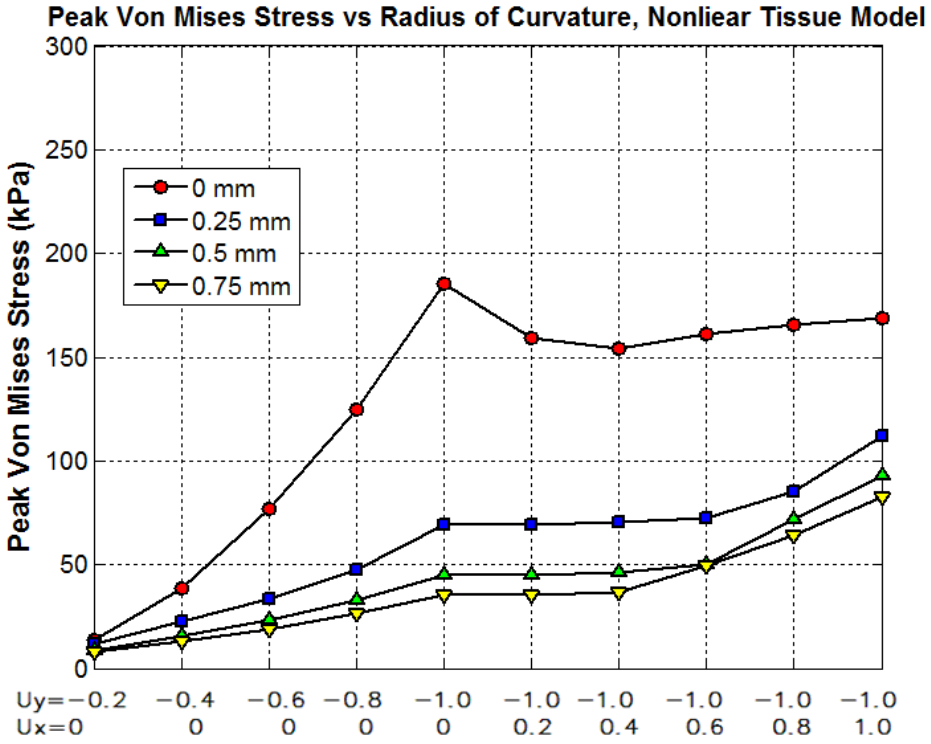

B) Integrated von Mises stress (N) with different radius of curvature.

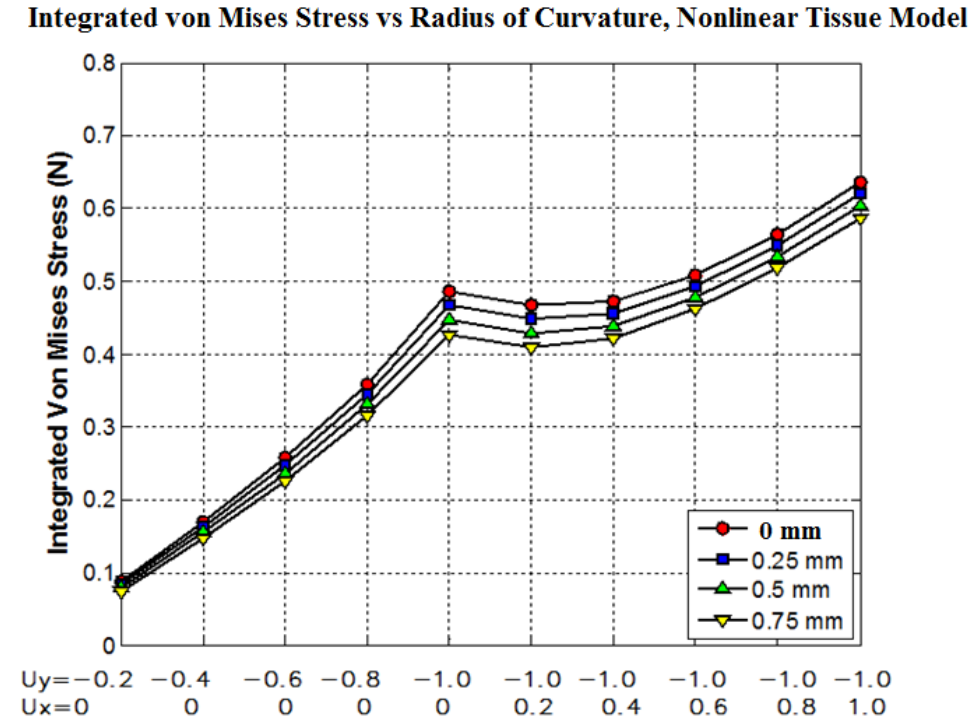

C) Integrated dimensionless tissue damage with radius of curvature.

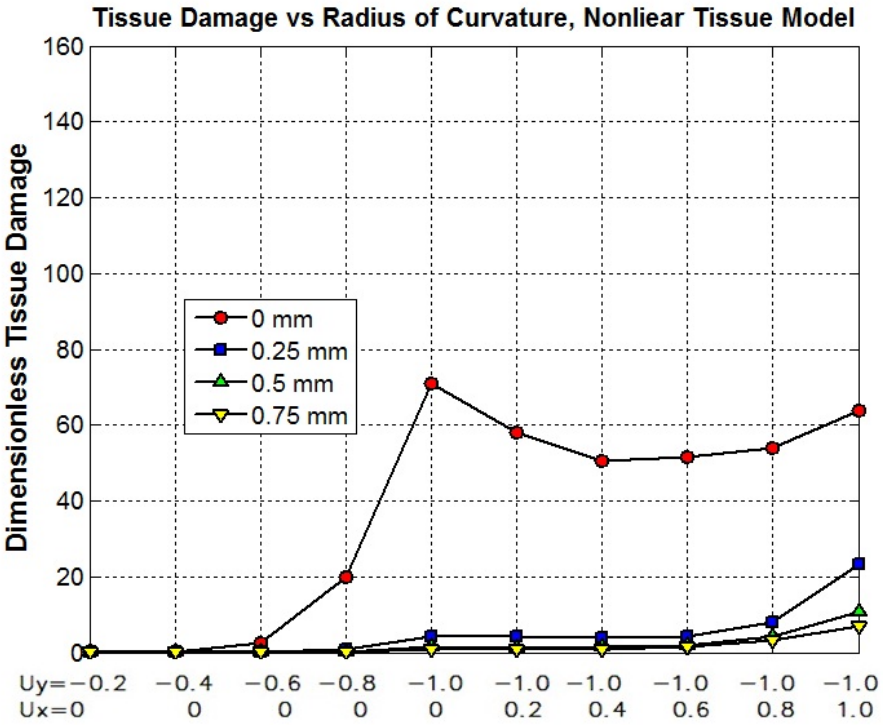

Figure A2.1.

A) Peak von Mises stress (kPa) with different tooth patterns. The displacement loads are Uy and Ux (mm).

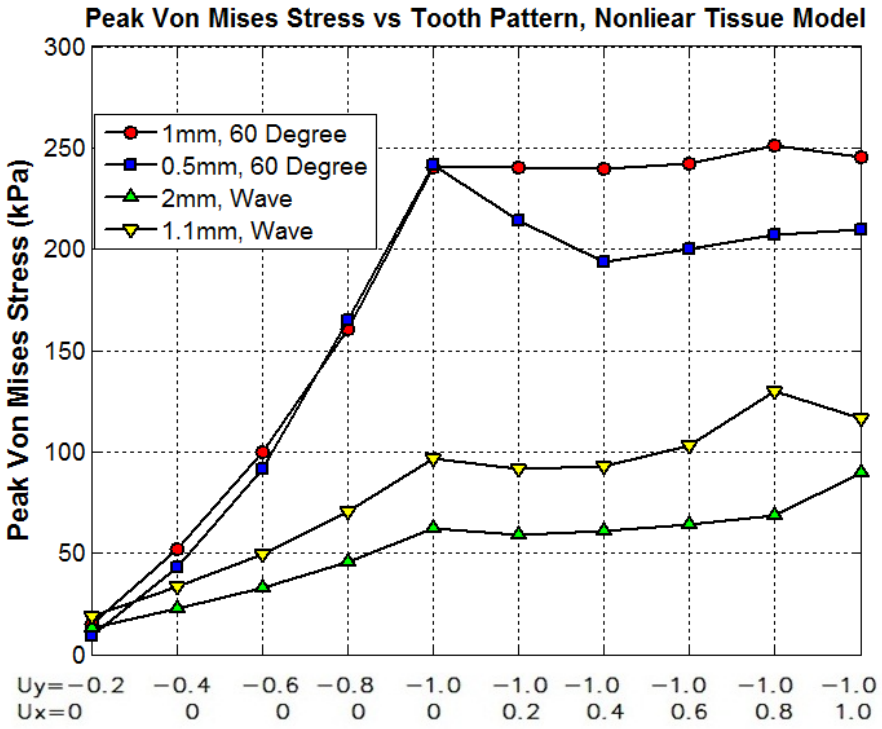

B) Integrated von Mises stress (N) with different tooth patterns.

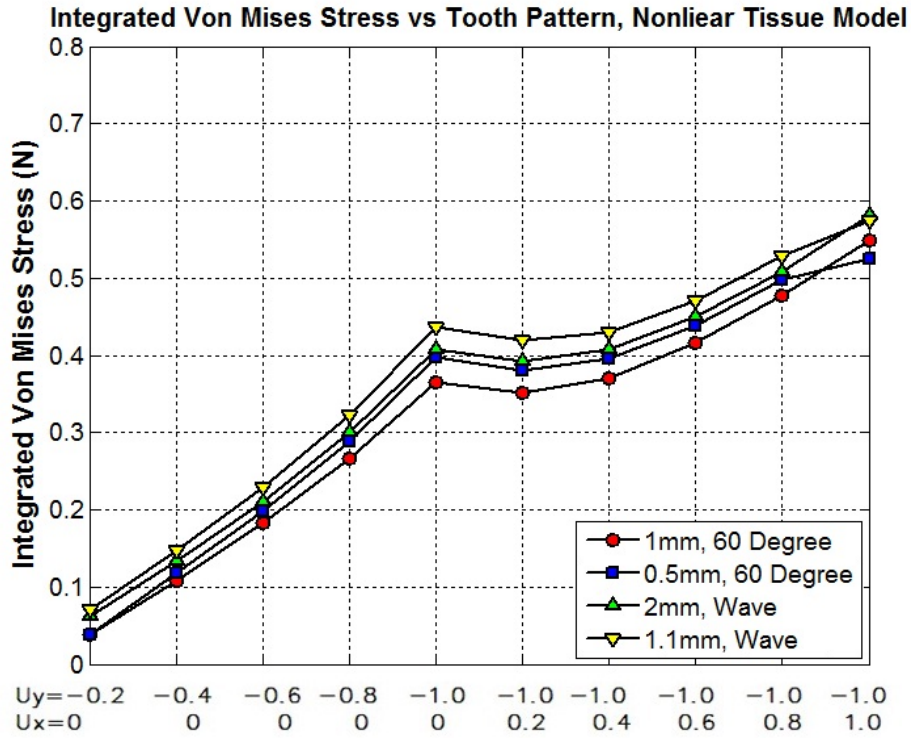

C) Integrated dimensionless tissue damage with different tooth patterns.

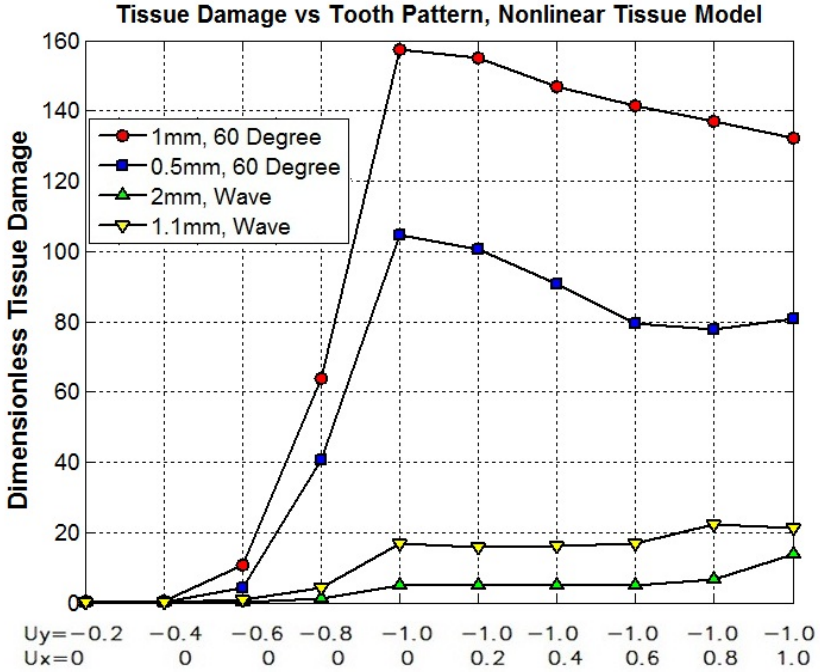

Figure A2.2.

BIBLIOGRAPHY

[1] Market engineering research for the U.S. market for general surgery laparoscopy access and closure instruments. Medical and Healthcare Marketplace Guide, 1999. Publisher: Frost & Sullivan London 071 730 3438. Dialog File Number 767 Accession Number 523034. [Cited 2001 Oct 18]. Available from: URL: http://www.dialogselect.com/business/cgi/present

[2] NJ Soper, LM Brunt, K Kerbl. Laparoscopic general surgery. New England Journal of Medicine. 10;330(6):409–419;1994.

[3] http://www.cnn.com/2013/08/02/tech/da-vinci-robot-surgery/index.html

[4] http://www.intuitivesurgical.com/company/

[5] S De. The Grasper-Tissue Interface in Minimally Invasive Surgery: Stress and Acute Indicators of Injury. Ph.D. Thesis, University of Washington, 2008.

[6] AM Okamura. Haptic feedback in robot-assisted minimally invasive surgery. Current Opinion in Urology. 19:102-107; 2009.

[7] BT Bethea, et al. Application of haptic feedback to robotic surgery. Journal of Laparoendoscopic and Advanced Surgical Techniques Part A. 14 (3):191-195, 2004.

[8] A.M. Okamura. Methods for haptic feedback in teleoperated robot-assisted surgery. Industrial Robot: An International Journal, 31(6):499-508, 2004.

[9] J Dargahi, et al. Modeling and testing of an endoscopic piezoelectric-based tactile sensor. Mechatronics. 17: 462-467, 2007.

[10] B Kubler, et al. Development of actuated and sensor integrated forceps for minimally invasive robotic surgery. The International Journal of Medical Robotics and Computer Assisted Surgery, 1(3):96-107, 2005.

[11] T Hu, G Tholey, JP Desai, AE Castellanos. Evaluation of a Laparoscopic Grasper with Force Feedback. Surgical Endoscopy, 18(5): 863-867, 2004.

[12] M MacFarlane, J Rosen, B Hannaford, C Pellegrini, M Sinanan. Force feedback grasper helps restore the sense of touch in minimally invasive surgery. Journal of Gastrointestinal Surgery, 3(3):278–285, 1999.

[13] J Rosen, B Hannaford, M MacFarlane, M Sinanan. Force Controlled and Teleoperated Endoscopic Grasper for Minimally Invasive Surgery - Experimental Performance Evaluation. IEEE Transactions on Biomedical Engineering, 46:1212-1221, Oct, 1999.

[14] G. Tholey, JP Desai, AE Castellanos. Force feedback plays asignificant role in minimally invasive surgery: results and analysis. Annals of Surgery. 241(1):102–109, 2005.

[15] K Vakili, MS Flander, TR Sepp, MCorral, JD Diaz, A Slocum, GSL Teo. Design and Testing of a Pressure Sensing Laparoscopic Grasper. Proceedings of the 2011 Design of Medical Devices Conference DMD2011. April 12-14, 2011, Minneapolis, MN, USA

[16] AJ Shakeshaft, JA Cartmill, WR Walsh, CJ Martin. A curved edge moderates high pressure generated by a laparoscopic grasper. Surgical Endoscopy. 15:1232–1234, 2001.

[17] DD Marucci, J A Cartmill, WR Walsh, C. J. Martin. Patterns of failure at the instrument tissue interface. Journal of Surgical Research. 93(1):16-20, 2000.

[18] EA Heijnsdijk, VH de, J Dankelman, DJ Gouma. Slip and damage properties of jaws of laparoscopic graspers. Surgical Endoscopy, 18: 974-979, 2004.

[19] JC Kalff, WH Schraut, RL Simmons, AJ Bauer. Surgical manipulation of the gut elicits an intestinal muscularis inflammatory response resulting in postsurgical ileus. Annals of Surgery, 228(5):652-663, 1998.

[20] R Anup, KA Balasubramanian. Surgical stress and the gastrointestinal tract. Journal of Surgical Research. 92(2):291-300, 2000.

[21] J Stoll, P Dupont. Force Control for Grasping Soft Tissue. Proceedings of the 2006 IEEE International Conference on Robotics and Automation, May 2006, Orlando, FL, USA.

[22] VA Ho, S Hirai. Understanding Slip Perception of Soft Fingertips by Modeling and Simulating Stick-Slip Phenomenon. Robotics: Science and Systems, 2011.

[23] N Xydas, M Bhagavat, I Kao. Study of soft-finger contact mechanics using finite elements analysis and experiments. Proceedings of IEEE International Conference on Robotics and Automation, 2179–2184, 2000.

[24] J Tian, YB Jia. Modeling deformable shell-like objects grasped by a robot hand. Proceedings of the IEEE International Conference on Robotics and Automation, 1297-1302, 2009.

[25] G. Tholey, JP Desai, AE Castellanos. Force feedback plays a significant role in minimally invasive surgery: results and analysis. Annals of Surgery. 241(1):102–109, 2005.

[26] N Famaey, E Verbeken, S Vinckier, B Willaert, P Herijgers, J Vander Sloten. In vivo soft tissue damage assessment for applications in surgery. Medical Engineering and Physics, 32:437–443, 2010.

[27] N Famaey, J Vander Sloten, E Kuhl. A three-constituent damage model for arterial clamping in computer-assisted surgery. Biomechanics and Modeling in Mechanobiology, DOI: 10.1007/s10237-012-0386-7, 2012.

[28] S De, J Rosen, A Dagan, B Hannaford, P Swanson, M Sinanan. Assessment of tissue damage due to mechanical stresses. International Journal of Robotic Research, 26:1159–1171, 2007.

[29] YB Fu, CK Chui. Modeling and Simulation of Porcine Liver Tissue Indentation using Finite Element Method and Uniaxial Stress-Strain Data. Journal of Biomechanics, http://dx.doi.org/10.1016/j.jbiomech.2014.04.009.

[30] YC Fung. Biomechanics: mechanical properties of living tissue. Springer, Berlin Heidelberg, New York, 1981.

[31] FJ Carter, TG Frank, et al. Measurements and modeling of the compliance of human and porcine organs. Medical Image Analysis. 5(4), 231-236, 2001.

[32] C Chui, et al. Combined compression and elongation experiments and non-linear modeling of liver tissue for surgical simulation. Medical and Biological Engineering and Computing. 42(6):787–798, 2004.

[33] Z Gao, K Lister and JP Desai. Constitutive modeling of liver tissue: experiment and theory. Annals of Biomedical Engineering, 38(2):505, 2010.

[34] Berkay Yarpuzlu, et al. Correlation between the mechanical and histological properties of liver tissue. Journal of the Mechanical Behavior of Biomedical Materials, 29:403-416, 2013.

[35] J Rosen, JD Brown, S De, M Sinanan, B Hannaford. Biomechanical properties of abdominal organs in vivo and postmortem under compression loads. Journal of Biomedical Engineering, 130(2): 021020, 2008.

[36] Krueger et al. Comparison of 2D finite element modeling assumptions with results from 3D analysis for composite skin-stiffener debonding. Composite Structures, 57:161-168, 2002.

[37] RW Ogden. Large deformation isotropic elasticity: on the correlation of theory and experimental for compressible rubberlike solids. Proceedings of the Royal Society of London, Series A (Mathematical and Physical Sciences), 328(1575), 567-583, 1972.

[38] RGM Breuls, CVC Bouten, et al. Compression induced cell damage in engineered muscle tissue: an in vitro model to study pressure ulcer aetiology. Annals of Biomedical Engineering, 31, 1357-1364, 2003.

[39] KK Ceelen, A Stekelenburg, et al. Compression-induced damage and internal tissue strains are related. Journal of Biomechanics, 41(16), 3399-404, 2008.

[40] L Cheng, B Hannaford. Evaluation of Liver Tissue Damage and Grasp Stability Using Finite Element Analysis. Computer Methods in Biomechanics and Biomedical Engineering, Nov 19, 1-10, 2014, available online.

[41] RA Romeed, SL Fok, NH Wilson. A comparison of 2D and 3D finite element analysis of a restored tooth. Journal of Oral Rehabilitation, 33: 209–215, 2006.

[42] P Meseure and C Chaillou. Deformable body simulation with adaptative subdivision and cutting. Proceedings of WSCG, 361-370, 1997.

[43] K Tagawa, et al. Adaptive and Embedded Deformation Model: An Approach to Haptic Interaction with Complex Inhomogeneous Elastic Objects. IEEE World Haptics Conference, 169-174, 2013.

[44] U Kocak, et al. Dynamic Deformation Using Adaptable, Linked Asynchronous FEM Regions. Proceedings of the 25th Spring Conference on Computer Graphics, 197-204, 2009.

[45] BM Ahn, et al. Robotic palpation and mechanical property characterization for abnormal tissue localization. Medical & Biological Engineering & Computation 50(9):961-971, 2012.

[46] H Liu, et al. Inverse finite-element modeling for tissue parameter identification using a rolling indentation probe. Medical & Biological Engineering & Computation, 52(1):17-28, 2014.

[47] K Morooka, et al. Real-Time Nonlinear FEM with Neural Network for Simulating Soft Organ Model Deformation. Medical Image Computing and Computer-Assisted Intervention – MICCAI 2008 Lecture Notes in Computer Science, 5242: 742-749, 2008.

[48] X Chen, et al. Study on liver surgery navigation based on nonlinear finite element method. Journal of Japan Society of Computer Aided Surgery 5: 15-22, 2003.

[49] S Giannarou, MV Scarzanella and GZ Yang. Probabilistic Tracking of Affine-Invariant Anisotropic Regions. IEEE Transactions on Pattern Analysis and Machine Intelligence, 99, 2012.

[50] L Cheng, B Hannaford. Finite Element Analysis for Evaluating Liver Tissue Damage Due to Mechanical Compression. Journal of Biomechanics, Vol. 48, Issue 6, 948-955. 2015.

[51] P Mountney, D Stoyanov and GZ Yang. Three-Dimensional Tissue Deformation Recovery and Tracking: Introducing techniques based on laparoscopic or endoscopic images. IEEE Signal Processing Magazine, 27(4): 14-24, 2010.

[52] E Noohi, S Parastegari and M Žefran. Using Monocular Images to Estimate Interaction Forces During Minimally Invasive Surgery. 2013 IEEE/RSJ International Conference on Intelligent Robots and Systems (IROS), 4297-4302.

[53] PS Tsai and M Shah. Shape from shading using linear approximation. Image and Vision Computing, 1994.

[54] G Zeng, Y Matsushita, et al. Interactive Shape from Shading. IEEE Computer Society Conference on Computer Vision and Pattern Recognition, 1:343-350, 2005.

[55] RS Fearing. Simplified grasping and manipulation with dextrous robot hands. IEEE Journal of Robotics and Automation, 2(4):188–195, 1986.

[56] D Goeger, N Ecker, H Woen. Tactile sensor and algorithm to detect slip in robot grasping processes. Proceedings of the IEEE International Conference on Robotics and Biomimetics, 1480-1485, 2009.

[57] S Shirafuji, K Hosoda. Detection and prevention of slip using sensors with different properties embedded in elastic artificial skin on the basis of previous experience. Robotics and Autonomous Systems (2012): doi:10.1016/j.robot.2012.07.016.

[58] T Maeno, S Hiromitsu, T Kawai. Control of grasping force by detecting stick/slip distribution at the curved surface of an elastic finger. Proceedings of the IEEE International Conference on Robotics and Automation, 3895-3900, 2000.

[59] N Famaey, G Sommer, J Vander Sloten, et al. Arterial clamping: Finite Element Simulation and In Vivo Validation. Journal of the Mechanical Behavior of Biomedical Materials, 12, 107-118, 2012.

[60]http://academic.amc.edu/martino/grossanatomy/site/Medical/Lab%20Manual/Gastrointestinal/answers/stomach3.htm

[61] http://www.google.com/patents/US20070216894?dq=primesense

VITA

LEI CHENG

EDUCATION

PhD	**Mechanical Engineering** University of Washington (UW), Seattle, WA	Sep 2008-June 2015
MS	**Biomedical Engineering, College of Engineering** Peking University, Beijing, China	Sep 2005-Jun 2008
BS	**Biomedical Engineering, College of Engineering** Tianjin University, Tianjin, China	Sep 2000-Jun 2005

PROFESSIONAL EXPERIENCE

Research Assistant at Bio-Robotics Laboratory of UW (Seattle, WA)	Jan 2011- June 2015
Research Assistant at UW (Seattle, WA)	Sep 2008-Dec 2010
Server Engineer at Peking University (Beijing , China)	Sep 2005-Jun 2008
Component Engineer Intern, at Ericsson R&D Center (Beijing , China)	Oct 2005–Dec 2005

PUBLICATIONS

[1] **Lei Cheng**, Blake Hannaford. Finite Element Analysis for Evaluating Liver Tissue Damage Due to Mechanical Compression. Journal of Biomechanics. 2015. Accepted.

[2] **Lei Cheng**, Blake Hannaford. Evaluation of Liver Tissue Damage and Grasp Stability Using Finite Element Analysis. Computer Methods in Biomechanics and Biomedical Engineering. 2014, Nov 19: 1-10.

[3] Blake Hannaford, Jacob Rosen, Diana Friedman, Hawkeye King, Philip Roan, **Lei Cheng**, Daniel Glozman, Ji Ma, Sina Nia Kosari , Lee White. Raven-II: An Open Platform for Surgical Robotics Research. IEEE TRANSACTIONS ON BIOMEDICAL ENGINEERING, VOL. 60, NO. 4, APRIL 2013.

[4] Lee White, Randall A. Bly, Daniella D'Auria, Paul Bartell, **Lei Cheng**, Blake Hannaford. Cricothyrotomy Simulator with Computational Skill Assessment for Procedural Skill Training in the Developing World. Otolaryngology–Head and Neck Surgery, 149(2S), 2013.

[5] Hawkeye King, **Lei Cheng**, Philip Roan, Diana Friedman, Sina Nia Kosari, Ji Ma, Daniel Glozman Jacob Rosen, Blake Hannaford, Raven II™: Open Platform for Surgical Robotics Research, The Hamlyn Symposium on Medical Robotics, July 1-2 2012, London, UK.

[6] Hsiu-hung Simon Chen, Zhiquan Shu, **Lei Cheng**, and Dayong Gao. Development of a microfludic injection and perfusion device for single cell study. Proceedings of ASME 2010 First Global Congress on Nano-engineering for Medicine and Biology NEMB 2010 February 7-10,Houston, TX, USA.

[7] **Lei Cheng**, Tao Wang. Ideal sodium concentration in peritoneal dialysate: from the view of fluid and sodium balance. The 3rd ACM-ISPD, 2007.

[8] **Lei Cheng**, Tao Wang. Current practiced hemodialysis and peritoneal dialysate achieved identical level of nitrogen balance. The 8th Euro PD Conference, 2007.

[9] **Lei Cheng**, Tao Wang. Three-pore model of trans-membrane mass transfer in peritoneal dialysis and its computer simulations. Journal of Biomedical Engineering, 2008; 4: 318-324.

[10] Qian Lu, **Lei Cheng**, Jonas Axelesson, Bengt Lindholm, Tao Wang. No Difference in Nitrogen Balance between Standard Prescriptions of Hemodialysis and Peritoneal Dialysis. Blood Purification, 2008; 26:511-517.

[11] Xing-wei Zhe, Yi-sheng Shan, **Lei Cheng**, Tao Wang. A simple method for estimation of peritoneal fluid transport. Blood Purification, 2007; 25: 161-168.

[12] Xing-wei Zhe, Xin-kui Tian, Yi-sheng Shan, **Lei Cheng**, Tao Wang. Evaluating peritoneal fluid transport in continuous peritoneal dialysis patients: a practical approach. Nephron Clinical Practice. 2007; c123-127.

[13] Xing-wei Zhe, Xin-kui Tian, **Lei Cheng**, Tao Wang. Ultrafiltration capacity and peritoneal fluid kinetics in CAPD patients. Artificial Organs, 2007; 32:61-65.

[14] Xing-wei Zhe, Xin-kui Tian, **Lei Cheng**, Tao Wang. Effects of peritoneal resting on peritoneal fluid transport kinetics. Peritoneal Dialysis International. 2007; 27(5):575-579.

[15] Li-tao Cheng, Li-jun Tang, **Lei Cheng**, Hai-yan Huang, Tao Wang. The limitation of augmentation index in evaluating arterial stiffness. Hypertension Research. 2007; 30:713-722.